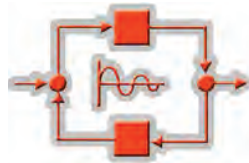




**The International Congress for  
global Science and Technology**



**ICGST International Journal on Automatic  
Control & System Engineering  
(ACSE)**

**Volume (16), Issue (II)  
December 2016**

**[www.icgst.com](http://www.icgst.com)  
[www.icgst-amc.com](http://www.icgst-amc.com)  
[www.icgst-ees.com](http://www.icgst-ees.com)**

**© ICGST LLC, 2016  
Delaware, USA**

ACSE Journal  
ISSN: Print 1687-4811  
ISSN Online 1687-482X  
ISSN CD-ROM 1687-4838  
© ICGST LLC, 2016, Delaware, USA

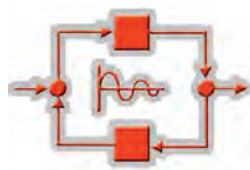
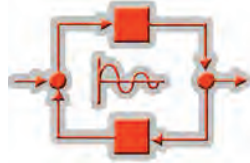


## Table of Contents

Papers	Pages
P1181632510, AUTHOR="Fahim Salauddin", TITLE="DPCM Soft Modelling in Open-Loop Representations"	1--8
P1111633511, AUTHOR="B. Dhouib and H. Hadj Abdallah", TITLE="Voltage Source Converter of Three Phase Photovoltaic Grid Connected System and Fault Analysis"	9--19
P1111638520, AUTHOR="G.Swapna and N.KrishnaKumari and D.Ravi Kumar", TITLE="Sensor less Control of PMSM with FOC using MRAS",	21--28
P1111634512, AUTHOR="Fethi Demim and Kahina Louadj and Aidene Mohamed and Abdelkrim Nemra", TITLE="Solution of an Optimal Control Problem with Vector Control using Relaxation Method",	29--41
P1111636517, AUTHOR="Raheel Muzzammel and Umair Tahir", TITLE="Comprehensive Comparison of PWM and SVM based Three Phase AC to AC Matrix Converters",	43--57
P1111641522, AUTHOR="Phi Hoang Nha and Dao Quang Thuy", TITLE="Improving the Characteristics of Switched Reluctance Motor",	59--66



**ICGST International Journal on Automatic Control & System Engineering -  
(ACSE)**

**A Publication of the International Congress for global Science and Technology -  
(ICGST)**

**ICGST Editor in Chief: Dr. rer. nat. Ashraf Aboshosha**

**[www.icgst.com](http://www.icgst.com), [www.icgst-amc.com](http://www.icgst-amc.com), [www.icgst-ees.com](http://www.icgst-ees.com)**

**[editor@icgst.com](mailto:editor@icgst.com)**



## DPCM Soft Modelling in Open-Loop Representations

Fahim Salauddin

Department of Electronic Engineering, La Trobe University

Melbourne, Australia

fahim.salauddin.bd@ieee.org

### Abstract

In Differential Pulse Coded Modulation (DPCM) the prediction of the next sample value is formed from the past values. This prediction can be considered as a set of instruction for the quantizer to conduct its next sample value in a particular interval. By using the redundancy in the signal to form a prediction, the region of uncertainty is reduced and the quantization can be performed with a reduced amount of decisions (or bits) for a given quantization level or reduced amount of quantization levels for a given number of decisions (or bits). This paper basically focuses on the software modeling of an open-loop DPCM structure by using MATLAB. During Simulation, comparisons were made in terms of different Signal to Noise ratios by using different number of bits per sample of the uniform quantization process and the prediction orders and their optimal values were determined. By determining these optimal values of number of bits as well as the prediction orders, the implementation of open-loop DPCM in production scenarios such as lossless compression or embedded compression could be made much more efficiently. Standalone graphical user interface (GUI) was developed for this task.<sup>1</sup>

**Keywords:** *dpcm, open-loop dpcm, quantization, differential pulse coded modulation, prediction error, pulse amplitude modulation, pulse coded modulation.*

### Nomenclature

DPCM	Differential Pulse Coded Modulation
$m[k]$	$K^{\text{th}}$ sample of uniform quantization
$d[k]$	Difference between two corresponding uniform quantization samples
$\Delta v$	Quantization interval
$L$	Quantization level
$\hat{m}[k]$	Estimated value of $K^{\text{th}}$ sample

<sup>1</sup> This study has been implemented on MATLAB software at BG320/322 lab. La Trobe University.

### 1. Introduction

DPCM compression depends on prediction technique, well-conducted prediction techniques leads to good compression rates, in other cases DPCM could mean expansion comparing to regular PCM encoding. There are two structures for DPCM: open-loop and close-loop. This paper is mainly focused on the software implementation of the open-loop DPCM.

DPCM is a computationally efficient means for waveform coding. Various common audio signals exhibit a long-term low-pass spectral characteristic which results in a significant correlation between successive samples of the input signal [1].

In order to address some of the applications of DPCM systems when it comes to audio compression, de-noising, video coding, prediction and communication, these papers could be considered [2, 3, 4, 5, 6].

Mansour et.al in their paper [7] created a simulation of the DPCM and ADM systems in Simulink. But there is still a lack of proper standalone GUI based software solutions to perform DPCM simulations. This research paper deals with this problem by creating a standalone GUI based open-loop DPCM simulation. Also this article deals with the determination of optimal values of bits per sample used in uniform quantization and the prediction orders by comparing SNRs. By doing so the applications mentioned in [2, 3, 4, 5, 6] could be performed more efficiently.

Section 2 deals with the theoretical backgrounds applied to the simulation process. This includes defining the relationship between the successive samples and how transmitting the difference between them helps the overall system to become more efficient, rather than transmitting the signal itself.

In section 3, the actual implementation of the simulation parameters were demonstrated. Various functions that were required to build up the robust GUI system for simulation were discussed in this section. Various combinations of experimental encoder and decoder values were also displayed in tabular format in this section.

Section 4 deals with the simulation results and various plots were constructed on the basis of trade-offs between the bits per sample of the uniform quantization process and the prediction order in this section. Tables displaying the



various signal to noise ratios for trade-offs between the bits per sample of the uniform quantization process and the prediction order were displayed in this section such that their optimal values could be found out.

Finally section 5 deals with the conclusion and possible scope of improvements for the project in future.

## 2. Theoretical Fundamentals

In analog messages it is possible to make a good guess about the sampled values from the knowledge of the past sample values. That is, the sample values are not independent and generally there is a great amount of redundancy in the Nyquist samples. Proper Exploration of this redundancy leads to encoding a signal with a lesser number of bits. If it is considered as a sample scheme where instead of transmitting the sample values, the system transmits the difference between the successive samples. Thus, if  $m[k]$  is the  $k$ th sample, instead of transmitting  $m[k]$ , the system transmits the difference  $d[k] = m[k] - m[k-1]$  [8].

At the receiver, knowing  $d[k]$  and the previous sample value  $m[k-1]$ , the system can reconstruct  $m[k]$ . So it can be seen that from the knowledge of difference  $d[k]$ , the system can reconstruct  $m[k]$  iteratively at the receiver. Now the difference between the successive samples is generally much smaller than the sample values. Thus, the peak amplitude  $m_p$  of the transmitted values is reduced considerably. Because the quantization interval  $\Delta v = m_p/L$ , for a given  $L$  (quantization level) this reduces the quantization interval  $\Delta v$ , thus reducing the quantization noise, which can increase the SNR [9].

The proposed system can improve upon this existing scheme by estimating or predicting the value of the  $k^{th}$  sample  $m[k]$  from a knowledge of the previous sample values. If this estimate is  $\hat{m}[k]$ , then it actually transmits the difference (prediction error)  $d[k] = m[k] - \hat{m}[k]$ . At the receiver also, we determine the estimate  $\hat{m}[k]$  from the previous sample values, and then generate  $m[k]$  by adding the received  $d[k]$  to the estimate  $\hat{m}[k]$ . So it is basically able to reconstruct the samples at the receiver iteratively. If everything has been done properly then the predicted or estimated value  $\hat{m}[k]$  will be close to  $m[k]$  and their difference (prediction error)  $d[k]$  will be even smaller than the difference between the successive samples.

## 3. Implementation

In DPCM coding a difference is based on the fact that most source signals shows significant correlation between successive samples so encoding uses redundancy in sample values which implies lower bit rate. Realization of basic concept (described above) is based on technique in which we have to predict current sample value based upon previous samples (or sample) and the system has to encode the difference between actual value of sample and predicted value (difference between samples can be interpreted as prediction error).

The open loop DPCM is comprised of mainly two main parts, the Encoder and the decoder. The encoding functionalities are implemented inside the encoder in the transmitting side while the decoding activities are performed by the decoder in the receiver side. Basically the encoder instead of encoding the input signal directly and sending it via the channel to the receiver, it encodes the difference between the main input signal sample and its linear prediction sample and sends it to the receiver for decoding. This is a much more efficient way of sending information from the transmitter and the receiver as it prevents a lot of redundant calculations. Due to this less number of bits will be needed to send the information via the channel so there will be less chance of bit error probability too.

The functionalities inside the encoder can be explained with the help of following equations that occurs inside the encoder.

$$x_p = \sum_{k=1}^M \alpha_k x[n-k] \quad (1)$$

$$e[n] = x[n] - x_p[n] \quad (2)$$

$$e_q[n] = Q(e[n]) \quad (3)$$

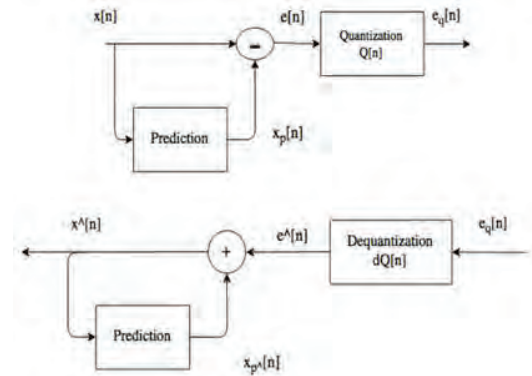


Figure 1: Encoder (top) and Decoder (bottom) block diagrams

Table1: Encoder Experimental values

n	1	2	3	4
$x[n]$	10	20	20	40
$x_p[n]$	0	9	18	18
$e[n]$	10	11	2	22
$e_q[n]$	2	2	0	5

For the experimental implementation of the encoder, the system basically takes an input signal  $x[n] = \{10, 20, 20, 40\}$ . The quantizer is designed as  $e_q = \text{floor}(\frac{e[n]}{4})$ . So it can be seen that after the input signal



traverses the entire block diagram of the encoder we are left with the values  $e_q = \{2, 2, 0, 5\}$ . The encoder basically transmits  $e_q$  than the actual signal  $x[n]$ .

The system can find the experimental values of the functioning of the decoder the same way as the encoder. The de-quantization block is designed as  $dQ = 4 * e_q[n]$ . Following is the table showing the experimental values of the decoder block.

Table 2: Decoder Experimental Values

n	1	2	3	4
$e_q[n]$	2	2	0	5
$\hat{e}[n]$	8	8	0	20
$\hat{x}_p[n]$	0	7.2	13.68	12.312
$\hat{x}[n]$	8	15.2	13.68	32.312

The proposed system can also find the error due to excessive quantization from the above experimental values which is given by equation (4). For this the above case it is found to be  $E[n] = \{2, 5, 6, 7\}$ .

$$E[n] = x[n] - \hat{x}[n] \quad (4)$$

Separate MATLAB functions entitled;

- *myQuantization*,
- *myDeQuantization*,
- *myPrediction*
- *myPredictionReconstruction*

were built to perform the functions of the block diagrams of the encoder and the decoder. A graphical user interface was also built that gave the user to choose between the three sound samples of handel, laughter and train in pop-up menu.

At first the system loaded the sound file *laughter* with sampling frequency of 8192 Hz in the main mat file. The users were asked in the GUI to enter the Quantization level (K) as well as the Prediction Order (N). As advised in the handouts we performed the encoding and the decoding process by using the Prediction Order of 3 (N = 3) and Quantization Level of 4 (K = 4). Following graphs were obtained:

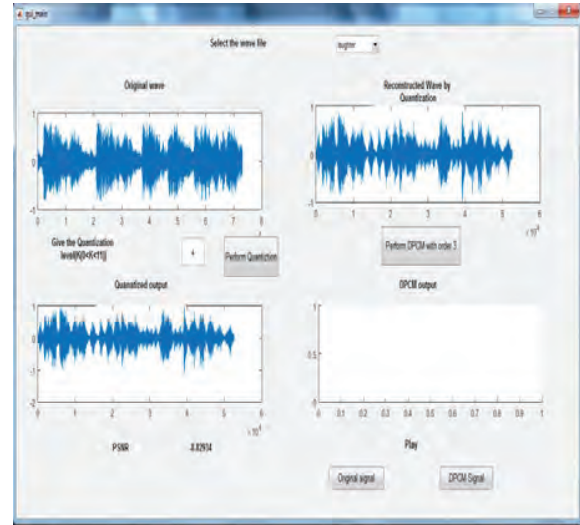


Figure 2: GUI for simulation of open-loop DPCM

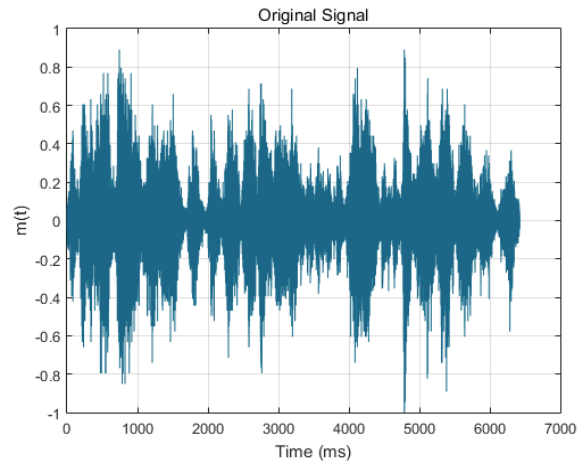


Figure 3: Original Signal (laughter)

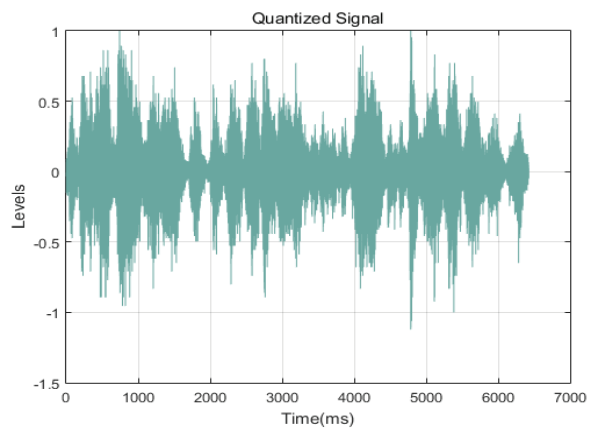


Figure 4: Quantized Signal (laughter)



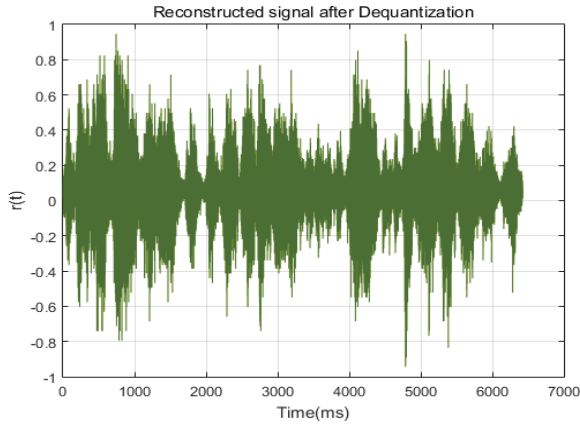


Figure 5: Signal after De-quantization (laughter)

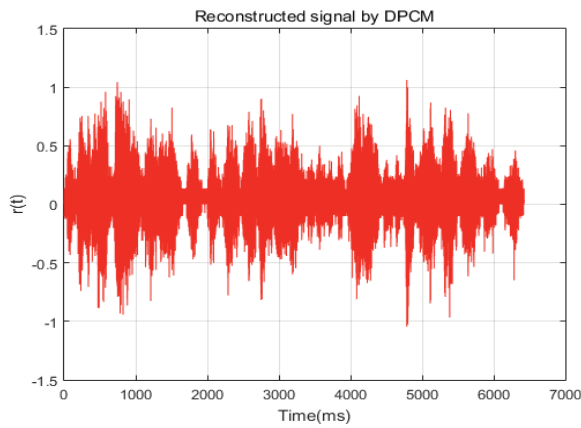


Figure 6: Signal after Linear prediction by order 3 (laughter)

In a similar way the other two signals *handel* and *train* could also be loaded in the main matlab file and it would ultimately give us the SNR that allowed us to estimate which prediction order or bits per sample are appropriate to re-generate the signal as close to the original signal as possible.

SNR was calculated by the given formula :

$$SNR = 10 \log_{10} \frac{\sum y[n]^2}{\sum (y[n] - r[n])^2} \quad (5)$$

#### 4. Experimental Results

In the experimental section I basically wanted to choose a suitable prediction order and the number of bits/sample to make a good compromise between the compression and the sound quality. We did that by comparing the SNR values of obtained from the following equation.

$$SNR = 10 \log_{10} \frac{\sum y[n]^2}{\sum (y[n] - r[n])^2} \quad (6)$$

Which is just a modified version of the following equation:

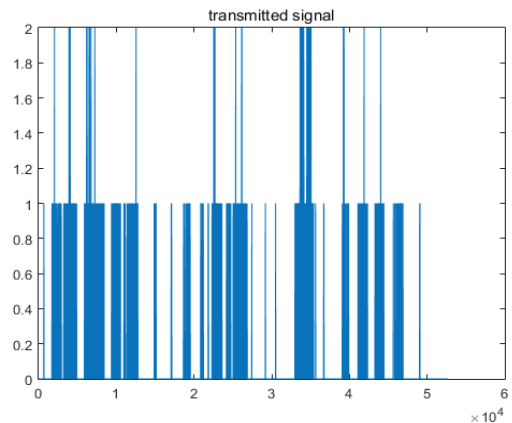
$$SNR = -10 \log_{10} \frac{\sum (r[n] - y[n])^2}{\sum y[n]^2} \quad (7)$$

I started the procedure by keeping  $K = 1$  and calculated the values of both  $SNR_r$  and  $SNR_e$  for  $1 \leq N \leq 5$ .

Table 3: SNR Comparison for  $k=1$  and  $1 \leq N \leq 5$ 

K	N	SNR_r
1	1	-22.1855
1	2	-16.1649
1	3	-10.2901
1	4	-6.1562
1	5	-4.6608
1	6	-4.3322

I observed from the table that as I increased the prediction order  $N$ , the  $SNR_r$  increased, which is desirable as the system was able to produce a sound quality much similar to the original signal. The system was thought to have a better Compression i.e. a better prediction then. As I saw that the system was getting a better sound quality as well as a better compression for both the increasing  $K$  and  $N$  I constructed the following table to get the optimal  $SNR_r$  and  $SNR_e$  values at the range of  $1 \leq K \leq 11$  and  $1 \leq N \leq 10$ .

Figure 7: Transmitted Signal for  $K = 4$   $N = 4$ Table 4: SNR Comparison for  $1 \leq K \leq 11$  and  $1 \leq N \leq 11$  (laughter)

K	N	SNR_r
1	1	-22.1855
2	2	-11.6936
3	3	-6.6188
4	4	-2.9897
5	5	-2.2874
6	6	-1.9291
7	7	-1.7244
8	8	-1.6341
9	9	-1.6012
10	10	-1.4655
11	11	-1.4442





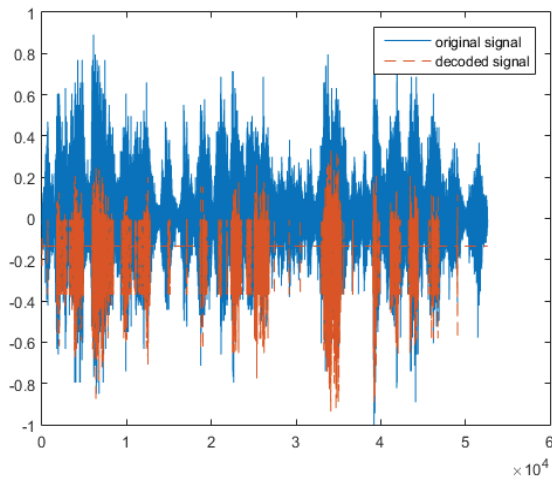


Figure 8: Original Vs. Decoded signal for  $K = 4$   $N = 4$

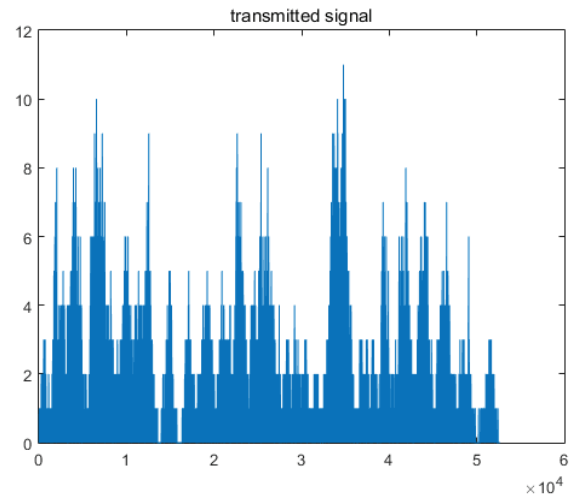


Figure 11: Transmitted Signal for  $K = 6$   $N = 6$

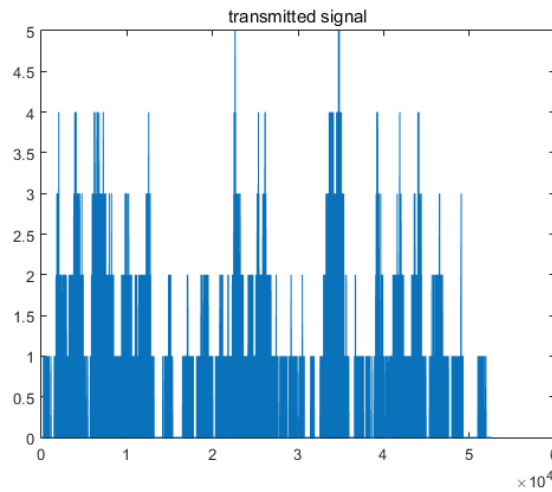


Figure 9: Transmitted Signal for  $K = 5$   $N = 5$

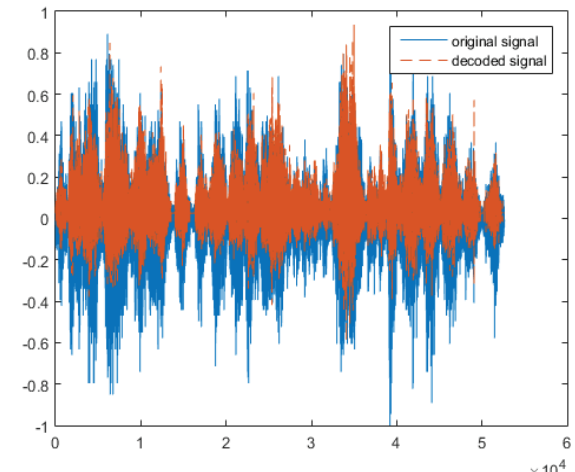


Figure 12: Original Vs. Decoded signal for  $K = 6$   $N = 6$

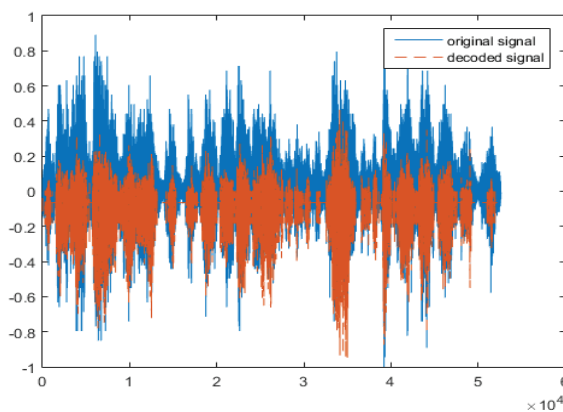


Figure 10: Original Vs. Decoded signal for  $K = 5$   $N = 5$

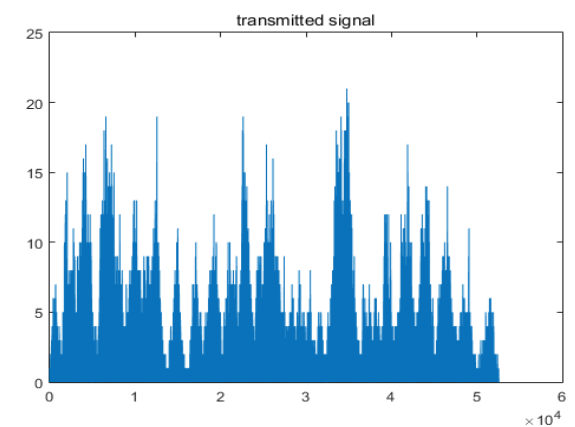
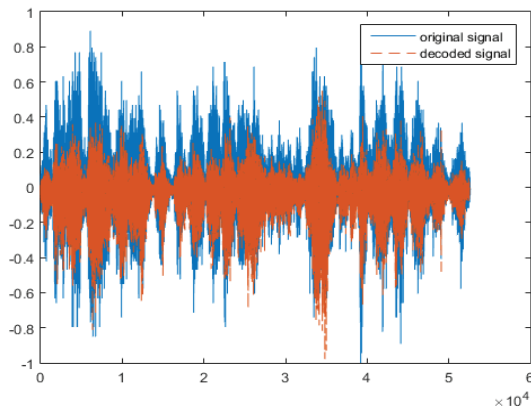
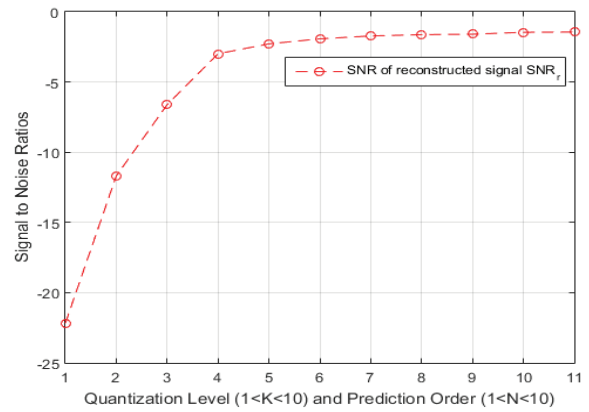
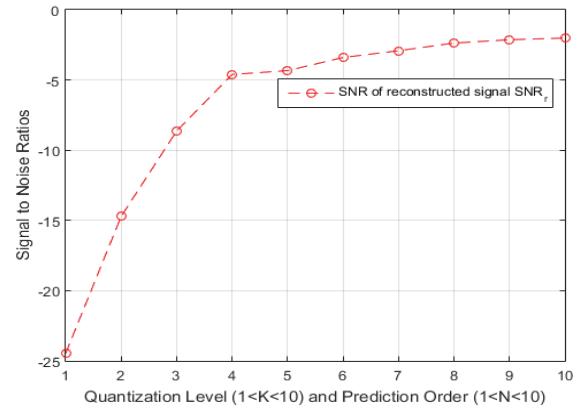


Figure 13: Transmitted Signal for  $K = 7$   $N = 7$

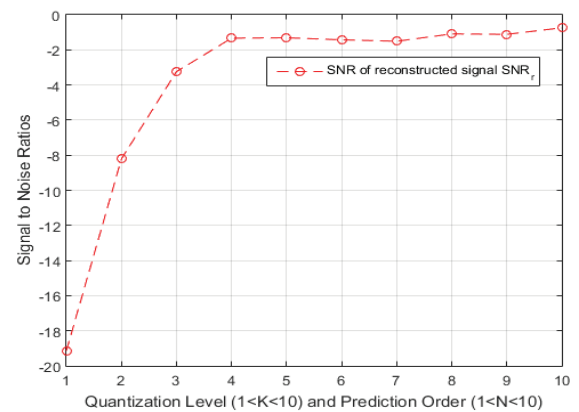


Figure 14: Original Vs. Decoded signal for  $K = 7$   $N = 7$ Figure 15: Signal to Noise ratios for both r and e against  $(1 < k < 11)$  and  $(1 < N < 11)$  for laughter signalTable 5: SNR Comparison for  $1 \leq K \leq 10$  and  $1 \leq N \leq 10$  (Handel)

K	N	SNR_r
1	1	-24.4608
2	2	-14.7124
3	3	-8.6330
4	4	-4.6088
5	5	-4.3354
6	6	-3.4003
7	7	-2.9174
8	8	-2.3727
9	9	-2.1369
10	10	-2.0144

Figure 16: Signal to Noise ratios for both r and e against  $(1 < k < 10)$  and  $(1 < N < 10)$  for handel signalTable 6: SNR Comparison for  $1 \leq K \leq 10$  and  $1 \leq N \leq 10$  (Train)

K	N	SNR_r
1	1	-19.1465
2	2	-8.2138
3	3	-3.2407
4	4	-1.3343
5	5	-1.3125
6	6	-1.4291
7	7	-1.5104
8	8	-1.0929
9	9	-1.1158
10	10	-0.7450

Figure 17: Signal to Noise ratios for both r and e against  $(1 < k < 10)$  and  $(1 < N < 10)$  for train signal

From the graph above it can be said that  $SNR_r$  is maximum for both  $K = 10$  and as well as  $N = 10$ . Whereas the prediction error is lowest for lowest for  $K = 10$  and  $N = 10$ . So it can be said that when the signal is quantized using increasing number of bits per sample as well as a higher prediction order it can have a proper audible reconstruction of the signal as well as a better compression due to decreasing  $e[n]$ .



It can also be seen that both the SNRs approximately intersect each other in a point when both  $(K, N) = (4, 4)$ . So the optimum point is seen somewhere around  $(K, N) = (4, 4)$  for both the *laughter* and the *handel* signals. But for *train* signal the optimum point will be at  $(K, N) = (5, 5)$ .

Table 7: Optimum SNR for trade-off between K(2-11) and N(1-6) for TRAIN Signal

$\frac{ N }{K}$	0	1	2	3	4	5	6
2	-19.59	-13.71	-8.21	-3.82	-1.84	-1.61	-1.61
3	-18.56	-12.72	-7.35	-3.24	-1.63	-1.44	-1.41
4	-17.40	-11.60	-6.41	-2.66	-1.33	-1.32	-1.32
5	-17.41	-11.62	-6.42	-2.67	-2.67	-1.31	-1.32
6	-16.10	-10.61	-5.42	-2.10	-1.20	-1.44	-1.43
7	-13.42	-7.96	-3.64	-1.24	-0.70	-1.38	-1.49
8	-9.51	-4.75	-1.76	-0.51	-0.25	-1.02	-1.01
9	-8.16	-3.78	-1.30	-0.37	-0.12	-0.81	-1.02
10	-5.80	-2.31	-0.70	-0.19	-0.04	-0.75	-0.68
11	-11.56	-6.37	-2.64	-0.83	-0.22	-0.65	-0.78

Table 8: Optimum SNR for trade-off between K(2-11) and N(7-10) for Train Signal

$\frac{ N }{K}$	7	8	9	10
2	-1.62	-1.63	-1.63	-1.63
3	-1.42	-1.43	-1.43	-1.42
4	-1.33	-1.33	-1.33	-1.33
5	-1.32	-1.32	-1.33	-1.33
6	-1.43	-1.43	-1.42	-1.42
7	-1.51	-1.59	-1.53	-1.54
8	-1.05	-1.09	-1.09	-1.09
9	-1.03	-1.10	-1.11	-1.12
10	-0.73	-0.75	-0.75	-0.74
11	-0.79	-0.72	-0.76	-0.77

So it can be seen from the table above that the optimum at Prediction Order,  $N = 4$  and Uniform quantization of Bits per sample,  $K = 10$  we got the highest SNR of -0.04 for *train* signal. Similarly the optimum SNR for trade-off between  $K$  and  $N$  for *laughter* as well as *handel* signals could be found. As these optimal values of  $K$  and  $N$  are determined for the three signals *train*, *laughter* and *handel*. Similarly this custom built GUI and MATLAB functions could be applied to any functions with after loading them as raw data inside MATLAB. So as discussed earlier in the introduction section the applications mentioned in the papers [2, 3, 4, 5, 6] could use the simulation process of this paper and increase the efficiency of their applications by using the optimal values of the bits per sample of the uniform quantization process in their applications.

## 5. Conclusion

This system successfully recreated both the encoder and the decoder of open-loop DPCM by applying some custom built MATLAB functions. It was basically used to find the trade-offs between the bits per sample of the uniform quantization process and the prediction order by comparing their SNRs. The results that were obtained could be used in variety of applications such as compression, de-noising, video coding, prediction, interpolation, and communications. The proposed technique of modeling and simulation of this paper is restricted to the application to DPCM simulation only. For an improvement to this paper, the proposed modeling and simulation technique could be applied to wide variety of digital filters like Kalman filter, wiener filter, LMS, RLS, AR, ARX, ARMA, ARMAX, IIR, FIR, FFT, IFT, DCT, DST etc.

## 6. References

- [1] N. S. Jayant, "Digital coding of speech waveforms: PCM, DPCM, and DM quantizers," Proc. IEEE, vol. 62 (May, 1974), pp. 611-632.
- [2] N. S. Jayant and P. Noll, Digital Coding of Waveforms, Englewood Cliffs, NJ: Prentice-Hall, 1984.
- [3] B. S. Atal and M. R. Schroeder, "Predictive coding of speech signals and subjective error criteria," IEEE Trans. Acoust., Speech, Signal Processing, vol. ASSP-27 (June 1979), pp. 247-254.
- [4] J. C. Asmuth and J. D. Gibson, "Sequential noise spectral shaping in DPCM," IEEE Trans. Acoust., Speech, Signal Processing, vol. ASSP-32, no. 2 (1984), pp. 228-235.
- [5] R. C. Maher, "Computationally efficient compression of audio signals by means of RIQ-DPCM," Applications of Signal Processing to Audio and Acoustics, 1993. Final Program and Paper Summaries., 1993 IEEE Workshop on, New Paltz, NY, 1993, pp. 35-38.
- [6] R. Achkar, G. A. Haidar and C. Mansour, "Real-time application of DPCM and ADM systems," Communication Systems, Networks & Digital Signal Processing (CSNDSP), 2012 8th International Symposium on, Poznan, 2012, pp. 1-6.
- [7] C. Mansour, R. Achkar and G. A. Haidar, "Simulation of DPCM and ADM Systems," Computer Modelling and Simulation (UKSim), 2012 UKSim 14th International Conference on, Cambridge, 2012, pp. 416-421.
- [8] B. P. Lathi. 1998. Modern Digital and Analog Communication Systems 3e Osece (3rd ed.). Oxford University Press.
- [9] Bernard Sklar. 1988. *Digital Communications: Fundamentals and Applications*. Prentice-Hall, Inc., Upper Saddle River, NJ, USA.
- [10] S. Hoque, F. Salauddin and A. Rahman, "Neighbour cell list optimization based on cooperative q-learning and reinforced back-propagation technique," Radio Science Meeting (Joint with AP-S Symposium), 2015 USNC-URSI, Vancouver, BC, Canada, 2015, pp. 215-215.
- [11] S. Rahman, A. Ahmed, F. Salauddin and A. Rahman, "HetNet performance analysis with asynchronous ABSF configuration employing horizontal sector offset scheme," Radio Science Meeting (Joint with AP-S Symposium), 2015 USNC-URSI, Vancouver, BC, Canada, 2015, pp. 216-216.
- [12] N. Hossain, M. T. Kabir, T. R. Rahman, M. S. Hossen and F. Salauddin, "A real-time surveillance mini-rover based on OpenCV-Python-JAVA using Raspberry Pi 2," 2015 IEEE International Conference on Control System, Computing and Engineering (ICCSCE), Penang, 2015, pp. 476-481.
- [13] F. Salauddin and T. R. Rahman "A Fuzzy based low-cost monitoring module built with raspberry pi - python - java architecture", International Conference on Smart Sensors and Application (ICSSA



## Biography



Fahim Salauddin completed his BEng. Degree in Electronics and Telecommunications Engineering from North South University, Dhaka, Bangladesh. Has multiple IEEE publications in Heterogeneous Networks and embedded systems. Currently pursuing his Master in Telecommunications and Network Engineering from La Trobe University, Melbourne, Australia. His research interest lies in Wireless Communications, Software Defined Networking, Internet of Things, Cloud Computing and embedded systems.





## Voltage Source Converter of Three Phase Photovoltaic Grid Connected System and Fault Analysis

B. Dhouib, H. Hadj Abdallah

CEM Lab, Department of electrical Engineering, National School of Engineering, University of sfax, BPW, 3038

dhouib.bilel@gmail.com

http://www.enis.tn

### Abstract

This paper develops a multilevel structure based on the modeling and control of a Photovoltaic (PV) application connected to a three-phase grid. The DC-DC boost converter boosts the DC voltage of the PV array to the Maximum Power Point (MPP) using a Maximum Power Point Tracking (MPPT) based on the incremental conductance method. For synchronization, a three-phase inverter is necessary to connect the PV system to the grid. The control system modeling of three phase inverter was carried out under Matlab / Simulink environment using the proportional integral controllers, pulse width modulation (PWM) three-level pulse generator technique and park transformation. The Phase Locked Loop (PLL) is used to synchronize the inverter current angle with the angle of the grid voltage to reach a power factor as close to one as possible. As a final point, different types of fault condition are created, simulated and analyzed on the grid side.

**Keywords:** photovoltaic (PV), Maximum power point tracking (MPPT), pulse width modulation (PWM), voltage source converter (VSC), fault analysis

### Nomenclature

$I_D$	The diode current (A)
$V_d$	The diode voltage (V)
$I_{sat}$	The diode saturation current (A)
$V_T$	The thermal voltage
$T$	The cell temperature (K)
$K$	The Boltzmann constant, equal to $1.3806e^{-23} (J \cdot K^{-1})$
$q$	The electron charge, equal to

$$1.6022e^{-19} (C)$$

$Q_d$	The diode quality factor
$R_{sh}$	The shunt resistance
$R_s$	The series resistance
$N_{cell}$	The number of series-connected cells per module
$N_{ser}$	The number of series-connected module per string
$N_{pp}$	The number of parallel strings
$\mathcal{G}_{base}$	The base voltage ( $\mathcal{G}_{rms}$ line-to-line).
$P_{sc}$	The inductive three-phase short circuit power in (VA)
$f$	The frequency in (HZ)
$X$	The reactance in ( $\Omega$ )
$(X/R)$	The ratio

### 1. Introduction

Today, the energy demand in the world is in full evolution. However, the stock of oil in our planet will soon be exhausted. The global warming of the planet today becomes more serious due to the greenhouse effect. Some emissions of these gases are due to human activity. To reduce these emissions and ensure energy security, renewable energy is enhanced in the production of electrical energy while preserving our fossil deposits (oil and gas) as long as possible with a lesser pollution and controlled.

In recent years, there has been a growing interest in PV solar energy as it is a potential source for electricity



generation with minimal environmental impact [1]. This energy is abundant, distributed through the earth, pollution free and clean and noise-free source of energy [2]-[3].

Direct exploitation of solar energy falls within three distinct technologies: one produces calories, it is solar thermal, the second is thermoelectric generators, and the third produces electricity, it is photovoltaic (PV) solar energy, which is the subject of this paper. The growing interest in photovoltaic systems requires the growth of the activities of research and development in various aspects such as Maximum Power Point Tracking (MPPT) [4], PV arrays, anti-Islanding protection, stability and reliability, the electronic interface of power quality and power. The MPPT is used to control variations on the curve current voltage of the cells. Thus the MPPT system must track the point of optimal functioning of the PV arrays. The purpose of this technique is to ensure that the system operates very close to the optimal operating point. In regards to power electronic converter interface PV array to the grid, a DC-DC boost converter and a three-phase three-level Voltage Source Converter (VSC) are a topology widely used to this day. We used Matlab/Simulink environment to model the control system of three phase inverter using the proportional integral controllers, pulse width modulation (PWM) three-level pulse generator technique and park transformation. To get the power factor as close as possible to one, we use the Phase Locked Loop to synchronize the inverter current angle with the angle of the grid voltage.

Finally, fault analyses is carried by creating a line-to-ground (LG), line-to-line (LL), double line-to-ground (LLG) fault in the network and observe the ac voltage, ac current and ac power waveforms at the grid side with and without different types of fault condition. The remainder of the paper is organized as follows: Section (2) focuses on description of the grid connected PV system. Section (3) emphasizes on PV array model. Section (4) is dedicated to the control system of PV solar systems. Section (5) presents the grid model. Section (6) provides a calculation of asymmetrical short-circuit current: Method of symmetrical components. Our results are analyzed and discussed in section (7). The main conclusions are drawn in section (8).

## 2. System description

The principal schematic diagram of the grid connected PV system is presented in figure 1. The PV module is usually composed of a number of solar cells with identical characteristics. Similarly, a number of PV modules are assembled and interconnected to build a PV array. The PV array generate  $72.6KW$  under standard test conditions ( $25^\circ C$ ,  $1000W/m^2$ ). The voltage

level of the PV array  $243V$  is boosted to  $400V$  via a DC-DC boost converter using MPPT based on the incremental conductance method. This dc power is converted into ac power using a three level bridge inverter. This inverter has three legs with two switches in each leg. The switching is performed by carrier-based or

space-vector based pulse width modulation. The converter produces an output waveform very close to a sinusoidal wave with extremely low harmonic distortion levels. The output  $L_f$  filter is connected to remove high switching frequency components from output current of inverter [5]. A delta-star step up transformer configuration is generally used in grid connected system because the third harmonic will get circulated in delta and does not enter in the grid. To produce the pulses for the three-level bridge inverter, a  $dq$  control uses a reference frame transformation  $abc$  to  $dq$  frame which transforms the grid current and grid voltage PLL into  $dq$  frame.

## 3. PV array model

The basic equation that describes the I-V characteristics of the PV model is given by the following equation [2]-[6]:

$$I_D = I_{sat} \left[ \exp(V_d / V_T) - 1 \right] \quad (1)$$

$$I = N_{pp} I_L - N_{pp} I_{sat} \left( e^{\left[ \frac{V + R_s I \left( \frac{N_{ser}}{N_{pp}} \right)}{V_T N_{ser}} \right]} - 1 \right) - \frac{V + R_s I \left( \frac{N_{ser}}{N_{pp}} \right)}{R_{sh} \left( \frac{N_{ser}}{N_{pp}} \right)} \quad (2)$$

where:

$$V_T = \frac{N_{cell} K T Q_d}{q} \quad (3)$$

## 4. Control system

The system has multiple control blocks that work together to ensure maximum power extraction from the PV array and then converting it to AC power to be injected into the grid. In this section, we discuss the details of each control block in the system.

### 4.1. Control of DC-DC boost converter

The DC-DC boost converter boosts the DC voltage of the PV array to the MPP using an MPPT based on the incremental conductance method. This method computes the maximum power point by comparison of the incremental conductance  $(\Delta I / \Delta V)$  to the array conductance  $(I / V)$ . When these two are the same  $(I / V = \Delta I / \Delta V)$ , the output voltage is the MPP voltage. The controller maintains this voltage until the irradiation changes and the process is repeated. The incremental conductance is a technique that takes advantage of the fact that the slope of the power-voltage curve is zero at the maximum power point. The slope of the power-voltage curve is positive at the left of the MPP and negative at the right of the MPP [7] as given by:





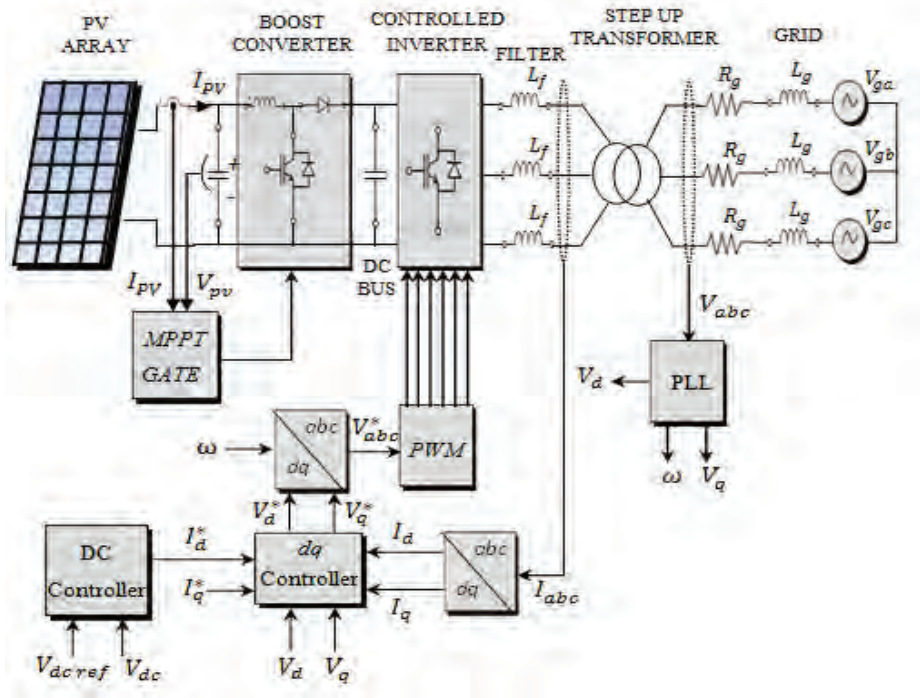


Figure 1. Schematic diagram of the grid connected PV system

$$\begin{cases} dP/dV = 0, & \text{at MPP} \\ dP/dV > 0, & \text{left of MPP} \\ dP/dV < 0, & \text{right of MPP} \end{cases} \quad (4)$$

since

$$\frac{dP}{dV} = \frac{d(IV)}{dV} = I + V \frac{dI}{dV} \cong I + V \frac{\Delta I}{\Delta V} \quad (5)$$

Therefore the equation (4) can be rewritten as:

$$\begin{cases} \Delta I / \Delta V = -I / V, & \text{at MPP} \\ \Delta I / \Delta V > -I / V, & \text{left of MPP} \\ \Delta I / \Delta V < -I / V, & \text{right of MPP} \end{cases} \quad (6)$$

We can find the MPP by comparing the instantaneous conductance ( $I/V$ ) to the incremental conductance ( $\Delta I / \Delta V$ ) as shown in figure 2. This idea is presented in [8].

This technique has an advantage over the perturbation and observation ( $P \& O$ ) method because it can determine when you reach the MPP without having to oscillate around this value. It can also perform MPPT under rapidly increasing and decreasing irradiance conditions with higher accuracy than the perturbation and observation ( $P \& O$ ) method.

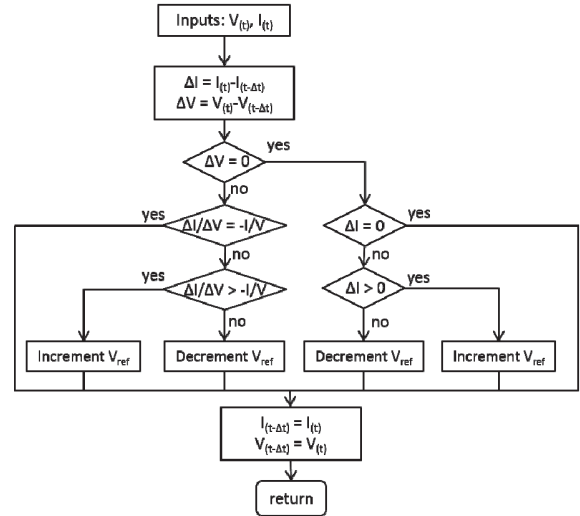


Figure 2. Flowchart for an Incremental Conductance Tracking System

#### 4.2. Control of voltage source converter (VSC)

The three level VSC regulates DC bus voltage and keeps unity power factor. The control system uses two control loops: an external control loop which regulates DC link voltage and an internal control loop which regulates  $I_d$  and  $I_q$  grid currents (active and reactive current components).  $I_d$  current reference is the output of the DC voltage external controller.  $I_q$  current reference is set to zero in order to maintain unity power factor.  $V_d$  and  $V_q$  voltage outputs of the current controller are



converted to three modulating signals  $U_{ref\_abc}$  used by the PWM three level pulse generator [9]. The determination of the grid voltage vector angle is done by a phase-locked loop (PLL) algorithm.

The grid voltage vector is used in a feed forward loop to compensate for the grid harmonics [10]. The voltage and power equations by the inverter in  $d-q$  synchronous reference frame are represented below:

$$\begin{cases} V_d^* = RI_d + V_d - \omega LI_q + L \frac{d}{dt} I_d \\ V_q^* = RI_q + V_q - \omega LI_d + L \frac{d}{dt} I_q \end{cases} \quad (7)$$

$$\begin{cases} P = V_d I_d + V_q I_q \\ Q = -V_d I_q + V_q I_d \end{cases} \quad (8)$$

The voltages presented by equation (7) in the  $d-q$  reference are coupled. Figure 3 shows how compensation is made for the coupling of the axes  $d$  and  $q$ . From the voltages equation by the inverter in  $d-q$  synchronous reference frame, we obtain the following decoupled voltages equation [11]:

$$\begin{cases} V_d^* = RI_d + V_d - \omega LI_q + K_p (I_d^* - I_d) + K_i \int (I_d^* - I_d) dt \\ V_q^* = RI_q + V_q + \omega LI_d + K_p (I_q^* - I_q) + K_i \int (I_q^* - I_q) dt \end{cases} \quad (9)$$

The bloc diagram is presented in figure3.

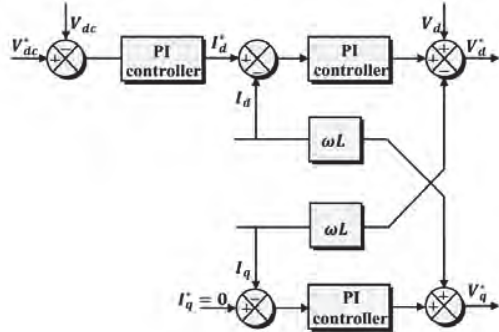


Figure 3. Compensation of the cross coupling between axes

#### 4.3. Filter inductance $L_f$

To reduce the switching losses in the power components of the inverter, and aimed at improving the load current (injected current), was added an inductance [12]. The value of  $L_f$  is design based on current ripple. Typically the ripple current can be chosen as 15% - 25% of rated current. The maximum current ripple [13]-[14] can be resulting as following:

$$\Delta i_{L_{max}} = \frac{1}{8} \cdot \frac{V_{dc}}{L_f f_{sw}} = 20\% \cdot i_{rated} \quad (10)$$

#### 4.4. Phase locked loop (PLL)

The PLL command is necessary in the control of the converters. Different methods to extract phase angle have

been developed and presented in many papers up to now [15]-[16]. The most common method for three-phase system is that based on the representation in the referential Park of the measured voltages on the network. The principle is to consider the equations of the three-phase network in a reference Park whose orientation is such that  $V_q = 0$  [17].

The phase locked loop achieves the slaving an arbitrary phase angle to the reference angle. The simulink model for a three-phase PLL is shown in figure 4.

As it can be observed, a PID controller is used in order to reduce the error between the reference and measured values of  $V_q$ . Deduce  $dq$  components from  $abc$  signals by performing an  $abc$  to  $\alpha\beta$  Clarke transformation in a fixed reference frame, then perform an  $\alpha\beta$  to  $dq$  transformation in a rotating reference frame to obtain the measured value  $V_q$ .

## 5. Grid model

The grid was modeled as a Y connected a balanced three-phase voltage source with an internal  $R_g - L_g$  impedance [18]. You can specify the source internal resistance and inductance either directly by entering  $R_g$  and  $L_g$  values or indirectly by specifying the source inductive short-circuit level and  $X/R$  ratio. The internal inductance and resistance are defined as:

$$L_g = \frac{g_{base}^2}{P_{SC}} \cdot \frac{1}{2\pi f} \quad (11)$$

$$R_g = \frac{X}{(X/R)} \cdot \frac{2\pi f L_g}{(X/R)} \quad (12)$$

## 6. Calculation of asymmetrical short-circuit currents: Method of symmetrical components

Any type of sinusoidal waveform (voltage, current, flux ...) can be written in terms of its symmetrical components as follows [19]:

$$\begin{bmatrix} X_a \\ X_b \\ X_c \end{bmatrix} = [F] * \begin{bmatrix} X_1 \\ X_2 \\ X_0 \end{bmatrix} \quad (13)$$

with

$$[F] = \begin{bmatrix} 1 & 1 & 1 \\ a^2 & a & 1 \\ a & a^2 & 1 \end{bmatrix} \text{ and } a = e^{j\frac{2\pi}{3}}$$





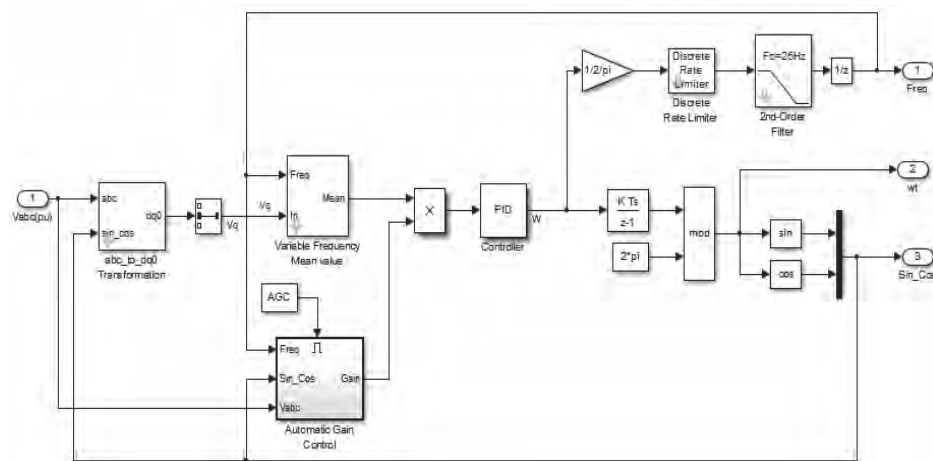


Figure 4. The Simulink model for a three-phase PLL

The sequences positive, negative and zero are determined by:

$$\begin{bmatrix} X_1 \\ X_2 \\ X_0 \end{bmatrix} = [F]^{-1} * \begin{bmatrix} X_a \\ X_b \\ X_c \end{bmatrix} \quad (14)$$

## 7. Simulation results

In this section we present the simulation results of the proposed grid connected PV system presented in figure 1.

### 7.1. Simulation of PV system

The PV array consists of 66 strings of 5 series-connected modules connected in parallel. The total power is  $(66 * 5 * 220W = 72.6KW)$ . Manufacturer specifications for one module are shown in Appendix (Table 1).

Figures 5, 6, 7 and 8 shows the output characteristics of PV arrays. These curves are nonlinear and are crucially influenced by solar radiation and temperature.

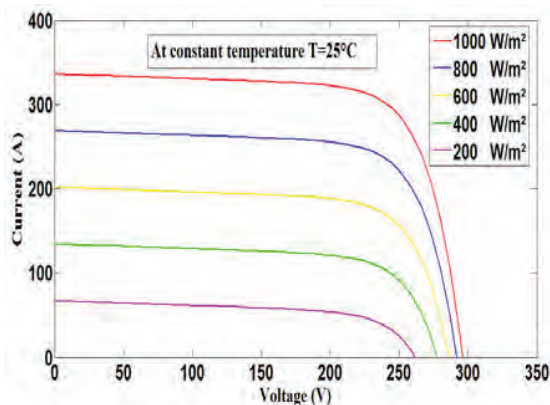


Figure 5. V-I characteristics of array under constant temperature and different irradiance

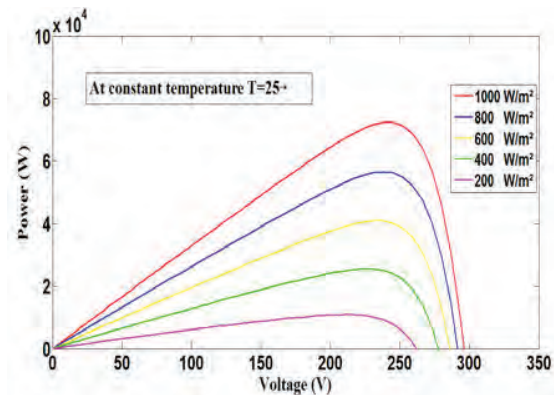


Figure 6. V-P characteristics of array under constant temperature and different irradiance

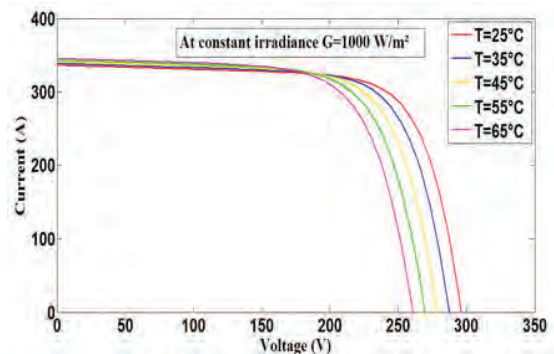


Figure 7. V-I characteristics of array under constant irradiance and different temperature

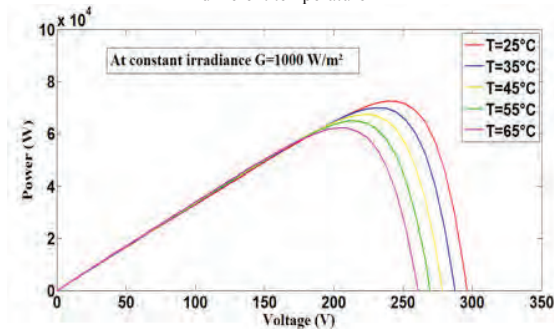


Figure 8. V-P characteristics of array under constant irradiance and different temperature



### 7.2. Simulation of grid connected PV system without fault

The grid connected PV system without fault in figure 1 is simulated by using MATLAB/Simulink software environment in order to validate the control methodology discussed earlier. Parameters of the test system are summarized in Appendix (Table 2).

For all simulations, the temperature is assumed constant at  $25^{\circ}\text{C}$ . Under steady-state condition, (i.e. constant solar irradiance  $G = 1000\text{W}/\text{m}^2$ ), some simulation results have been chosen to illustrate the system response at standard test condition (STC).

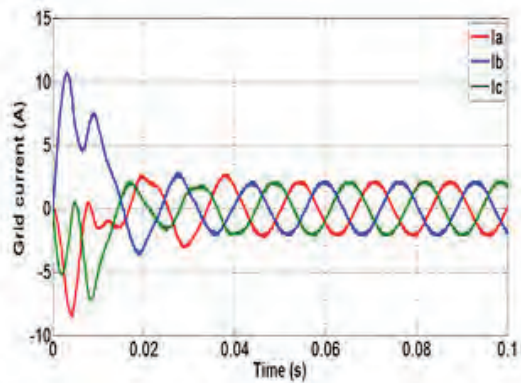


Figure 9 (a). The three phase grid current waveform

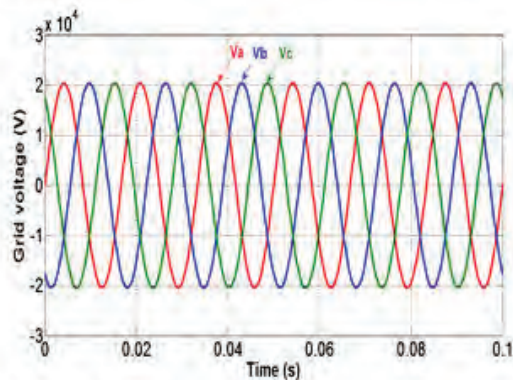


Figure 9 (b). The three phase grid voltage waveform

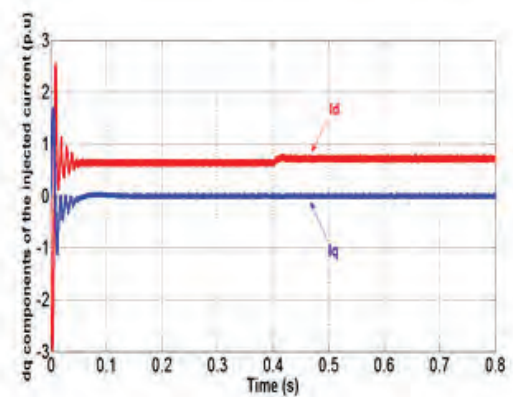


Figure 9 (c). dq components of the injected current

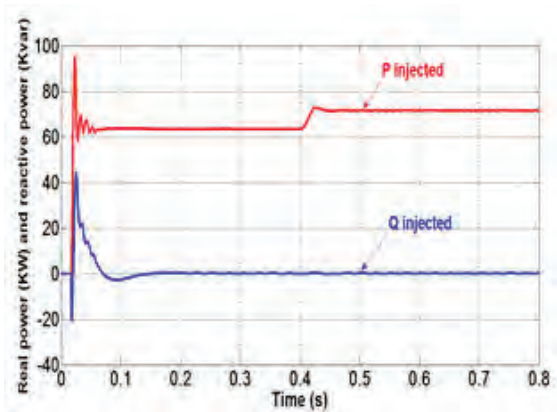


Figure 9 (d). Real power and reactive power

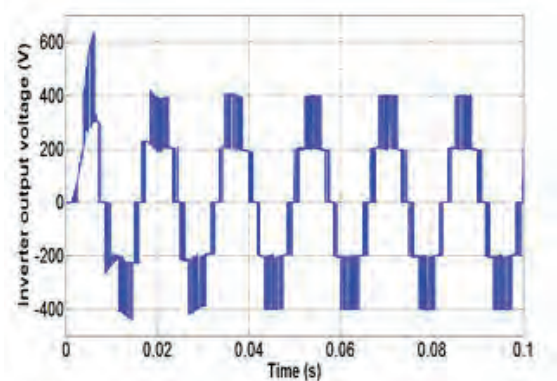


Figure 9 (e). Inverter output voltage

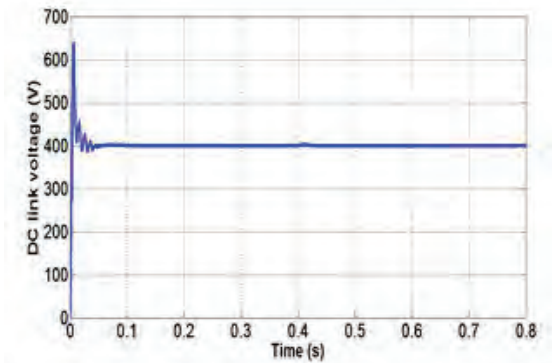


Figure 9 (f). DC link voltage

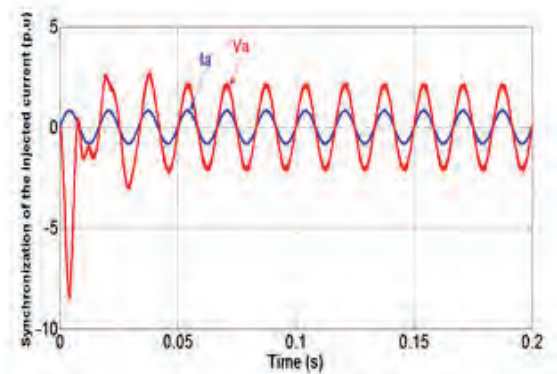


Figure 9 (g). Dynamic response of synchronization of the injected current



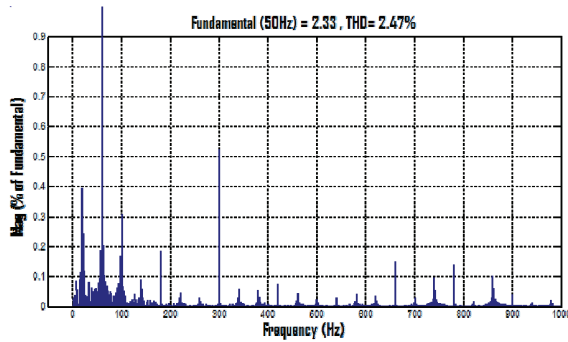


Figure 9 (h). The total harmonic current distortion in frequency domain

The three phase grid current and grid voltage waveforms are exposed in Figures 9(a) & 9(b) respectively. As can be seen, the system response under STC is very good where the steady-state conditions are reached in few AC periods. The  $dq$  components of the injected current are shown in Figure 9(c) which follow closely the references  $I_d^*$  and  $I_q^*$ . The real power and reactive power injected from the PV system are shown in Figure 9(d). The injected real power was around 71KW while reactive power was set to zero. To eliminate the high frequency harmonic in Figure 9(e), low-pass filter is connected. The DC link voltage was controlled at a steady state value of about 400V as shown in Figure 9(f). The injected currents must be synchronized with the grid voltages. So, the PLL has been used to satisfy this condition. The dynamic response of synchronization of the injected current is shown in Figure 9(g). The total harmonic distortion (THD) of the current in frequency domain is shown in Figure 9(h). The THD of current injected into the grid is 2.47% which satisfies IEEE 519 standard limits.

### 7.3. Effect of irradiation

In order to investigate the effectiveness of the control algorithms, a dynamic simulation is carried out with solar irradiance suddenly dropped from  $1000W/m^2$  to  $250W/m^2$  at 0.5sec as shown in Figure 10(a).

The effect of irradiation on PV power generation is demonstrated in figure 10. The PV array output current, voltage and power during simulation run are shown in Figures 10(b), 10(c) and 10(d) respectively. It may be noted that the effect of solar irradiance on the array terminal voltage is small compared to its effect on output current.

The simulation results of irradiation effect on PV connected to grid are illustrated in figure 11. The active and reactive powers are shown in Figure 11(a). The reactive power drops from 71KW to 14KW after 0.5sec when the reactive power is maintained equal to zero. From the simulation curve in figure 11(b), can be distinguished that the grid current amplitude decreases in response due to the sudden change of the PV generated power.

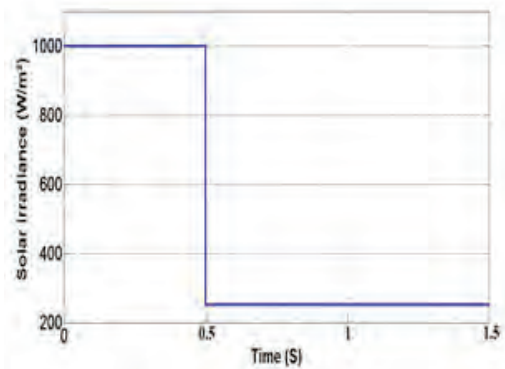


Figure 10 (a). The solar irradiance

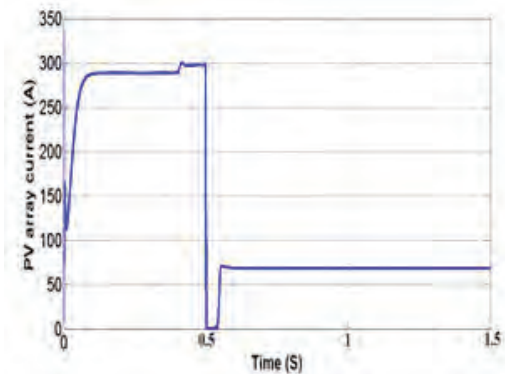


Figure 10 (b). The PV array current

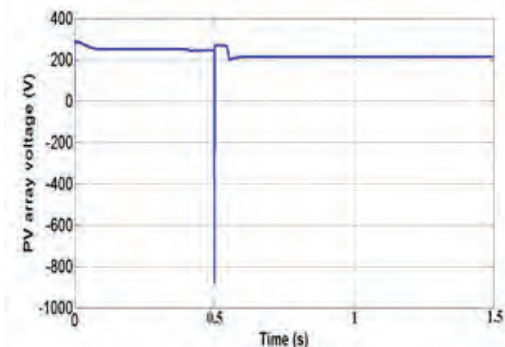


Figure 10 (c). The PV array voltage

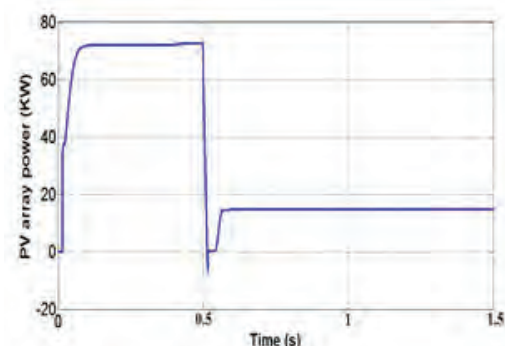


Figure 10 (d). The PV array power





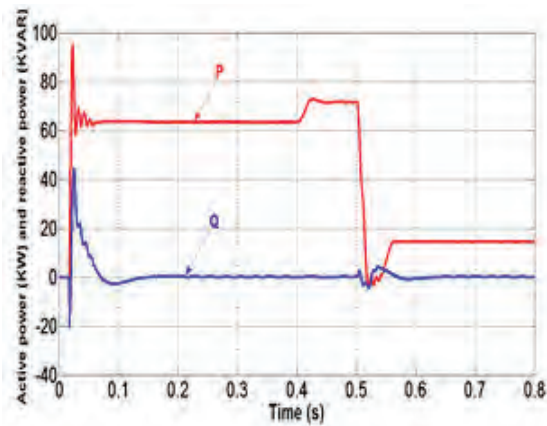


Figure 11 (a). Active and reactive power injected to the grid

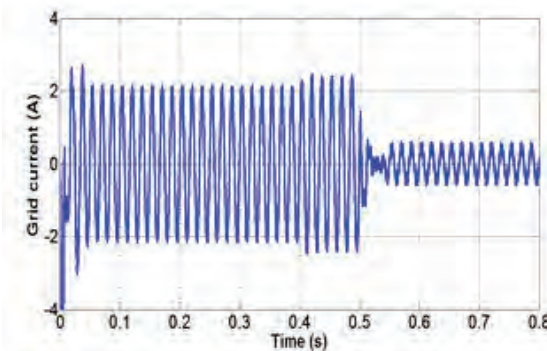


Figure 11 (b). The grid current

#### 7.4. Simulation of grid-connected PV system with fault

The system is simulated at temperature  $T = 25^{\circ}\text{C}$  and irradiance  $G = 1000\text{W} / \text{m}^2$ . We applying a fault on the grid side at  $t = 0.55\text{sec}$  and the fault duration is  $0.05\text{sec}$ .

- Line-to- ground (LG) fault

Due to LG fault, the voltage  $V_a$  drops to zero as shown in figure 12. Application of fault on the grid side has resulted in oscillations in current. However, oscillations are damped as soon as the fault is cleared, and the system tracks the reference current in less than 0.2 sec. The injected current into the grid is no longer sinusoidal. This disconnection creates an increase over rated currents of the three phases currents simultaneously as shown in figure 13, this case study clearly shows an increase equal to 16.16 times of the rated current for phase A, whereas it is equal to 17.44 times for phase B and 14.24 times for phase C (see Table 3 in Appendix). In addition, this voltage failure causes a slight decrease in the level of active and reactive powers. In figure 14, the decrease of the active power is about 0.93 times of the rated power (see Table 3 in Appendix).

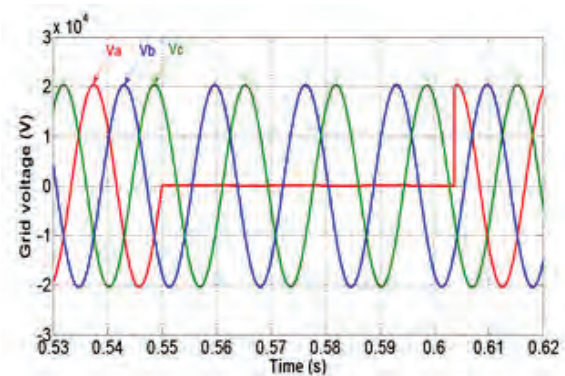


Figure 12. The grid voltage with LG fault

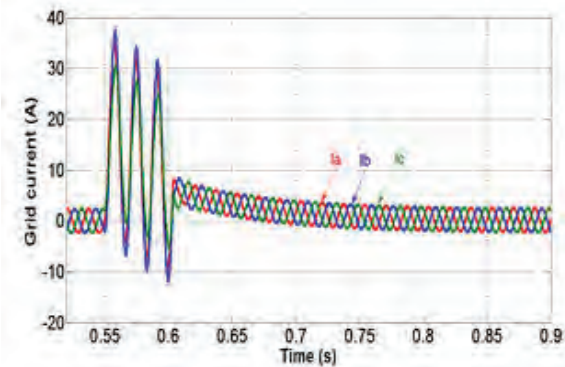


Figure 13. The grid current with LG fault

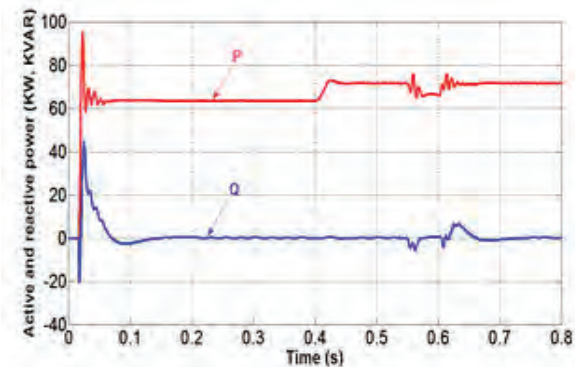


Figure 14. The active and reactive power with LG fault

- Line-to- line (LL) fault

When applying the LL fault, it can be observed from figure 15 that two phases A and B are in short-circuit during a period of fault. As a result, application of fault on the grid side has resulted in oscillations in current so that an enhances observed as shown in figure 16; this injected current into the grid is no longer sinusoidal and this boost is less important than the LG fault. For phase A, an increase of 2.17 times is reached, while for phase B an increase of 1.81 times and for phase C an increase of 2.5 times are obtained (see Table 3 in Appendix). This case study clearly shows an decrease in active power is more important for this type of fault than for the LG fault as shown in figure 17, and this decrease is 0.86 times (see Table 3 in Appendix).



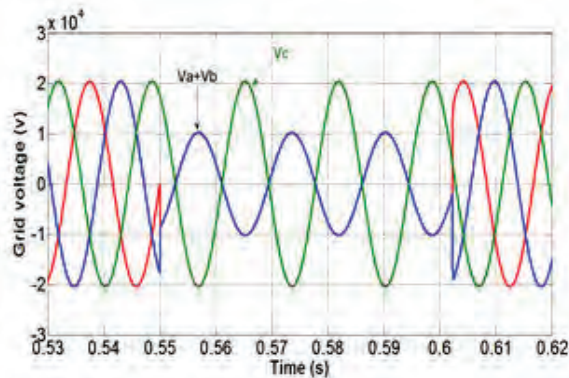


Figure 15. The grid voltage with LL fault

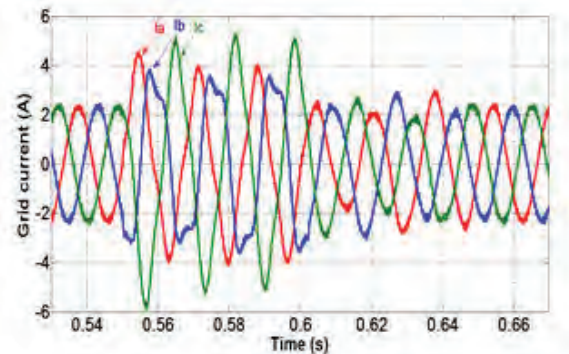


Figure 16. The grid current with LL fault

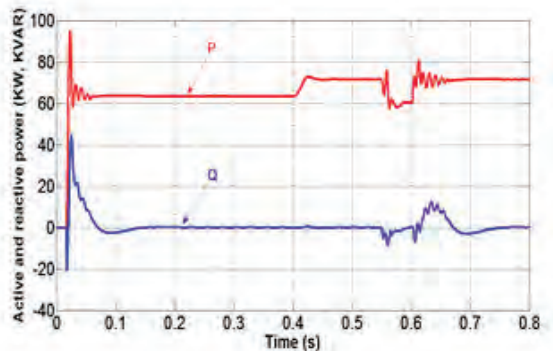


Figure 17. The active and reactive power with LL fault

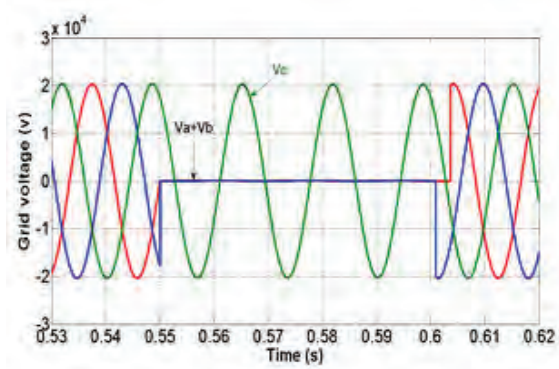


Figure 18. The grid voltage with LLG fault

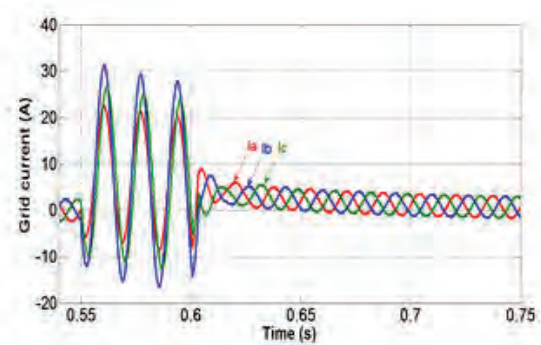


Figure 19. The grid current with LLG fault

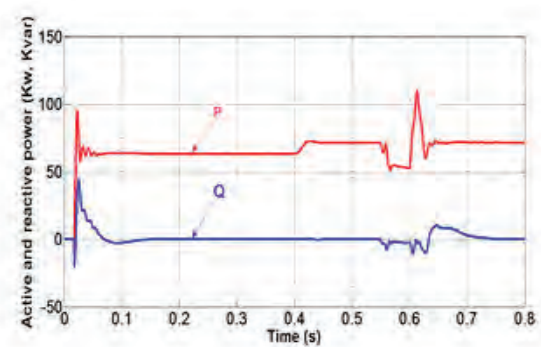


Figure 20. The active and reactive power with LLG fault

- Line-to- line to ground (LLG) fault

The different simulations of LLG fault are shown in the following figures. As shown in figure 18, phases A and B are grounded. This fault applied in the grid side causes an increase of the phase currents. However, this increase is damped as soon as the fault is cleared and the system tracks the reference current. This increase is allocated as follows: phase A- 10.72 times, phase B- 14.84 times and Phase C- 12.62 times (see Table 3 in Appendix). This increase is smaller than the LG fault but at the same time larger than the LL fault as shown in figure 19. During fault period, the active and reactive power decrease in figure 20 is less than LG and LL faults. The decrease in active power is 0.71 times (see Table 3 in Appendix).



## 8. Conclusion

In this paper, a grid-connected PV system based on MATLAB has been proposed. The main objectives were to achieve maximum power output from the PV array and to inject a high quality AC current into the grid.

Based on the modeling system, MPPT, steady state and dynamic performances, and fault analysis are studied. The PLL has been designed for grid synchronization and it effectively synchronizes the inverter voltage and frequency with the grid voltage and frequency. The steady state and dynamic performances of the proposed system have been tested under constant solar irradiation and fast changing solar irradiation. The presented simulation results show a good system behavior under all these case studies.

Fault analysis on grid side have been performed for various fault conditions like LG, LL, LLG faults. In case of fault, to become stable at nominal frequency, it is



observed that the system tracks the reference current in less than 0.2 sec. Application of fault on the grid side has resulted in current oscillations. The injected current into the grid is no longer sinusoidal. Disconnections create an increase over rated currents of the three phase currents simultaneously. In addition, this voltage failure causes a slight decrease in the level of active and reactive powers. The results of simulations show that the interruption due to phase to ground faults are noticeably more dangerous than the line to line faults. The decreasing of active power depends on the number of phases in fault. Nearly all PV systems will soon be required to have a fault protective device that will minimize the damages in PV arrays.

## 9. Appendix

- Manufacturer specifications for one module are shown in table 1

TABLE 1  
ELECTRICAL CHARACTERISTIC FOR ONE  
MODULE

Symbol	Manufacturer	Rating values
$P_{max}$	Maximum power	220W
$N_{cells}$	Number of series-connected cells	96
$V_{OC}$	Open-circuit voltage	59.2618V
$I_{SC}$	Short-circuit current	5.09261A
$V_{mp}$	Voltage at maximum power	48.3159V
$I_{mp}$	Current at maximum power	4.54758A

- System parameters used in simulation are shown in table 2

TABLE 2  
SYSTEM PARAMETERS USED IN SIMULATION

Components	Rating value
<b>DC link:</b>	
Capacitance	12000 $\mu$ F
Reference $V_{dc}$	400V
<b>Passive L Filter:</b>	
Inductance: L	250 $\mu$ H
Resonance frequency	50HZ
R (in series with L)	0.002 $\Omega$
<b>Isolation Transformer:</b>	Step-up
Apparent power: S	100KVA
Primary side	25KV ( $L - L_{rms}$ )
Secondary side	230V ( $L - L_{rms}$ )
<b>3 phase AC distribution grid:</b>	
Phase-to-phase rms voltage	25KV
Frequency	50HZ
3 phase short circuit level	100MVA

- Phase currents and active power variations during different fault conditions are shown in table 3

TABLE 3  
PHASE CURRENTS AND ACTIVE POWER  
VARIATIONS DURING DIFFERENT FAULT  
CONDITIONS

FAULT	PHASE A	PHASE B	PHASE C	ACTIVE POWER
LG	1616 %	1744 %	1424 %	93 %
LL	217 %	181.4%	250 %	86%
LLG	1072 %	1484 %	1262 %	71

## 10. References

- [1] Hyuntae Choi, Mihai Ciobotaru. High gain DC/DC converter for the grid integration of large-scale PV systems, pp. 1011-1016, IEEE 2012.
- [2] K.Manohar, P.Sobha Rani. Mppt and simulation for a Grid-Connected Photovoltaic System and Fault analysis. The International Journal of Engineering and Science (IJES) pp. 158-166, 2012.
- [3] S. MALLIKA and R. SARAVANAKMAR. Closed Loop Current Control of Three Phase Photovoltaic Grid Connected System. International Journal of Electronics Communications and Electrical Engineering. Volume 5 (Issue 2) ISSN : 2277-7040, May 2015.
- [4] N. Ammasai Gounden, Sabitha Ann Peter. Fuzzy logic controller with MPPT using line-commutated inverter for three-phase grid-connected photovoltaic systems, Renewable energy journal n 34. Elsevier pp. 909-915, 2009.
- [5] T. Wanjekeche, D.V. Nicolae, A.A. Jimoh, Modeling and control of a cascaded NPC/H-bridge inverter with LCL filter in PV-grid application, IPEC 2010, IEEE 2010.
- [6] Chih-Ming Hong, Chiung-Hsing Chen. Intelligent control of grid-connected wind-photovoltaic hybrid power systems. Electrical power & energy systems journal 55 – Elsevier pp. 554-561, 2014.
- [7] Divya Teja Reddy Challa, I, Raghavendar, Implementation of Incremental Conductance MPPT with Direct Control Method Using Cuk Converter. International Journal of Modern Engineering Research (IJMER) pp-4491-4496, 2012.
- [8] M. Abdelkadir, A.S. Samosir, A.H.M. Yatim and S.T. Yusuf. A New Approach of Modelling, Simulation of MPPT for Photovoltaic System in Simulink Model. ARPN Journal of Engineering and Applied Sciences Vol. 8, No. 7, July 2013.
- [9] V. HimaLeela, S. Thai Subha. Control of power converter for power quality improvement in a grid connected PV system. IEEE International conference on circuits, power and computing technologies ICCPCT- pp. 26-30, 2013.
- [10] Hui Zhang; Hongwei Zhou; Jing Ren; Weizeng Liu; ShaohuaRuan; YongjunGao, "Three-Phase Grid-Connected Photovoltaic System with SVPWM Current Controller," Proceedings Of IEEE 6th International Conference on Power





- Electronics and Motion Control (IPEMC). pp. 2161-2164, May, 2009.
- [11] Ahmed S.Khalifa and Ehab F. EI-Saadany. Control of Three Phase Grid Connected Photovoltaic Power Systems. IEEE 2010.
  - [12] Rihab Mahjoub Essefi, Mansour Souissi, Hsan Hadj Abdallah, Current Control Strategy for Grid Connected Photovoltaic Inverter via LCL Filter, International Review on Modelling and Simulations (IREMOS), 6 (5), pp. 1426-1434, 2013.
  - [13] Miss. Sangita R Nandurkar, Mrs. Mini Rajeev. Design and Simulation of three phase Inverter for grid connected Photovoltaic systems. Proceedings of Third Biennial National Conference, NCNTE, Feb 24-25, -2012.
  - [14] Sibasish Panda, Anup Kumar Panda and H.N Pratihari. Fault Analysis on Grid Connected MPPT based Photovoltaic System. International Journal of current Engineering and Technology Vol. 3, No. 3, August 2013
  - [15] P. Paramita Das, Mehrdad Kazerani, "Dynamic Modeling and Performance Analysis of a Grid-Connected Current-Source Inverter-Based Photovoltaic System" in Proc IEEE Trans. sustainable energy, vol.2, no. 4, October 2011.
  - [16] Ryn Marouani, Kamel Echaieb and Abdelkader Mami. Sliding Mode Controller for Buck-Boost dc-dc Converter in PV Grid-Connected System. IEEE 2012.
  - [17] Mihai Ciobotaru, Remus Teodorescu, Vesalius G Agelidis, Offset rejection for PLL based synchronization in grid-connected converters. Applied power electronics conference and Exposition.APEC-.23rd annual IEEE. pp. 1611-1617, 2008
  - [18] Riad Kadri, Jean-Paul Garbert, Member, IEEE and Gerard champenois, Member, IEEE. An Improved Maximum Power Point Tracking for Photovoltaic Grid-Connected Inverter Based on Voltage-Oriented Control. IEEE transactions on industrial electronics, vol.58, No 1, January 2011.
  - [19] N. Umamaheswari, P.SrinivasRaju, K.Sravanthi, K.Kalyan Kumar. Performance analysis of CSI Based PV system During LL and TPG faults. IOSR Journal of Electrical and Electronics Engineering (IOS-JEEE) pp. 101-107, 2013.

## Biographies



**Bilel Dhouib** was born in Tunisia in 1986. He received the degree in electrical engineers in 2011, The M.S. degree in electrical conversion and renewable energies in 2012 from the National School of Engineering of Sfax-Tunisia, her research interest include study the dynamic behavior of electrical network equipped with renewable sources of energy.



**Hssan Hadj Abdallah** is currently professor the Department of Electrical Engineering of National School of Engineering of Sfax-Tunisia at University of Sfax and member in the "CEMLab" Laboratory ENIS- Sfax. He received his Mastery in electrical engineering from the superior normal school of technical teaching of Tunis-Tunisia in 1982, the diploma in-depth studies in electrical engineering from the superior normal school of technical teaching of Tunis-Tunisia in 1984, the Ph.D in electrical engineering from the superior normal school of technical teaching of Tunis-Tunisia in 1991 and Habilitation University in electrical engineering from National school of engineering of Sfax in 2007. His main research interests are electrical power system (EPS), the dispatching and the stability of the EPS, wind energy and intelligent techniques applications in the EPS. He is authors and co-authors of about 100 papers in international journals and national and international conferences.









## Sensor less Control of PMSM with FOC using MRAS

G.Swapna, N.KrishnaKumari, D.Ravi Kumar

M.Tech Power Electronics Student, EEE Dept., Engineering, VNR VJIET, Hyderabad, Telangana, India

Assoc. Prof, EEE Dept., Engineering, VNR VJIET, Hyderabad, Telangana, India

Assist. Prof, EEE Dept., Engineering, VNR VJIET, Hyderabad, Telangana, India

gswapna.2468@gmail.com, nkkpsg@gmail.com, ravi44d@gmail.com

### Abstract

Sensor less Control of PMSM with FOC using MRAS for speed estimation is implemented through Popov's Hyper stability criterion. The output of the adaptation mechanism MRAS is the estimated speed quantity using PI controller. The aim of the proposed sensorless control is to improve performance and robustness of PMSM drive under load and speed variations. The PMSM drive is tested for three different cases; with balance three phase supply, FOC and with MRAS using PI controller. The effectiveness and validity of the proposed control approach is verified by simulation results through MATLAB/Simulink/Sim Power System environment. It is found that the performance of the PMSM drive is better and also the torque, flux ripples are quite less with MRAS.

**Keywords:** Permanent magnet synchronous motor (PMSM), Field oriented control (FOC), Model reference adaptive system (MRAS).

### Nomenclature

$V_{ds}$	direct axis stator voltage, V
$V_{qs}$	quadrature axis stator voltage, V
$i_{ds}$	direct axis stator current, A
$i_{qs}$	quadrature axis stator current, A
$R_s$	Stator armature resistance, $\Omega$
$p$	no. of poles
$L_{ds}$	direct axis inductances, H
$L_{qs}$	quadrature axis inductances, H
$\lambda_{ds}$	direct axis flux linkage, wb
$\lambda_{qs}$	quadrature axis flux linkage, wb
$\lambda_f$	magnetic flux linkage, wb
$\omega_e$	rotor speed in electrical, rpm
$\omega_m$	mechanical speed, rad/s
$J$	moment of inertia, $\text{kg.m}^2$
$B$	Viscous Friction Co-efficient, $\text{Nm/rad/s}$
$P$	Differential operator
$T_e$	electromagnetic torque, Nm
$T_L$	load torque, Nm

### 1. Introduction

As PMSM Motor is made up of rare earth and neodymium boron magnets, it has been widely used in high performance variable speed industrial applications. In this motor, Permanent Magnets are placed in the rotor; because of absence of windings in the rotor; rotor copper losses are zero. Due to these advantages, this motor offers high efficiency, high torque to inertia, high Power density [1]. PMSM are preferred in applications where it requires fast torque response and high performance operations [2] such as robotics, electrical vehicles, and servo applications [3, 4]. Both Permanent Magnet Synchronous Motor (PMSM) and Brushless DC motor (BLDCM) have permanent magnets on the rotor and require alternating stator currents to produce constant torque. But the torque ripples of the BLDCM are higher than that of the PMSM [1].

The scalar control is an open loop speed control method, doesn't provide a possibility to control the currents during various operation cycles like the start-up and loading conditions. The second method, vector control (FOC & DTC) is the most common method of speed control method for AC drives due to their dynamic response [5]. Comparison between FOC and DTC are based on various criteria including basic control characteristics, dynamic performance, and implementation complexity. The simulation and evaluation of both control strategies are performed using actual parameters of Permanent Magnet Synchronous Motor fed by an IGBT PWM inverter [6]. It presents a method of estimating simultaneously the motor speed and the rotor resistance of an induction motor by superimposing ac components on the field current command. The validity of the proposed method is verified by simulation and experimentation [7].

The structure and the control methods of PMSM are analyzed and simulation is realized using conventional direct torque control (DTC) method. It can be applied for PMSM and is reliable in a wide speed range applications [8]. Dynamic permanent magnet Flux Estimation of Permanent Magnet Synchronous Machines explains clearly about the rotor flux estimation in permanent magnet synchronous motor [9]. A Direct Torque



Controlled Interior Permanent Magnet Synchronous Motor Drive without a Speed Sensor has been presented with a speed control system for an IPM motor with an inner DTC which does not require a mechanical position sensor [10].

The problem of efficiency optimization in vector-controlled interior permanent magnet synchronous motor is investigated. It also describes a method for minimizing the losses in vector controlled interior permanent magnet synchronous motor drives [11]. A new control scheme for wide speed range operation of interior permanent magnet synchronous motor drives, where both torque and stator flux linkage are directly controlled is proposed in [12]. It is proved that the dynamic performance of permanent magnet synchronous motor with vector control is better [13]. But the main advantage of DTC is that there is no requirement for transformation, and current regulator, but it gives high torque ripples [14]. The basic principle of DTC is to directly select stator voltage vectors according to difference between the actual & reference torque and stator flux linkages. In this paper along with stator resistance estimator is used [15]. In the DTC torque and flux ripples are high; to overcome this problem fuzzy controller is used. Using hysteresis band the torque ripples are reduced and MRAS technique is used for estimate the motor speed [16]. To trace the error between reference and actual values, the conventional controller PI, PID is implemented. To have better performance and accuracy in outputs, Model Reference Adaptive Control system MRAS is adapted [17]. The performance of the PMSM can further improved by implementing SVM control strategy along with DTC and Multi Level Inverters using Fuzzy Logic Controllers [18][19][20][21][22]. The hardware implementation of PMSM with PI Controller using FPGA is discussed in [23] using two level inverter with SVM control.

In this paper, Sensor less Control of PMSM with FOC using MRAS is implemented. The rotor speed is estimated using MRAS with PI controller. The paper is organized as follows: Section II revolves around the Field Oriented Control of Permanent Magnet Synchronous Motor. Section III explains the implementation of FOC for PMSM drive with the proposed MRAS. Section IV focuses on the simulation results for the dynamic performance of PMSM. Section V summarises the conclusions drawn from the work with future recommendations.

## 2. Field Oriented Control of Permanent Magnet Synchronous Motor

The principle idea of FOC is to introduce decoupling between field and torque producing component. This makes PMSM to behave like a separately excited DC motor. If the magnets are placed inside the rotor then  $L_q > L_d$ , otherwise if the magnets are placed on the surface of a rotor then  $L_q = L_d$ .

The modeling of PMSM motor in rotor reference frame is given from Eqns (1) to (8). The proposed block diagram of the work is given in Figure 1.

$$V_{qs} = R_s i_{qs} + P \lambda_{qs} + \omega_r \lambda_{ds} \quad (1)$$

$$V_{ds} = R_s i_{ds} + P \lambda_{ds} - \omega_r \lambda_{qs} \quad (2)$$

$$\lambda_{ds} = L_{ds} i_{ds} + \lambda_f \quad (3)$$

$$\lambda_{qs} = L_{qs} i_{qs} \quad (4)$$

$$v_{ds} = R_s i_{ds} + L_{ds} \frac{d}{dt} i_{ds} - L_{qs} \omega_r i_{qs} \quad (5)$$

$$v_{qs} = R_s i_{qs} + L_{qs} \frac{d}{dt} i_{qs} + L_{qs} \omega_r i_{ds} + \omega_r \lambda_f \quad (6)$$

$$T_e = \frac{3}{2} p [(L_{ds} - L_{qs}) i_{ds} i_{qs} + \lambda_f i_{qs}] \quad (7)$$

$$J \frac{d\omega_m}{dt} + B\omega_m + T_L = T_e \quad (8)$$

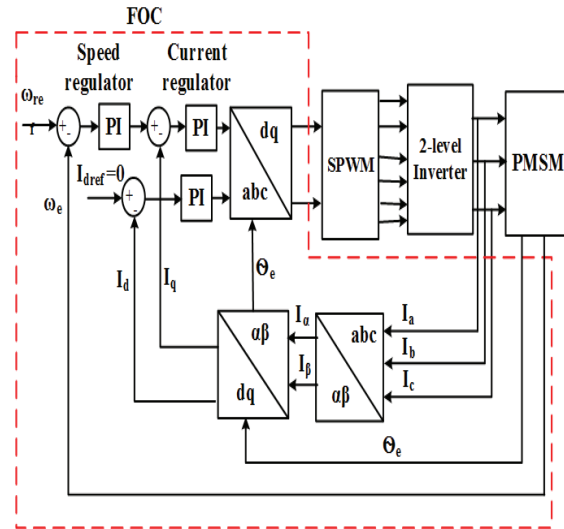


Figure 1. Block diagram of FOC of PMSM

## 3. Implementation of FOC for PMSM drive with the proposed MRAS using PI Controller

The Field Oriented Controlled electrical drives have rapid expansion in recent years. due to the achievements obtained in semiconductors for both power and signal electronics. This paper proposes to describe Field oriented control (FOC) of Permanent Magnet Synchronous motor (PMSM) using MRAS speed observer for sensor less control of drive.

This paper proposes a sensor less speed control based on MRAS, which is based on the comparison between outputs of two estimators. This estimated error is used to drive PMSM with a suitable adaptive mechanism to estimate the error speed. In this work MRAS is based on  $i_d$ ,  $i_q$  of a PMSM, since FOC is used as a speed controller.

The general block diagram of MRAS is given in Figure 2.



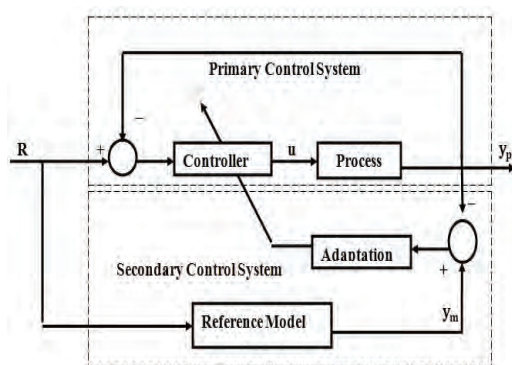


Figure 2. Block Diagram of MRAS

The main objective of MRAS is to estimate the rotor speed. Hence first  $i_d$ ,  $i_q$  are represented in a state variable form is given by Eqn (9)

$$\mathbf{p} \begin{bmatrix} i_d \\ i_q \end{bmatrix} = \begin{bmatrix} -\frac{R_s}{L_d} & \omega_e \frac{L_q}{L_d} \\ -\omega_e \frac{L_d}{L_q} & -\frac{R_s}{L_q} \end{bmatrix} \begin{bmatrix} i_d \\ i_q \end{bmatrix} + \begin{bmatrix} \frac{v_d}{L_d} \\ \frac{v_q}{L_q} - \omega_e \frac{\lambda_f}{L_q} \end{bmatrix} \quad (9)$$

According to Eqn (9), the following Eqn (10) is derived

$$\mathbf{p} \begin{bmatrix} i_d + \frac{\lambda_f}{L_d} \\ i_q \end{bmatrix} = \begin{bmatrix} -\frac{R_s}{L_d} & \omega_e \frac{L_q}{L_d} \\ -\omega_e \frac{L_d}{L_q} & -\frac{R_s}{L_q} \end{bmatrix} \begin{bmatrix} i_d + \frac{\lambda_f}{L_d} \\ i_q \end{bmatrix} + \begin{bmatrix} \frac{v_d}{L_d} + \frac{R_s}{L_d^2} \lambda_f \\ \frac{v_q}{L_q} \end{bmatrix} \quad (10)$$

From Eqn (10) the reference currents and voltages are obtained as given in Eqn (11)

$$i_d^* = i_d + \frac{\lambda_f}{L_d}, i_q^* = i_q, v_d^* = v_d + \frac{R_s}{L_d} \lambda_f, v_q^* = v_q \quad (11)$$

Using Eqn (11), Eqn (10) can be converted to Eqn (12)

$$\mathbf{p} \begin{bmatrix} \mathbf{i}_d^* \\ \mathbf{i}_q^* \end{bmatrix} = \begin{bmatrix} -\frac{R_s}{L_d} & \omega_e \frac{L_q}{L_d} \\ -\omega_e \frac{L_d}{L_q} & -\frac{R_s}{L_q} \end{bmatrix} \begin{bmatrix} \mathbf{i}_d^* \\ \mathbf{i}_q^* \end{bmatrix} + \begin{bmatrix} \frac{1}{L_d} \mathbf{v}_d^* \\ \frac{1}{L_q} \mathbf{v}_q^* \end{bmatrix} \quad (12)$$

According to Eqn (12), the state equation of adjustable model of PMSM with speed angle as the adjustable parameter is represented in Eqn(13):

$$\mathbf{p} \begin{bmatrix} \widehat{l_d^*} \\ \widehat{l_q^*} \end{bmatrix} = \begin{bmatrix} -\frac{R_s}{L_s} & \widehat{\omega_e} \\ -\widehat{\omega_e} & -\frac{R_s}{L_s} \end{bmatrix} \begin{bmatrix} \widehat{l_d^*} \\ \widehat{l_q^*} \end{bmatrix} + \frac{1}{L_s} \begin{bmatrix} \widehat{v_d^*} \\ \widehat{v_q^*} \end{bmatrix} \quad (13)$$

For SPM,  $L_d=L_q=L_s$ , so the adaptive speed mechanism can be simplified as follow:

$$\widehat{\omega}_e = \left( K_P + \frac{K_i}{p} \right) \left[ i_d \widehat{1}_q - i_q \widehat{1}_d - \frac{\lambda_f}{L_s} (i_q - \widehat{1}_q) \right] + \widehat{\omega}_e(0) \quad (14)$$

Block Diagram of FOC of PMSM with MRAS is given in Figure 3.

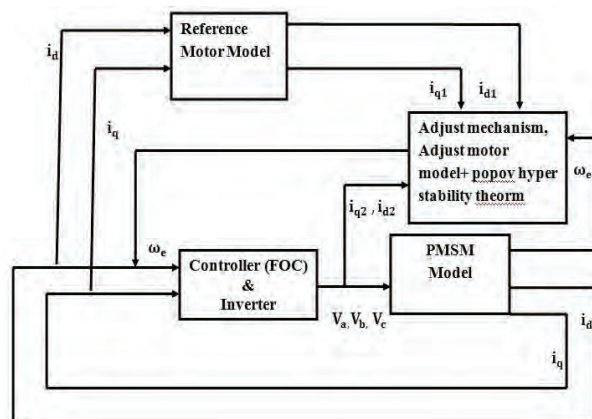


Figure 3. Block Diagram of FOC of PMSM with MRAS

#### 4. Design of PI Controller - Conventional Controller

For process control in industrial automation the conventional PI controllers are extensively used because of its simple process, design, maintenance, economical, effectiveness, less number of parameter tuning and good performance for different operating conditions. Also it does not require the complete knowledge of the system. Hence these controllers are mostly preferred in industrial applications. [24] [25] [26]. The integral term in a PI controller causes the steady-state error to reduce to zero.

Speed controller plays an significant role in achieving aspiring dynamic characteristics of AC drives (PMSM). In this work, PI controller is considered in speed control loop [27] to investigate the dynamic response of a drive for different set speeds and load conditions. This is achievable by tuning the parameters of a PI controller,  $K_p$  and  $K_i$  [25].

The stability of a IPM and SPM drive system are analyzed as a linearized error model using PI controller. The general block diagram of the PI speed controller is shown in Figure 4..

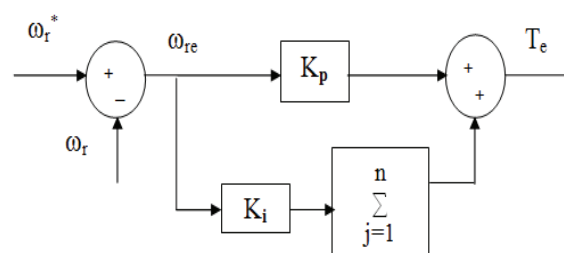


Figure 4 Block diagram of PI speed controller

The output of a speed controller (torque command) at  $n$ -th instant is expressed as follows:

$$T_{e(n)} = T_{e(n-1)} + K_p \omega_{re(n)} + K_i \omega_{re(n)} \quad (15)$$

Where  $T_{e(n)}$  is the torque output of the controller at the  $n$ -th instant,  $K_p$  is the proportional gain constants and  $K_i$  is the integral gain constant. A limit of the torque command is imposed as



$$T_{e(n+1)} = \left\{ \begin{array}{l} T_{e_{max}}, T_{e(n+1)} \geq T_{e_{max}} \\ -T_{e_{max}}, T_{e(n+1)} \leq -T_{e_{max}} \end{array} \right\} \quad (16)$$

The gains of PI controller shown here are selected by trial and error method,

## 5. Results and Discussion

The dynamic performance of the PMSM drive is tested for three different cases as mentioned below:

- Balanced Three Phase Supply
- FOC
- MRAS

### i. Balanced Three Phase Supply

At first, the motor starts on no-load, after reaching to its rated speed of 1500rpm, a load torque of  $T_L = 2\text{Nm}$  is applied at  $t=0.1\text{sec}$ .

In the first case, the dynamic performance of PMSM Drive under balanced three phase supply is modelled in MATLAB/ Simulink/ Sim Power System environment. Response of Stator currents, speed, torque, direct current, quadrature current and flux waveforms with three phase balance supply are plotted in Figure 5. In this case, there are lot of disturbances found in reaching steady state for speed and torque responses during starting. Whereas torque response has disturbance or lot of fluctuations when load is applied at  $t=0.1\text{ sec}$ . Response of torque and flux ripple waveforms with three phase balance supply are given in Figure 6. Since the input to the motor is a three phase balanced supply, it is observed that smooth response for torque and flux ripple waveforms as compared to the other two cases.

### ii. FOC

In the second case, the dynamic performance of PMSM Drive with FOC is modeled. Response of Stator currents, speed, torque, direct current, quadrature current and flux waveforms for rated speed are plotted in Figure 7.

In this case, there are few disturbances found in reaching steady state for speed and torque responses during starting as compared to the first case. Here the load torque  $T_L = 2\text{Nm}$  at  $t=0.1\text{sec}$ ;  $T_L = 1.5\text{Nm}$  at  $t=0.4\text{sec}$  and  $T_L = 1\text{Nm}$  at  $t=0.5\text{sec}$  is applied and the dynamic performance of the drive is tested with rated constant speed 1500 rpm. Responses of torque and flux ripple waveforms with FOC for rated speed are given in Figure 8.

Also the drive performance is tested considering constant rated load torque of  $T_L = 2\text{Nm}$  is applied at  $t=0\text{sec}$  with varying speed from rated speed; 1500 rpm at  $t=0\text{ sec}$ ; 1000rpm at  $t=0.1\text{sec}$  and 500 rpm at  $t=0.4\text{sec}$ . Response of Stator currents, speed, torque, direct current, quadrature current and flux waveforms for rated load torque are plotted in Figure 9. Responses of torque and flux ripple waveforms with FOC for rated load torque are given in Figure 10. The torque and flux ripples are quite high as compared to the first case.

### iii. MRAS

The same analysis is repeated for third case, the dynamic performance of PMSM Drive with MRAS is modelled. Response of Stator currents, speed, torque, direct current, quadrature current and flux waveforms for rated speed with MRAS are plotted in Figure 11. Responses of torque and flux ripple waveforms with MRAS for rated speed are given in Figure 12. Response of Stator currents, speed, torque, direct current, quadrature current and flux waveforms for rated load torque with MRAS are plotted in Figure 13. Responses of torque and flux ripple waveforms with FOC for rated load torque with MRAS are given in Figure 14.

It is found that the drive performance is better in terms of speed and torque wave forms and also the torque and flux ripples are quite low as compared to the FOC. The parameters used for PMSM is given in Table1.

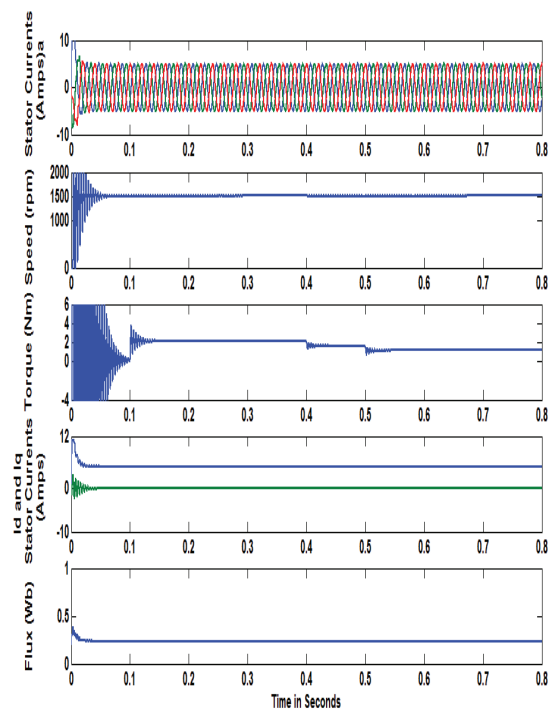


Figure 5. Response of Stator currents, speed, torque, direct current, quadrature current and flux waveforms with three phase balance supply

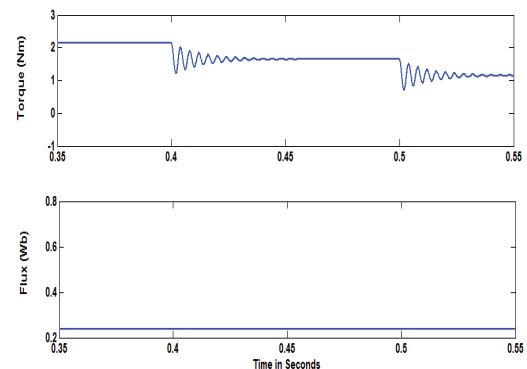


Figure 6. Response of torque and flux ripple waveforms with three phase balance supply



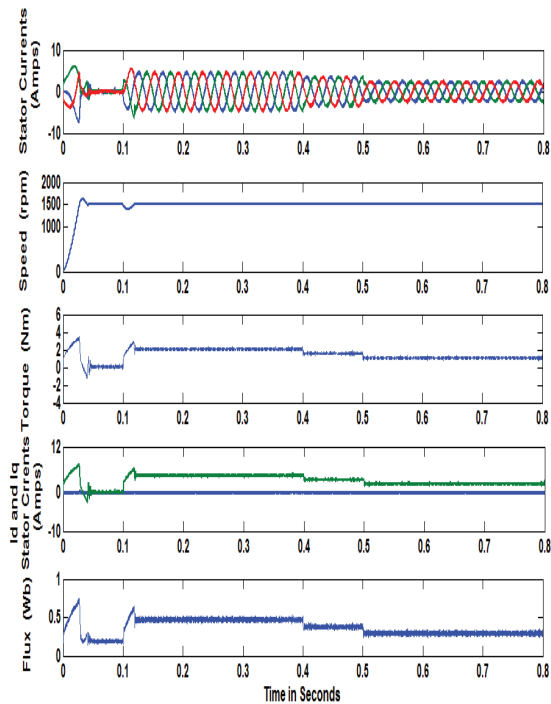


Figure 7. Response of Stator currents, speed, torque, direct current, quadrature current and flux waveforms with FOC for rated speed 1500 rpm

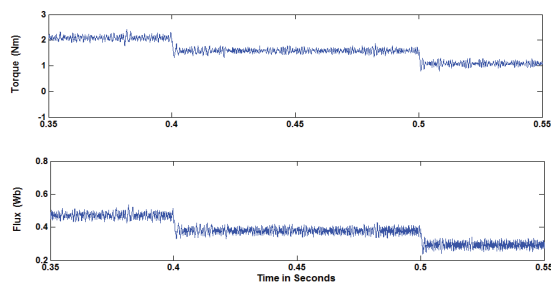


Figure 8. Responses of torque and flux ripple waveforms with FOC for rated speed .

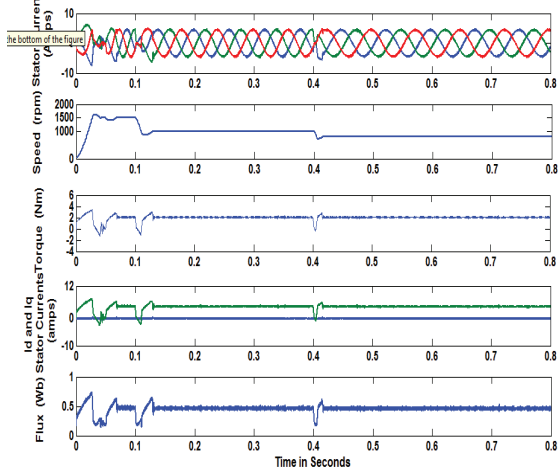


Figure 9. Response of Stator currents, speed, torque, direct current, quadrature current and flux waveforms with FOC for rated load torque 2 Nm

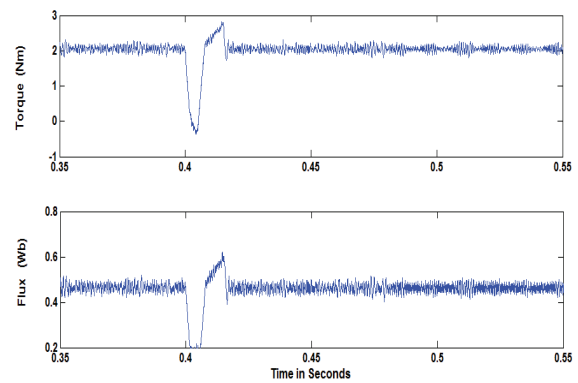


Figure 10. Responses of torque and flux ripple waveforms with FOC for rated load torque

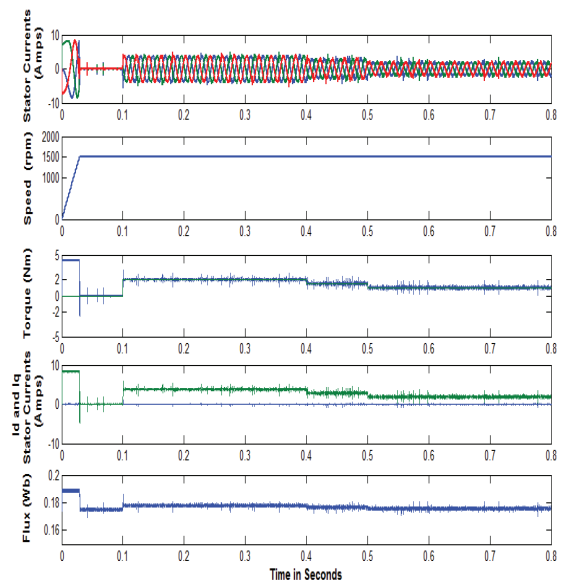


Figure 11. Response of Stator currents, speed, torque, direct current, quadrature current and flux waveforms with MRAS for rated speed 1500 rpm

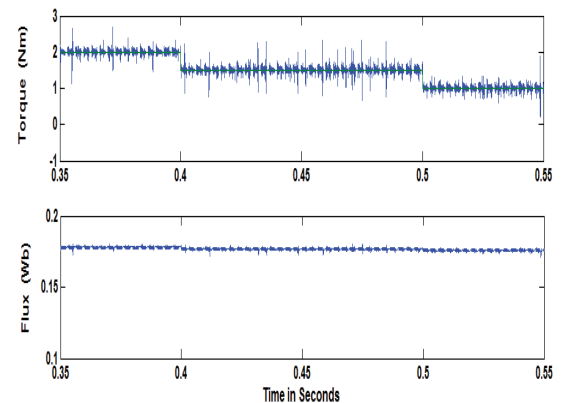


Figure 12. Figure 7. Responses of torque and flux ripple waveforms with FOC for rated speed .





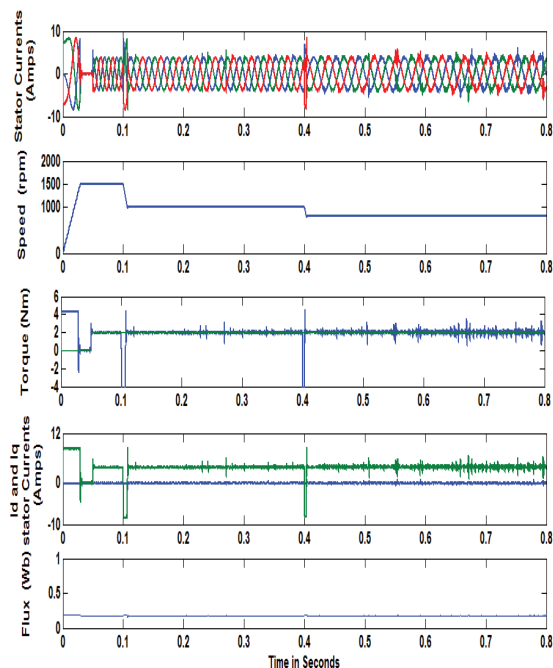


Figure 13. Response of Stator currents, speed, torque, direct current, quadrature current and flux waveforms with MRAS for rated load torque 2 Nm

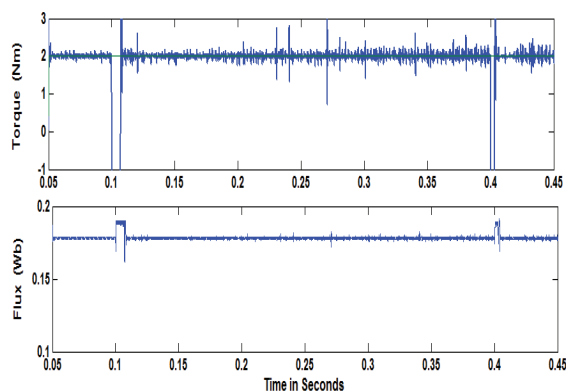


Figure 14. Responses of torque and flux ripple waveforms with MRAS for rated load torque

Table 1: Parameters of PMSM

Parameter Description	Value
DC Voltage ( $V_{dc}$ )	230 V
Direct Axis Inductance ( $L_d$ )	0.075 H
Quadrature Axis Inductance ( $L_q$ )	0.095 H
Rotor Flux Constant ( $\lambda_f$ )	0.1540 Wb
Stator Resistance ( $R_s$ )	18 $\Omega$
Number of Poles ( $p$ )	4
Moment of Inertia ( $J$ )	0.8111e-3 Kg m <sup>2</sup>
Viscous Friction Co-efficient ( $B$ )	0.0011 Nm/rad/s
Speed ( $N$ )	1500 rpm

## 6. Conclusion

Sensor less Control of PMSM with FOC using MRAS for speed estimation is carried out using MATLAB/Simulink/Sim Power Systems is carried out in this paper. The output of the adaptation mechanism is the estimated speed quantity, which is used for the tuning in adjustable model and also for feedback. The stability of such closed loop estimator is achieved through Popov's Hyper stability criterion. The method is simple and requires less computation. The drive is tested for three cases and also for dynamic conditions. It is found that with MRAS with PI Controller, the drive performance is smooth and torque and flux ripples are less. Further this work can be extended with Fuzzy Logic Controller along Multilevel Inverter topology. It is further suggested that the proposed work further can be implemented with MRAS using fuzzy logic and FPGA Hardware implementation.

## 7. References

- [1]. Pragasen Pillay, Ramu Krishnan, "Application Characteristics of Permanent Magnet Synchronous and Brushless dc Motors for Servo Drives", IEEE transactions on industry applications, vol.no. 27, Issue. no. 5, September/October 1991, Pp nos: 986-996
- [2]. L.Zhong and M.F.Rahman, "Analysis of Direct Torque Control in Permanent Magnet Synchronous Motor Drives", IEEE transactions on power electronics, vol. 12, no. 3, may 1997, Pp nos: 528-536
- [3]. Kayhan Gulez, Ali Ahmed Adam, "Adaptive Neural Network Based Controller for Direct Torque Control of PMSM with Minimum Torque Ripples", SICE Annual Conference September 2007, Kagawa university, Japan
- [4]. M. S. Merzoug, and F. Naceri, "Comparison of Field-Oriented Control and Direct Torque Control for Permanent Magnet Synchronous Motor (PMSM)", International Journal of Electrical, Computer, Energetic, Electronic and Communication Engineering Vol:2, No:9, 2008, Pp nos:1797-1802
- [5]. Shihua, "Adaptive Speed Control for Permanent-Magnet Synchronous Motor System With Variations of Load Inertia", IEEE transactions on industrial electronics, vol. 56, no. 8, august 2009, Pp nos:3050-3059
- [6]. Marek Stulrajter, Valeria Hrabovcova and Marek Franko "Permanent Magnet Synchronous Motor Control Theory," Journal of electrical engineering, vol. 58, no. 2, 2007, 79–84.
- [7]. Ch. Uma maheswara rao, Bala Murali Krishna .V, A. Laxmi Soundarya, N. Krishna Kumari "Field Oriented Control (FOC) of PMSM with Model Reference Adaptive Control Using Fuzzy – PI Controller," IJCTA Vol.8, No.1, Jan-June 2015, Pp.95-107.
- [8]. Hisao Kubota, and Kouki Matsuse, "Speed Sensor less Field-Oriented Control Induction Motor with Rotor Resistance Adaptation", IEEE



- transactions on industry applications, vol. 30, no. 5, September / October 1994.
- [9] Selin Ozcira, Nur Bekiroglu and Engin Aycicek "Simulation of Direct Torque Controlled Permanent Magnet Synchronous Motor Drive explains about the structure and the control methods of PMSM.
  - [10] Xi Xiao, Changming chen and Meng Zhang "Dynamic permanent magnet Flux Estimation of Permanent Magnet Synchronous Machines," IEEE Transactions On Applied Superconductivity, Vol. 20, No. 3, June 2010.
  - [11] Muhammed Fazlur Rahman, L. Zhong, Md. Enamul Haque and M. A. Rahman "A Direct Torque Controlled Interior Permanent Magnet Synchronous Motor Drive without a Speed Sensor," IEEE Transactions On Energy Conversion, Vol. 18, No. 1, March 2003.
  - [12] Christos Mademlis, Iordanis Kioskeridis and Nikos Margaritis "Optimal Efficiency Control Strategy for Interior Permanent Magnet Synchronous Motor Drive," IEEE Transactions On Energy Conversion, Vol. 19, No. 4, December 2004.
  - [13] Muhammed Fazlur Rahman, L. Zhong and Khiang Wee Lim "A Direct Torque Controlled Interior Permanent Magnet Synchronous Motor Drive Incorporating Field Weakening," IEEE Transactions On Industry Applications, Vol. 34, No. 6, November/December 1998.
  - [14] Zhanghui Zhang and Jiao Shu "Matlab-based Permanent Magnet Synchronous Motor Vector Control Simulation," IEEE 2010.
  - [15] Fatiha Zidani, Rachid Nait Said, "Direct torque control of induction motor with fuzzy minimization torque ripple", Journal of electrical engineering, vol. 56, no. 7-8, Pp nos: 183–188, ISSN 1335-3632 c 2005 FEI STU
  - [16] Kiran Bobby, Prof.Acy M Kottalil, N.P.Ananthamoorthy, " Simulation of PMSM Vector Control System with Fuzzy Self-Adjusting PID Controller Using MATLAB ", International Journal of Scientific and Research Publications, Volume 3, Issue 3, March 2013 1 ISSN 2250-3153, Pp nos:1-3
  - [17] Priyank Jain and Dr. M.J. Nigam, "Design of a Model Reference Adaptive Controller Using Modified MIT Rule for a Second Order System", Advance in Electronic and Electric Engineering. ISSN 2231-1297, Volume 3, Number 4 (2013), pp nos:477-484 © Research India Publications.
  - [18] U.Harika, N.KrishnaKumariz, "Multilevel Inverter fed Permanent Synchronous Motor with Field Oriented Control Using Three Level Space Vector Modulation", ICGST-ACSE Journal, ISSN: 1687-4811, Volume 15, Issue 2, ICGST LLC, Delaware, USA, December 2015, pp No: 17-23
  - [19] P. Satish Kumar, J.Amarnath, S.V.L. Narasimham "A Qualitative Space Vector PWM Algorithm for a Five-level Neutral Point Clamped Inverter", ICGST-ACSE Journal, ISSN 1687-4811, Volume 9, Issue I, January 2009
  - [20] G. Sambasiva Rao, K. Chandra Sekhar, "A Sophisticated Space Vector Pulse Width Modulation Signal Generation for Nine-Level Inverter System for Dual-Fed Induction motor Drive", ICGST-ACSE Journal, Volume 12, Issue-2, October 2012
  - [21] V. Anantha Lakshmi, T. Brahmananda Reddy, V. C. Verra Reddy, M. Surya Kalavathi, "Reduction of common Mode Voltage using Space Vector Base PWM Technique for Induction Motor Drive", ICGST-ACSE Journal, Volume 11, Issue 2, November 2011.
  - [22] N. Krishna Kumari, G. Tulasi Ram Das, and M.P.Soni, "Online Stator Reference Flux Approach to Torque Ripple Minimization for SPM Drive using Fuzzy and PI Controllers", ICGST-ACSE Journal, ISSN: 1687-4811, Volume 15, Issue 1, Delaware, USA, June 2015 pp-Nos: 31-38
  - [23] N. Krishna Kumari, G. Tulasi Ram Das, and M.P.Soni, "Implementation of FPGA on SPM Drive Using PI Controller", ICGST-ACSE Journal, ISSN: 1687-4811, Volume 15, Issue 2, ICGST LLC, Delaware, USA, December 2015 pp Nos: 37-46
  - [24] Afshan Ilyas, Shagufta Jahan, Mohammad Ayyub, "Tuning Of Conventional Pid And Fuzzy Logic Controller Using Different Defuzzification Techniques", International Journal Of Scientific & Technology Research Volume 2, Issue 1, January 2013 , pp No:138-142.
  - [25] M.Antony Freeda Rani, 2B.Sankaragomathi, "Tuning of Conventional PI controller and Fuzzy Logic Controller with Permanent Magnet Brushless DC Motor Drive ", Journal of Convergence Information Technology (JCIT) Volume 10, Number 2, March 2015, pp No: 115-124.
  - [26] K. Ayyar, K. Ramesh , G. Gurusamy, "Design of Speed Controller for Permanent Magnet Synchronous Motor Drive Using Genetic Algorithm Based Lower Order System Modelling", Journal of Computer Science 8 (10), 2012, pp No: 1700-1710
  - [27] Bin Wang, Yue Wang and Zhaoan Wang, " A Modified Direct Torque Control of Surface Permanent Magnet Synchronous Motor Drives without a Speed Sensor" IPEMC2009 pp no 1871- 1874.



## Biographies



**G. Swapna**, She received B.Tech degree from Mina Institute of Engineering and Technology for Women, Miryalaguda, affiliated to JNTU Hyderabad, Telangana in the year 2013. Pursuing M.Tech in Power Electronics in VNR Vignana Jyothi Institute of Engineering and Technology, Hyderabad.



**N. Krishna Kumari** graduated in Electrical and Electronics Engineering from Sri Venkateswara University, Tirupathi, Andhra Pradesh, India in 1994. Received M.E in Electrical machines from PSG College of Technology, Coimbatore, Bharathiyar University, Tamilnadu, India in 1997. She submitted her Ph.D thesis in the area of Electrical Drives and Control at Jawaharlal Nehru Technological University, Hyderabad in July 2016, India. She has presented/ published 20 research papers in national and international conferences and journals. Her research areas include PWM techniques, DC-DC converters, Multi Level Inverters, AC- AC converters and control of electrical drives. She has executed UGC Minor Project on "FPGA Implementation of Field Oriented Control for Permanent Magnet Synchronous Motor", in September, 2014. She is a IEEE Member, Life Member of ISTE and SAE. She is presently working as Associate Professor in the Electrical and Electronics Engineering Department, VNR Vignana Jyothi Institute of Engineering and Technology, Hyderabad, India.



**D. Ravi Kumar** graduated in Electrical and Electronics Engineering from Jawaharlal Nehru Technological University Hyderabad, Andhra Pradesh, India in 2006. He received M.Tech in Electrical Power Systems from, JNTU Hyderabad in 2008. He submitted his Ph.D thesis in the area of Electrical Distribution Systems at JNTU Anantapur in Feb. 2016, India He has published/ presented 13 research papers in International and National Journals and Conferences. His Patent titled "A Passive filter configuration to reduce THD produced by Non-Linear loads" is published in Patent office Journal, Issue No: 51/2012. He has presented a paper in IEEE International Conference ICBEST-2015 at CREATE, Singapore. He has executed UGC Minor Research Project on "Development of Optimization Techniques for Protective Devices and Distributed Generators allocation to Optimize Reliability and to reduce losses in Electrical Power Distribution systems". His research areas include Power System Reliability, Reliability Optimization, Distribution Systems, and Deregulation. He is a IEEE Member and Life Member of ISTE. He is presently working as Assistant Professor in the Electrical and Electronics Engineering Department, VNR Vignana Jyothi Institute of Engineering and Technology, Hyderabad, India.







## Solution of an Optimal Control Problem with Vector Control using Relaxation Method

Demim Fethi <sup>1</sup>, Louadj Kahina <sup>2</sup>, Aidene Mohamed <sup>3</sup>, Abdelkrim Nemra<sup>1</sup>

<sup>1</sup>*Laboratoire Robotique et Productique, Ecole Militaire Polytechnique, EMP, BP: 17, Bordj El Bahri, 16111. Algiers, Algeria.*

<sup>2</sup> *University Bouira, Faculty of sciences and applied sciences, Departement of Mathematics, Bouira, Algeria.*

<sup>3</sup>*Laboratoire de Conception et Conduites Systèmes de Production (L2CSP).Tizi-Ouzou, Algeria.*  
demifethi@gmail.com, louadj\_kahina@yahoo.fr , aidene@mail.ummto.dz, karim\_nemra@yahoo.fr

### Abstract

An optimal control problem with a linear state equation and vector control with the minimization of a quadratic criterion is considered. Furthermore, the terminal state is fixed with fixed horizon. The relaxation method is proposed coupled with the shooting technique to solve this problem. We rely on shooting method to find initial condition of adjoint vector  $p(0)$ . The convergence of the numerical procedure is presented where numerical experiments are also presented. We solve the problem analytically then we compare the results.

**Keywords:** *Optimal control, Shooting method, Relaxation method.*

## 1 Introduction

The theory of optimal control has been well developed for over forty years. With the advances of computer technique, optimal control is now widely used in multi-disciplinary applications such as biological systems, communication networks and socio-economic systems etc. As a result, more and more people will benefit greatly by learning to solve the optimal control problems numerically. Realizing such growing needs, books on optimal control put more weight on numerical methods. In retrospect, [11] was the first and the "classic" book for studying the theory as well as many interesting cases (time-optimal, fuel-optimal and linear quadratic regulator(LQR) problems). Necessary conditions for various systems were derived and explicit solutions were given when possible.

In this work, we are interested in linear quadratic optimal control problems with a fixed terminal time. Moreover the state is subject to some constraints and a value of the final state is fixed and vector control. In order to use a numerical solution, we rewrite the equations of optimality from the Pontryagin's minimum principle. Then we obtain a system in which, the differential equation describing the state is equipped with an initial and final conditions. Note also that, the costate equation derived from the Pontryagin's principle is equipped with no initial condition or terminal one to be used algorithmically. In order to determine the initial condition of the costate we use in this study, the shooting method [5] coupled with the relaxation method (see [1] and [3]). Under suitable assumptions, we analyze the convergence of the considered iterative method.

This study is organized as follows. Section 2 defines the problem and presents the shooting method. The Section 3 is devoted to the description of the relaxation method coupled with the shooting one. The convergence of the proposed method is presented in section 4, while Section 5 contains the results of the numerical experiments.



## 2 Statement of the Problem

Let us consider the following problem:

$$\begin{cases} \text{Find } u \in \mathcal{U}_{ad} \text{ such that,} \\ J(u) \leq J(v), \forall v \in \mathcal{U}_{ad}, \end{cases}$$

Where

$$J(u) = \frac{1}{2} \int_0^T ((x - x_d)^2 + ku^2) dt;$$

$x_d$  corresponding at desired state,  $u$  is the control and  $k$  control the comparative weight given to the two components of the cost function, i.e., the values of  $k$  are chosen in order to grant more weight to precision or energy expenditure to the final state  $x_T$  fixed and minimizing the cost functional, and  $\mathcal{U}_{ad}$  is the closed convex domain.

Under the following constraints:

$$\begin{cases} \dot{x}_1 = -bx_1 + ax_2 + u_1, \\ \dot{x}_2 = ax_1 - bx_2 + u_2, \\ x(0) = x_0, \\ \kappa x(T) = g, \end{cases}$$

With  $G = (1, 2)$ ,  $\gamma = 3$ ,  $\kappa = (1, 0)$ ,  $g = 2$ ,  $T = 2$ ,  $a > 0$ ,  $b > 0$ . Otherwise, We can reformulate the problem as follows:

$$\begin{cases} \dot{x}_1 = -bx_1 + ax_2 + u_1, \\ \dot{x}_2 = ax_1 - bx_2 + u_2, \\ x(0) = x_0, \\ x_1(T) = 2, \end{cases}$$

The matrix form of the state system is written as follows:

$$\begin{pmatrix} \dot{x}_1 \\ \dot{x}_2 \end{pmatrix} = \begin{pmatrix} -b & a \\ a & -b \end{pmatrix} \begin{pmatrix} x_1 \\ x_2 \end{pmatrix} + \begin{pmatrix} 1 & 0 \\ 0 & 1 \end{pmatrix} \begin{pmatrix} u_1 \\ u_2 \end{pmatrix},$$

with

$$J(u) = \frac{1}{2} \int_0^T [(x_1 - x_{1d}, x_2 - x_{2d}) \begin{pmatrix} 1 & 0 \\ 0 & 1 \end{pmatrix} \begin{pmatrix} x_1 - x_{1d} \\ x_2 - x_{2d} \end{pmatrix} + k(u_1, u_2)^t \begin{pmatrix} u_1 \\ u_2 \end{pmatrix}] dt.$$

If we solve the previous problem by a numerical procedure, we have then to solve an algebraic-differential system. On one hand, the state equation describing the physical system is provided with an initial condition  $x_0$  and the final condition  $x_f$ . On the other hand, the second equation corresponding to the costate one is formed with no initial condition and with no terminal condition. We will therefore use the shooting method to compute the value of  $p(0)$ .

### 2.1 Shooting method

The shooting method is used to obtain the value of  $p(0)$  necessary to the solution of the problem characterized by the Pontryaguin principle. If it is possible from the condition of minimization of the Hamiltonian to express the extremal control with respect to  $(x(t), p(t))$ , then the extremal system is a differential system of the form  $\dot{z}(t) = F(t, z(t))$ , where  $z(t) = (x(t), p(t))$ . With a numerical integrator beginning from  $z_0$  we obtain:  $\tilde{z}_i^{z_0} \sim z(t_i)$ , where the  $t_i$  are the discretized time generated by the numerical integrator. Note that in  $z_0 = (x_0, p_0)$ , the value of  $x_0$  is given by the initial condition of the problem and  $p_0$  denotes the value of  $p(0)$ . Therefore, for different values of  $p_0$ , we will obtain the corresponding values of  $\tilde{z}_i^{z_0}$ . We are interested in the value of  $\tilde{z}_N^{z_0} \sim z(T)$ , at the final time, where  $N$  is such that  $T = N \cdot dt$ ,  $dt$  being the time step, and  $\tilde{z}_N^{z_0} = (\tilde{x}_N^{z_0}, \tilde{p}_N^{z_0})$ . In our case only  $\tilde{x}_N^{z_0}$  are significant. Since the numerical results only depend on  $p_0$  they are denoted in the sequel  $\tilde{x}_N^{p_0}$ . We define



the mapping  $G$  as an implicit function which gives  $p_0$  by using a numerical integrator such that we obtain  $\tilde{x}_N^{p_0} - x_T = 0$ . Let

$$G : \mathbb{R}^n \rightarrow \mathbb{R}^n \text{ such that } G(p_0) = \tilde{x}_N^{p_0} - x_T.$$

Using  $G$  we define a nonlinear implicit system of  $n$  equations with  $n$  unknowns such that:

$$G(p_0) = 0. \quad (1)$$

In order to solve (1), we will use the Newton's method. The principle of the Newton's method is described as follows: in the  $k^{th}$  step, let  $p_0^k$  be an approximation of the zero  $p_0$  of  $G$ ; therefore  $p_0$  can be written  $p_0 = p_0^k + \Delta p_0^k$  and then:

$$0 = G(p_0) = G(p_0^k + \Delta p_0^k) = G(p_0^k) + \frac{\partial G}{\partial p_0}(p_0^k) \cdot (p_0 - p_0^k) + o(p_0 - p_0^k),$$

which leads to the solution of the following linear system:

$$\frac{\partial G}{\partial p_0}(p_0^k) \cdot (p_0 - p_0^k) = -G(p_0^k),$$

where  $\frac{\partial G}{\partial p_0}(p_0^k)$  is the Jacobian matrix of the application  $p_0 \rightarrow G(p_0)$  computed when  $p_0 = p_0^k$ ; note that the mapping  $p_0 \rightarrow G(p_0)$  is not explicitly known but is known numerically. So we will use a method of numerical derivation based on the finite difference method. To avoid the computation of  $\frac{\partial G}{\partial p_0}(p_0^k)$ , it is sufficient to find an approximation of  $\frac{\partial G}{\partial p_0}(p_0^k)$ . According to [4], we have two typical finite difference approximations which are frequently used:

$$\frac{\partial G_i}{\partial p_{0j}}(p_0^k) \approx \frac{1}{h_{ij}} [G_i(p_0 + \sum_{k=1}^j h_{ik} e^k) - G_i(p_0 + \sum_{k=1}^{j-1} h_{ik} e^k)],$$

or

$$\frac{\partial G_i}{\partial p_{0j}}(p_0^k) \approx \frac{1}{h_{ij}} [G_i(p_0 + h_{ij} e^j) - G_i(p_0)],$$

where the  $h_{ij}$  are the given discretization step parameters of the  $i^{th}$  equation with respect to the  $j^{th}$  variable and  $e^k$  are the  $k^{th}$  vector of the canonical basis; note that, classically, we can always choose the values of  $h_{ij}$  equal to each other at a common value  $h$ . Let  $\Delta_{ij}(p, h)$  be a finite difference approximation, then we have:

$$\lim_{h \rightarrow 0} \Delta_{ij}(p_0, h) = \frac{\partial G_i}{\partial p_{0j}}(p_0), \quad i, j = 1, \dots, n.$$

Let

$$J(p, h) = (\Delta_{ij}(p_0, h)),$$

which is an approximation of the Jacobian matrix; then the approximate Newton's method can be written as follows:

$$p_0^{k+1} = p_0^k - J(p_0^k, h^k)^{-1} \cdot G(p_0^k), \quad k = 0, 1, \dots,$$

The problem of convergence of this iterative process is ensured by using a result of the book of Ortega and Rheinbold [4]; indeed, if the discretization step  $h_{ij}$  are small enough and tend to zero then the convergence is ensured.

### 3 Numerical Algorithm

To solve the problem, with and without constraints, we perform the coupling of the relaxation method (see [1] and [3]) with the shooting method [5], the latter method being intended to calculate  $p(0)$  necessary to solve the differential-algebraic system obtained by applying the Pontryagin minimum principle. The steps in this numerical method are summarized below:

In the unconstrained case note that  $\bar{x} \equiv x^{(r)}$ .

**Remark 1** Steps (2), (2) and (3) correspond to the relaxation method while the following steps correspond to the implementation of the shooting method.

**Definition 1** An invertible matrix  $\bar{A}$  is an  $M$ -matrix if  $\bar{A}^{-1} \geq 0$  and  $\bar{a}_{ij} \leq 0$  for  $i \neq j$ .

**Remark 2**  $M$ -matrices have many main properties, in particular the spectral radius of the associated Jacobi matrix  $J = I - \bar{D}^{-1} \cdot \bar{A}$ , where  $\bar{D}$  is the diagonal of  $\bar{A}$ , is lower than one; this property will be used in the sequel.



---

**Algorithm 1** Numerical Algorithm

---

**◇ Initial Approximation**Control  $u^0$  for  $t \in [0, T]$ , and of the costate variable  $p^0(0)$ ,◇–  $r \leftarrow 0$  (where  $r$  is the number of iteration),◇ **If**  $|u^{(r+1)} - u^{(r)}| > \epsilon$  (%where  $\epsilon$  defines the convergence threshold) **do**:- Determine the state variable  $x^{(r)}$ , by integration of the state equation:

$$\begin{cases} \frac{d\bar{x}}{dt} = A\bar{x} + Bu^{(r)}, & 0 < t \leq T, \\ \bar{x}(0) = x_0, \end{cases}$$

$$\text{and } x^{(r)} = Proj(\bar{x}),$$

where  $Proj(.)$  is the projected operator,-and find the costate variable  $p^{(r)}$  by solving:

$$\begin{cases} -\frac{dp^{(r)}}{dt} = \frac{\partial H}{\partial x^{(r)}}, \\ p^{(r)}(0), \end{cases} \quad (2)$$

where  $p^{(r)}(0)$  is computed by the shooting method,– Determine the control  $u^{(r+1)}$ :

$$u^{(r+1)} \leftarrow (u^{(r)} - \frac{1}{k} B^t p^{(r)}), \quad (3)$$

◇– Else  $|u^{(r+1)} - u^{(r)}| < \epsilon$ ,

- Determine the shooting function:

$$G(p) = x^{(r)}(T) - x_f,$$

- Solve the shooting equation by the Newton method and find the new value of  $p(0)$ :

$$p^{(r+1)}(0) \leftarrow p^{(r)}(0) + \text{correction},$$

-  $r \leftarrow r + 1$ .**§End**

---



**Proposition 1** *If the following conditions are satisfied:*

- $\bar{A}$  is an  $M$ -matrix
- $k \geq k_0 > 0$
- $p^2(0) - p^2(T) > 0$ ,

*then the algorithm for computing the numerical optimal control law, by the relaxation method coupled with the shooting method, converges whatever be the initial value of  $u^0$ .*

## 4 Numerical Experiments

The Hamiltonian of the system is given by:

$$\begin{aligned} H(x(t), p(t), u(t), t) &= \frac{1}{2}[(x_1 - x_{1d})^2 + (x_2 - x_{2d})^2 + k(u_1^2 + u_2^2)] \\ &+ (p_1(t), p_2(t)) \begin{pmatrix} -b & a \\ a & -b \end{pmatrix} \begin{pmatrix} x_1 \\ x_2 \end{pmatrix} + (p_1(t), p_2(t)) \begin{pmatrix} u_1 \\ u_2 \end{pmatrix} \\ &= \frac{1}{2}[(x_1 - x_{1d})^2 + (x_2 - x_{2d})^2 + k(u_1^2 + u_2^2)] + p_1(t)(-bx_1 + ax_2 + u_1) \\ &+ p_2(t)(ax_1 - bx_2 + u_2) + p_1(t)u_1 + p_2(t)u_2. \end{aligned}$$

On the state the optimality equations can be written as follows:

$$\left\{ \begin{array}{l} \left\{ \begin{array}{l} \frac{dx_1}{dt} = \frac{\partial H}{\partial x_1} = -bx_1 + ax_2 + u_1, \\ \frac{dx_2}{dt} = \frac{\partial H}{\partial x_2} = ax_1 - bx_2 + u_2, \\ x(0) = x_0, \end{array} \right. \\ \left\{ \begin{array}{l} -\frac{dp_1}{dt} = \frac{\partial H}{\partial x_1} = -bp_1 + ap_2 + x_1 - x_{1d}, \quad p_1(T) = \alpha_1 \\ -\frac{dp_2}{dt} = \frac{\partial H}{\partial x_2} = ap_1 - bp_2 + x_2 - x_{2d}, \quad p_2(T) = \alpha_2 \end{array} \right. \\ \frac{\partial H}{\partial u_1} = 0 = ku_1 + p_1(t). \\ \frac{\partial H}{\partial u_2} = 0 = ku_2 + p_2(t). \end{array} \right.$$

where  $\alpha_i, i = \overline{1, 2}$  is found below. Adjunct on the previous system transversality condition:  
 $\exists k_1 \neq 0$  such that:

$$\varphi(0, x_0, T, x(T), k_0, k_1) = (\psi_1(T, x(T)|k_1),$$

with

$$\psi_1(T, x(T)) = \kappa x(T) - g,$$

$$\varphi(0, x_0, T, x(T), k_1) = (\kappa x(T) - g|k_1).$$

$$p(T) = -\frac{\partial \varphi}{\partial x(T)}(0, x_0, T, x(T), k_1) = -\kappa^t k_1,$$

$$(p_1(T), p_2(T)) = -(1, 0)k_1 = (-k_1, 0).$$

After, the values of  $\alpha_i, i = \overline{1, 2}$  are defined, Hamilton-Pontriaguine equation's are written as follows:

$$\left\{ \begin{array}{l} \left\{ \begin{array}{l} \dot{x}_1 = -bx_1 + ax_2 + u_1, \\ \dot{x}_2 = ax_1 - bx_2 + u_2, \\ x(0) = x_0, \end{array} \right. \\ \left\{ \begin{array}{l} -\dot{p}_1 = -bp_1 + ap_2 + x_1 - x_{1d}, \quad p_1(T) = -k_1 \\ -\dot{p}_2 = ap_1 - bp_2 + x_2 - x_{2d}, \quad p_2(T) = 0 \end{array} \right. \\ 0 = ku_1 + p_1(t) \\ 0 = ku_2 + p_2(t) \end{array} \right.$$



Then, the matrix form is given as follows:

$$\begin{pmatrix} \dot{x}_1 \\ \dot{x}_2 \\ -\dot{p}_1 \\ -\dot{p}_2 \\ 0 \\ 0 \\ p_1(T) \end{pmatrix} = \begin{pmatrix} -b & a & 0 & 0 & 0 & 0 & 0 \\ a & -b & 0 & 0 & 1 & 0 & 0 \\ -1 & 0 & -b & a & 0 & 0 & 0 \\ 0 & -1 & a & -b & 0 & 0 & 0 \\ 0 & 0 & 1 & 0 & k & 0 & 0 \\ 0 & 0 & 0 & 1 & 0 & k & 0 \\ 0 & 0 & 0 & 0 & 0 & 0 & -1 \end{pmatrix} \begin{pmatrix} x_1 \\ x_2 \\ p_1 \\ p_2 \\ u_1 \\ u_2 \\ k_1 \end{pmatrix}$$

We solve iteratively the following problem of the fixed point:

$$\begin{cases} \dot{x}_1 = -bx_1 + ax_2 + u_1, \\ \dot{x}_2 = ax_1 - bx_2 + u_2, \\ x_1(0) = 0, x_2(0) = 0, \\ \dot{p}_1 = bp_1 - ap_2 - x_1 + x_{1d}, & p_1(T) = -k_1 \\ \dot{p}_2 = -ap_1 + bp_2 - x_2 + x_{2d}, & p_2(T) = 0, \\ u_1 = -\frac{p_1(t)}{k}, \\ u_2 = -\frac{p_2(t)}{k}, \end{cases}$$

## 5 Analytical Solution

Let us derivation method at the level equation. We obtain:

$$\dot{p}_1 = bp_1 - ap_2 - x_1 + x_{1d},$$

$$\ddot{p}_1 = b\dot{p}_1 - a\dot{p}_2 - \dot{x}_1,$$

$$\ddot{p}_1 = b(bp_1 - ap_2 - x_1 + x_{1d}) - a(-ap_1 + bp_2 - x_2 + x_{2d}) - (-bx_1 + ax_2 - \frac{p_1}{k}),$$

$$\ddot{p}_1 = b^2p_1 - abp_2 - bx_1 + bx_{1d} + a^2p_1 - abp_2 + ax_2 - ax_{2d} + bx_1 - ax_2 + \frac{p_1}{k},$$

$$\ddot{p}_1 = (a^2 + b^2 + \frac{1}{k})p_1 - 2abp_2 + bx_{1d} - ax_{2d},$$

Then,

$$\ddot{p}_1 = (a^2 + b^2 + \frac{1}{k})p_1 - 2abp_2 + bx_{1d} - ax_{2d}.$$

In the same way:

$$\dot{p}_2 = -ap_1 + bp_2 - x_2 + x_{2d}$$

$$\ddot{p}_2 = -a\dot{p}_1 + b\dot{p}_2 - \dot{x}_2,$$

$$\ddot{p}_2 = -a(bp_1 - ap_2 - x_1 + x_{1d}) + b(-ap_1 + bp_2 - x_2 + x_{2d}) - (ax_1 - bx_2 - \frac{p_2}{k}),$$

$$\ddot{p}_2 = -abp_1 + a^2p_2 + ax_1 - ax_{1d} - abp_1 + b^2p_2 - bx_2 + bx_{2d} - ax_1 + bx_2 + \frac{p_2}{k},$$

$$\ddot{p}_2 = -2abp_1 + (a^2 + b^2 + \frac{1}{k})p_2 - ax_{1d} + bx_{2d},$$



Then

$$\ddot{p}_2 = (a^2 + b^2 + \frac{1}{k})p_2 - 2abp_1 - ax_{1d} + bx_{2d} \quad (4)$$

derive double the equation (4), we obtain:

$$p_1^{(4)} = (a^2 + b^2 + \frac{1}{k})\ddot{p}_1 - 2ab\ddot{p}_2,$$

$$p_1^{(4)} = (a^2 + b^2 + \frac{1}{k})\ddot{p}_1 - 2ab(-2abp_1 + (a^2 + b^2 + \frac{1}{k})p_2 - ax_{1d} + bx_{2d}),$$

$$p_1^{(4)} = (a^2 + b^2 + \frac{1}{k})\ddot{p}_1 + 4a^2b^2p_1 - 2ab(a^2 + b^2 + \frac{1}{k})p_2 + 2a^2bx_{1d} - 2ab^2x_{2d},$$

Then,

$$p_1^{(4)} = (a^2 + b^2 + \frac{1}{k})\ddot{p}_1 + 4a^2b^2p_1 - 2ab(a^2 + b^2 + \frac{1}{k})p_2 + 2a^2bx_{1d} - 2ab^2x_{2d},$$

(4) leads:

$$2abp_2 = (a^2 + b^2)p_1 - \ddot{p}_1 + bx_{1d} - ax_{2d}, \quad (5)$$

By injecting (5) in (5), we obtain:

$$p_1^{(4)} = (a^2 + b^2 + \frac{1}{k})\ddot{p}_1 + 4a^2b^2p_1 - (a^2 + b^2 + \frac{1}{k})((a^2 + b^2 + \frac{1}{k})p_1 - \ddot{p}_1 + bx_{1d} - ax_{2d}) + 2a^2bx_{1d} - 2ab^2x_{2d},$$

$$\begin{aligned} p_1^{(4)} &= (a^2 + b^2 + \frac{1}{k})\ddot{p}_1 + 4a^2b^2p_1 - ((a^2 + b^2)^2 + \frac{1}{k}(a^2 + b^2))p_1 + (a^2 + b^2 + \frac{1}{k})\ddot{p}_1 \\ &\quad - b(a^2 + b^2 + \frac{1}{k})x_{1d} + a(a^2 + b^2 + \frac{1}{k})x_{2d} + 2a^2bx_{1d} - 2ab^2x_{2d}, \end{aligned}$$

$$\begin{aligned} p_1^{(4)} &= (2a^2 + 2b^2 + \frac{2}{k})\ddot{p}_1 - ((a^2 + b^2 + \frac{1}{k})^2 - 4a^2b^2)p_1 + (-a^2b - b^3 - \frac{b}{k} + 2a^2b)x_{1d} \\ &\quad + (a^3 + ab^2 + \frac{a}{k} - 2ab^2)x_{2d}, \end{aligned}$$

Then,

$$p_1^{(4)} - (2a^2 + 2b^2 + \frac{2}{k})\ddot{p}_1 - ((a^2 + b^2 + \frac{1}{k})^2 - 4a^2b^2)p_1 = (-b^3 - \frac{b}{k} + a^2b)x_{1d} + (a^3 - ab^2 + \frac{a}{k})x_{2d}, \quad (6)$$

The characteristic equation corresponding in equation (6) written as:

$$C^4 - 2(a^2 + b^2 + \frac{1}{k})C^2 - (-(a^2 + b^2 + \frac{1}{k})^2 + 4a^2b^2) = 0,$$

$$\Delta = 4a^2b^2$$

The root of the characteristic equation are given by:

$$C_1^2 = (a^2 + b^2 + \frac{1}{k}) - 2ab,$$

$$C_2^2 = (a^2 + b^2 + \frac{1}{k}) + 2ab.$$

Then

$$p_1(t) = \lambda e^{C_1 t} + \beta e^{-C_1 t} + \mu e^{C_2 t} + \alpha e^{-C_2 t} + \nu. \quad (7)$$



Determine  $\nu$ , we have:

$$\begin{aligned}\dot{p}_1(t) &= \lambda C_1 e^{C_1 t} - \beta C_1 e^{-C_1 t} + \mu C_2 e^{C_2 t} - \alpha C_2 e^{-C_2 t}, \\ \ddot{p}_1(t) &= \lambda C_1^2 e^{C_1 t} + \beta C_1^2 e^{-C_1 t} + \mu C_2^2 e^{C_2 t} + \alpha C_2^2 e^{-C_2 t}, \\ p_1^{(3)}(t) &= \lambda C_1^3 e^{C_1 t} - \beta C_1^3 e^{-C_1 t} + \mu C_2^3 e^{C_2 t} - \alpha C_2^3 e^{-C_2 t}, \\ p_1^{(4)}(t) &= \lambda C_1^4 e^{C_1 t} + \beta C_1^4 e^{-C_1 t} + \mu C_2^4 e^{C_2 t} + \alpha C_2^4 e^{-C_2 t}.\end{aligned}$$

We substitute on (6), and we obtain:

$$\begin{aligned}& \lambda[C_1^4 - (-(a^2 + b^2 + \frac{1}{k})^2 + 4a^2b^2) - 2(a^2 + b^2 + \frac{1}{k})C_1^2]e^{C_1 t} + \beta[C_1^4 - (-(a^2 + b^2 + \frac{1}{k})^2 + 4a^2b^2) \\ & - 2(a^2 + b^2 + \frac{1}{k})C_1^2]e^{-C_1 t} + \mu[C_2^4 - (-(a^2 + b^2 + \frac{1}{k})^2 + 4a^2b^2) - 2(a^2 + b^2 + \frac{1}{k})C_2^2]e^{C_2 t} + \alpha[C_2^4 \\ & - (-(a^2 + b^2 + \frac{1}{k})^2 + 4a^2b^2) - 2(a^2 + b^2 + \frac{1}{k})C_2^2]e^{-C_2 t} + (-(a^2 + b^2 + \frac{1}{k})^2 + 4a^2b^2)\nu \\ & = (-b^3 - \frac{b}{k} + a^2b)x_{1d} + (a^3 - ab^2 + \frac{a}{k})x_{2d},\end{aligned}$$

By identification, we obtain:

$$\nu = \frac{(-b^3 - \frac{b}{k} + a^2b)x_{1d} + (a^3 - ab^2 + \frac{a}{k})x_{2d}}{4a^2b^2 - (a^2 + b^2 + \frac{1}{k})^2}. \quad (8)$$

We deduce  $p_2(t)$  of (5), we obtain:

$$\begin{aligned}p_2(t) &= \frac{1}{2ab}[(a^2 + b^2 + \frac{1}{k})p_1 - \ddot{p}_1 + bx_{1d} - ax_{2d}2ab], \\ p_2(t) &= \frac{a^2 + b^2 + \frac{1}{k}}{2ab}[\lambda e^{C_1 t} + \beta e^{-C_1 t} + \mu e^{C_2 t} + \alpha e^{-C_2 t} + \nu] - \frac{1}{2ab}[\lambda C_1^2 e^{C_1 t} + \beta C_1^2 e^{-C_1 t} + \mu C_2^2 e^{C_2 t} \\ & + \alpha C_2^2 e^{-C_2 t}] + \frac{1}{2a}x_{1d} - \frac{1}{2b}x_{2d}, \\ p_2(t) &= \lambda[\frac{a^2 + b^2 + \frac{1}{k} - C_1^2}{2ab}]e^{C_1 t} + \beta[\frac{a^2 + b^2 + \frac{1}{k} - C_1^2}{2ab}]e^{-C_1 t} \\ & + \mu[\frac{a^2 + b^2 + \frac{1}{k} - C_2^2}{2ab}]e^{C_2 t} + \alpha[\frac{a^2 + b^2 + \frac{1}{k} - C_2^2}{2ab}]e^{-C_2 t} \\ & + (\frac{a^2 + b^2 + \frac{1}{k}}{2ab})\nu + \frac{1}{2a}x_{1d} - \frac{1}{2b}x_{2d}.\end{aligned}$$

Then,

$$p_2(t) = \lambda e^{C_1 t} + \beta e^{-C_1 t} - \mu e^{C_2 t} - \alpha e^{-C_2 t} + (\frac{a^2 + b^2 + \frac{1}{k}}{2ab})\nu + \frac{1}{2a}x_{1d} - \frac{1}{2b}x_{2d}. \quad (9)$$

Also, given the following equation:

$$\begin{aligned}x_1 &= bp_1 - ap_2 - \dot{p}_1 + x_{1d}, \\ x_2 &= -ap_1 + bp_2 - \dot{p}_2 + x_{2d}.\end{aligned}$$

We obtain the following results:

$$\begin{aligned}x_1(t) &= b[\lambda e^{C_1 t} + \beta e^{-C_1 t} + \mu e^{C_2 t} + \alpha e^{-C_2 t} + \nu] - a[\lambda e^{C_1 t} + \beta e^{-C_1 t} + \mu e^{C_2 t} + \alpha e^{-C_2 t} \\ & + \frac{a^2 + b^2 + \frac{1}{k}}{2ab}\nu + \frac{1}{2a}x_{1d} - \frac{1}{2b}x_{2d}] - [\lambda C_1 e^{C_1 t} - \beta C_1 e^{-C_1 t} + \mu C_2 e^{C_2 t} - \alpha C_2 e^{-C_2 t}] + x_{1d}\end{aligned}$$





$$x_1(t) = \lambda(b-a-C_1)e^{C_1t} + \beta(b-a+C_1)e^{-C_1t} + \mu(b+a-C_2)e^{C_2t} + \alpha(b+a+C_2)e^{-C_2t} \\ + \left[b - \frac{(a^2+b^2+\frac{1}{k})}{2b}\right]\nu - \frac{1}{2}x_{1d} + \frac{a}{2b}x_{2d} + x_{1d}.$$

Then,

$$x_1(t) = \lambda(b-a-C_1)e^{C_1t} + \beta(b-a+C_1)e^{-C_1t} + \mu(b+a-C_2)e^{C_2t} + \alpha(b+a+C_2)e^{-C_2t} + \frac{b^2-a^2-\frac{1}{k}}{2b}\nu \\ + \frac{1}{2}x_{1d} + \frac{a}{2b}x_{2d}. \quad (10)$$

$$x_2(t) = -a[\lambda e^{C_1t} + \beta e^{-C_1t} + \mu e^{C_2t} + \alpha e^{-C_2t} + \nu] + b[\lambda e^{C_1t} + \beta e^{-C_1t} + \mu e^{C_2t} + \alpha e^{-C_2t} + \\ + (b^2-a^2-\frac{1}{k})2b]\nu + \frac{1}{2}x_{1d} + \frac{a}{2b}x_{2d} - [\lambda C_1 e^{C_1t} - \beta C_1 e^{-C_1t} + \mu C_2 e^{C_2t} - \alpha C_2 e^{-C_2t}] + x_{2d},$$

Then,

$$x_2(t) = \lambda(b-a-C_1)e^{C_1t} + \beta(b-a+C_1)e^{-C_1t} + \mu(-b-a+C_2)e^{C_2t} + \alpha(-a-b-C_2)e^{-C_2t} \\ + \frac{b^2-a^2+\frac{1}{k}}{2a}\nu + \frac{b}{2a}x_{1d} + \frac{1}{2}x_{2d}. \quad (11)$$

The constants are determined by the following limits conditions:

$$x_1(0) = 0, x_2(0) = 0,$$

$$x_1(T) = 2,$$

$$p_1(T) = -k_1, p_2(T) = 0.$$

We solve the linear system numerically:

$$\left\{ \begin{array}{l} 0 = \lambda(b-a-C_1) + \beta(b-a+C_1) + \mu(b+a-C_2) + \alpha(b+a+C_2) + \frac{b^2-a^2-\frac{1}{k}}{2b}\nu + \frac{1}{2}x_{1d} + \frac{a}{2b}x_{2d}, \\ 0 = \lambda(b-a-C_1) + \beta(b-a+C_1) + \mu(-b-a+C_2) + \alpha(-b-a-C_2) + \left(\frac{b^2-a^2+\frac{1}{k}}{2a}\right)\nu + \frac{b}{2a}x_{1d} + \frac{1}{2}x_{2d}, \\ 2 = \lambda(b-a-C_1)e^{C_1T} + \beta(b-a+C_1)e^{-C_1T} + \mu(b+a-C_2)e^{C_2T} + \alpha(b+a+C_2)e^{-C_2T} + \frac{b^2-a^2-\frac{1}{k}}{2b}\nu \\ + \frac{1}{2}x_{1d} + \frac{a}{2b}x_{2d}, \\ -k_1 = \lambda e^{C_1T} + \beta e^{-C_1T} + \mu e^{C_2T} + \alpha e^{-C_2T} + \nu, \\ 0 = \lambda e^{C_1T} + \beta e^{-C_1T} - \mu e^{C_2T} - \alpha e^{-C_2T} + \left(\frac{a^2+b^2+\frac{1}{k}}{2ab}\right)\nu + \frac{1}{2a}x_{1d} - \frac{1}{2b}x_{2d} \end{array} \right. .$$

(12) is equivalent to following system:

$$\left\{ \begin{array}{l} \lambda(b-a-C_1) + \beta(b-a+C_1) + \mu(b+a-C_2) + \alpha(b+a+C_2) = -\frac{b^2-a^2-\frac{1}{k}}{2b}\nu - \frac{1}{2}x_{1d} - \frac{a}{2b}x_{2d}, \\ \lambda(b-a-C_1) + \beta(b-a+C_1) + \mu(-b-a+C_2) + \alpha(-b-a-C_2) = -\left(\frac{b^2-a^2+\frac{1}{k}}{2a}\right)\nu - \frac{b}{2a}x_{1d} - \frac{1}{2}x_{2d}, \\ \lambda(b-a-C_1)e^{C_1T} + \beta(b-a+C_1)e^{-C_1T} + \mu(b+a-C_2)e^{C_2T} + \alpha(b+a+C_2)e^{-C_2T} = 2 - \frac{b^2-a^2-\frac{1}{k}}{2b}\nu \\ - \frac{1}{2}x_{1d} - \frac{a}{2b}x_{2d}, \\ \lambda e^{C_1T} + \beta e^{-C_1T} + \mu e^{C_2T} + \alpha e^{-C_2T} + k_1 = -\nu, \\ \lambda e^{C_1T} + \beta e^{-C_1T} - \mu e^{C_2T} - \alpha e^{-C_2T} = -\left(\frac{a^2+b^2+\frac{1}{k}}{2ab}\right)\nu - \frac{1}{2a}x_{1d} + \frac{1}{2b}x_{2d} \end{array} \right. .$$



Let matrix form:

$$\begin{pmatrix} b-a-C_1 & b-a+C_1 & b+a-C_2 & b+a+C_2 & 0 \\ b-a-C_1 & b-a+C_1 & -b-a+C_2 & -b-a-C_2 & 0 \\ (b-a-C_1)e^{C_1T} & (b-a+C_1)e^{-C_1T} & (-b-a+C_2)e^{C_2T} & (-b-a-C_2)e^{-C_2T} & 0 \\ e^{C_1T} & e^{-C_1T} & e^{C_2T} & e^{-C_2T} & 1 \\ e^{C_1T} & e^{-C_1T} & -e^{C_2T} & -e^{-C_2T} & 0 \end{pmatrix} \begin{pmatrix} \lambda \\ \beta \\ \mu \\ \alpha \\ k_1 \end{pmatrix} = \begin{pmatrix} -\frac{b^2-a^2-\frac{1}{k}}{2b}\nu - \frac{1}{2}x_{1d} - \frac{a}{2b}x_{2d} \\ -(\frac{b^2-a^2+\frac{1}{k}}{2a})\nu - \frac{b}{2a}x_{1d} - \frac{1}{2}x_{2d} \\ 2 - \frac{b^2-a^2-\frac{1}{k}}{2b}\nu - \frac{1}{2}x_{1d} - \frac{a}{2b}x_{2d} \\ -\nu \\ -(\frac{a^2+b^2+\frac{1}{k}}{2ab})\nu - \frac{1}{2a}x_{1d} + \frac{1}{2b}x_{2d} \end{pmatrix}$$

### 5.0.1 Comparison of the Two Approaches

The numerical algorithm is implemented in Matlab. Particularly, we used the function *ode45* et *fsolve*. In this example, the method converge independently with initial point  $\psi(0) = (0.0536, 0.1072)$ . Numerical experience is determined by values  $a = 1$ ,  $b = 3$  et  $k = 2$ . Let us deduce that analytical solution and numerical solution correspond perfectly. For different values of  $k$ , The performance of the numerical procedure is

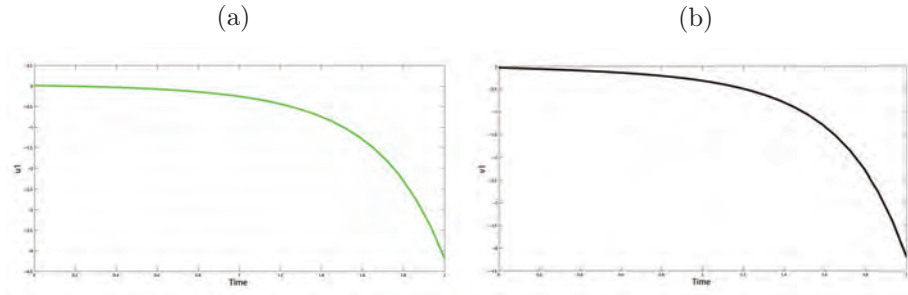


Figure 1: (a)  $u_1$  numerical solution (b)  $v_1$  true solution

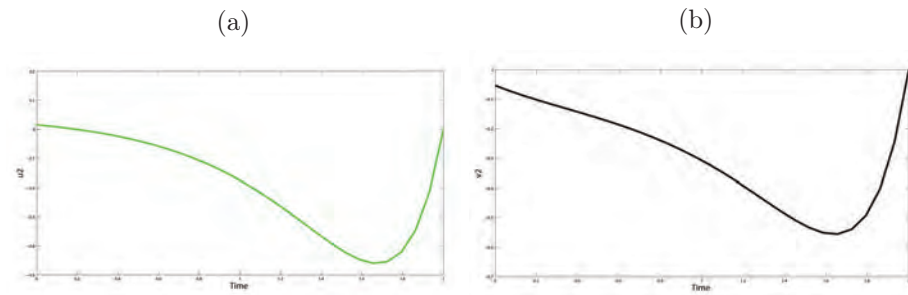


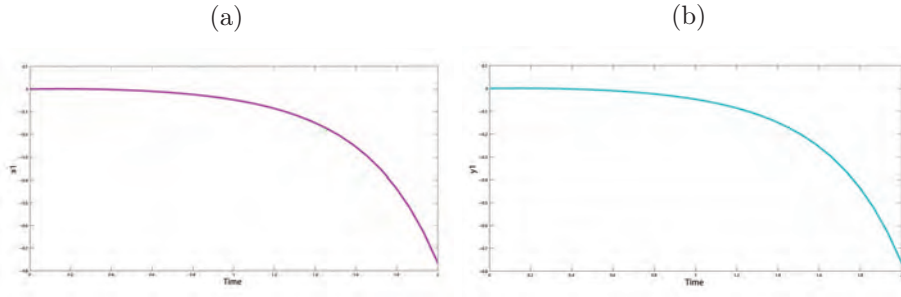
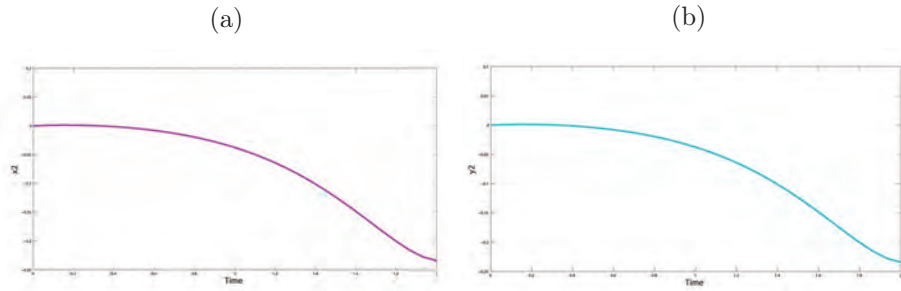
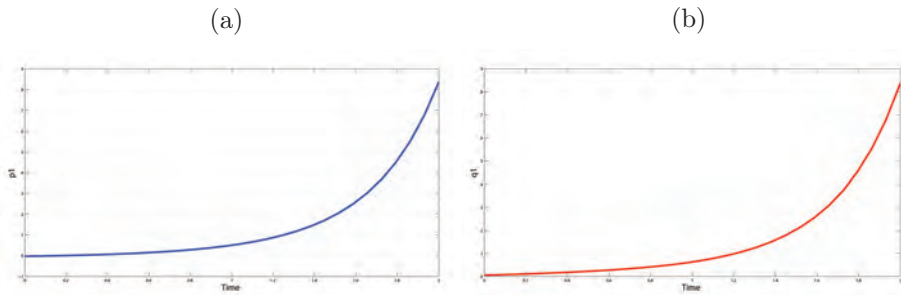
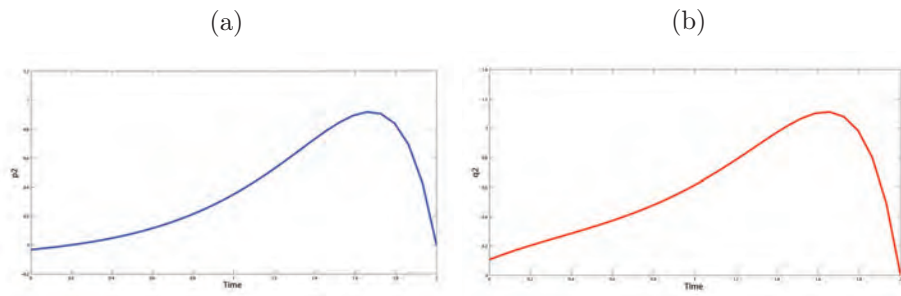
Figure 2: (a)  $u_2$  numerical solution (b)  $v_2$  true solution

summarized in the following table.

k	time C.P.U	Iteration Number
0.5	1.3089	12
1	2.3619	8
1.5	2.7016	7
2	3.7995	7
2.5	5.7479	6

Note that the algorithm converges quickly, to a very small number of iterations required to reach convergence. In addition, the computing time used is very low.



Figure 3: (a)  $x_1$  numerical solution (b)  $y_1$  true solutionFigure 4: (a)  $x_2$  numerical solution (b)  $y_2$  true solutionFigure 5: (a)  $p_1$  numerical solution (b)  $q_1$  true solutionFigure 6: (a)  $p_2$  numerical solution (b)  $q_2$  true solution

## 6 Conclusions

The goal of this study concerns the linear quadratic optimal control problems with a fixed terminal time. We have used the relaxation method coupled with the shooting method for solving the optimal control problem. The convergence of the procedure is ensured. The rate of convergence is high and the computation of time is fast. We concluded that relaxation method give a good results in quick time.



## References

- [1] Efsthathios Bakolas-Panagiotis Tsiotras, Optimal Synthesis of the Zermelo-Markov-Dubins, Problem in a constant Drift Field, J.Optimal theory applications, Springer, 156:469-492. 2013.
- [2] David G. Hull, Optimal control theory for applications, Springer-Verlag, 2003.
- [3] J.M.Ortega and W.C.Rheinboldt, Iterative solution of nonlinear equations in several variables. Academic Press, New York, 1970.
- [4] E.Trelat, Contrôle optimal: théorie et applications, Vuibert, collection Mathématiques Concrètes, 2005.
- [5] Suresh P.Sethi, Gerald L.Thompsonn Optimal control theory, applications to management science and economics, second edition, 2000.
- [6] Walid Bouhafs, Nahla Abdellatif, Frédéric Jean, Jérôme Harmand, Commande optimale en temps minimal d'un procédé biologique d'épuration de l'eau, Arima, Janvier 2013.
- [7] Alexander J. Zaslavski, Structure of approximate solutions of optimal control problems, Springer, 2013.
- [8] Leonid D. Akulenko, Problems and Methods of Optimal Control, Springer, 1994.
- [9] I. H. Mufti, Computational Methods in Optimal Control Problems, Springer, 1970.
- [10] R. Pytlak, Numerical Methods for Optimal Control Problems With State Constraints, Spinger, 1999.
- [11] M. Athans and P. Falb (2007). Optimal control: an introduction to the theory and its applications. Dover Publications, Inc.



## Biographies



**Fethi Demim** received the Engineer degree in Electronics from the University of Abou-Bekr Belkaïd, Tlemcen, Algeria, in 2002 and M.S degree in control systems from the Department of Control, Polytechnic Military School, Algeria, in 2014. He is currently pursuing his Ph.D. degree at the Department of Control, Polytechnic Military School, Algeria. His current research interests are autonomous navigation, unmanned vehicles, localization of ground vehicle and map building.



**Kahina Louadj** is currently lecturer at University of Bouira in the field of Informatics, mathematics and physics Laboratory (LIMPAF). She studied at University of Tizi Ouzou. She received DES of Mathematics in 2000, Doctorate in 2012. Her main research interests are optimal control, optimization, aircraft problems.



**Mohamed Aidene** is currently Professor at University of Tizi-Ouzou, in Laboratoire de Conception et Conduite de Systèmes de Production (L2CSP). He is Director of L2CSP, and studied at University of Minsk. He received his PHD of Mathematics in Minsk. His main research interests are optimal control, optimization, Operational research.



**Abdelkrim Nemra** received the Engineer degree and M.S degree in Control systems from the Department of Control, Polytechnic Military School, Algeria, in 2004 and 2006, respectively. He received the Ph.D. degree in Control systems from the Department of Informatics and Sensors, Cranfield University, Shrivenham, UK in 2010. He received the accreditation to supervise research (HDR) in 2016. His current research interests include unmanned vehicles, localization of aerial vehicle and map building. His publications include a number of conference and journal papers in computer vision and data fusion and book chapter in robotics.









## Comprehensive Comparison of PWM and SVM based Three Phase AC to AC Matrix Converters

Raheel Muzzammel and Umair Tahir

*Department of Electrical Engineering, University of Lahore, Lahore, Pakistan*

raheelmuzzammel@gmail.com and umairtahir099@gmail.com

### Abstract

Converters are employed in wide range of applications to save energy and attain desirable voltage. Matrix converter can convert three phase AC input to three phase AC output with variable voltage amplitude and frequency directly. It can be used as a bidirectional power flow converter without any intermediate storage element. The objective of this proposed research is to minimize the harmonic losses to get maximum output voltage ratio, sinusoidal current, desired variable voltage amplitude and desired variable frequency. Pulse width modulation and space vector modulation algorithm control the input and output voltage and frequency independently. In this research work, pulse width modulation and space vector modulation based matrix converters will be designed to attain voltage ratio up to 1 and to reduce switching losses so that total harmonic distortion could be minimized with sinusoidal waveforms of desired amplitude and frequency. Comparisons will be drawn on the basis of harmonic contents present in the desired output waveform by changing the characteristics of input waveform. Simulation environment will be created in Matlab.<sup>1</sup>

**Keywords:** *Pulse Width Modulation, Space Vector Modulation, Matrix Converters, Matlab*

### Nomenclature

PWM	Pulse Width Modulation
SVM	Space Vector Modulation
AC	Alternating Current
DC	Direct Current
BJT	Bipolar Junction Transistor
MOSFET	Metal Oxide Silicon Field Effect Transistor
IGBT	Insulated Gate Bipolar Junction Transistor

### 1 Introduction

The basic component of matrix converter is bidirectional switch which are forcibly commutated. Switches are used in controlled manner to generate a variable frequency output. There is no dc link between two different voltage sources and also there is no need of using energy storing active elements link capacitor. The switches are used in controlled way due to which the operation at high frequency is possible. There are many type of matrix converters in which the components used can be reduced according to the requirement and thus the modulation technique is also less complex [22, 9, 20, 18, 15].

Pulses of variable widths are generated using pulse width modulation that represent the amplitude of an analogue signal. The main use of pulse width modulation is that the power supplied to the electrical loads especially of rotating loads like motors which have some inertia, can be controlled. Thus, motors can be made to operate at variable speed by using pulse width modulation.

To control the pulse width modulation, another algorithm space vector pulse width modulation is employed [19]. It is used to drive a motor at variable speed by generating three phase alternating currents waveform. There are many methods and variations of space vector pulse width modulation, each having different quality and different requirement of computation. Due to rapid switching actions, the harmonics are generated. The elimination of these harmonics is one of the basic purposes of using space vector pulse width modulation [30].

Non linear loads generate current harmonics and voltage harmonics in a system. High order frequencies are major cause of problems in quality of power supplied. Harmonics result in increased heating of the equipments. It is highly desirable to reduce the harmonics in any power system. Low order harmonics which are undesirable, can be eliminated by selecting most preferable harmonics elimination technique [21, 24]. The operation of electrical system is highly

<sup>1</sup>This study has been implemented at Department of Electrical Engineering, University of Lahore, Pakistan



effected due to generation of harmonics. A lot of attention in any system is paid to the reduction of harmonics [11, 27]. The operations of a systems have standards to maintain and to limit up to which harmonics can be added to the system [1, 2, 3]. By using multiple winding transformer in multiple connection at input side of a system, current harmonics can be reduced. Harmonics can also be removed using different active and passive filter topologies [5, 28, 4].

The matrix converter topologies are more attractive after the development of power switches like bipolar junction transistors (BJTs), metal oxide silicon field effect transistors (MOSFETs) and insulated gate bipolar junction transistors (IGBTs) [12]. The first time development of matrix converter was in 1980 [31, 32]. Venturini and Alesia in 1980, presented the converter using bidirectional switches and they introduced the name of matrix converter for the first time. The modulation technique introduced by them is known as direct transfer function approach. In order to obtain the desired output voltages, the input voltages are multiplied by the modulation matrix [23] [8].

After them in 1983, Rodriguez introduced a different technique for matrix converter operation introducing fictitious DC link [29]. According to his technique, the output was switched between the most positive input line and the most negative input line. This technique is known as indirect transfer function approach [26].

The method for the control of Matrix Converters was introduced by Braun in 1983 [6] and by Kastner and Rodriguez in 1985 [14]. The first paper to provide the solution of modulation scheme in matrix converters using space modulation was published in 1989 by Huber [10]. Schauder and Neft proved this fact experimentally in 1992 that high quality of input current and output current can be obtained by using matrix converter which comprises of only bidirectional switches [25]. The switching should be performed in such a manner that there should be no high spikes of voltages and current which can damage the switches made up of semi-conductor materials. This fact affected the interests of using matrix converters. This issue has been solved due to the development of micro-processors based controllers and multistage switching and commutation techniques.

Implementation and operation of bidirectional switches [17, 7] under normal condition with active filters [16, 33] are main themes of researches. Lanka Parampil, Ushakomari and Nisha removed the harmonics in three phase inverters using space vector pulse width modulation [13].

In this research work, three phase input and three phase output will be compared and modulated according to requirement by a modulation block. The modulated voltages will be fed to a matrix converter which comprises IGBTs whose operation will be controlled

by applying a PWM and SVM at the gates of the IGBTs. The output from the matrix converter will be fed to different loads like synchronous motor, induction motor, resistive load and RL load whose harmonics will be removed.

The remainder of the paper is organized as follows: Section II focuses on description and mathematical framework of matrix converter, pulse width modulation and space vector modulation Section III emphasizes on mathematical formulation of modulation techniques. Section IV covers the simulation results and Matlab/Simulink models. This research work and its simulation results are concluded in section V.

## 2 Mathematical Formulation of Research Problem

### 2.1 Matrix Converter

A device that changes the frequency of input supply is called matrix converter. The basic components of matrix converter is bidirectional switches which allows any output phase to be connected to any of the three input phase for a given length of line and any desired frequency can be generated. The main advantages of the matrix converter are as follow:

- It eliminates the need of large reactive components which are used in AC-DC-AC type inverters.
- The use of bidirectional switches allows the energy to be regenerated back to the supply or grid.
- This allows the input current waveforms to be sinusoidal and suitable switching can be provided the unity input power factor.
- Due to absence of large reactive elements like capacitors and inductors, the size is small.
- Matrix converter provides more power to weight ratio.
- DC link in back to back inverters is absent.
- The number of switches used are also less.

### 2.2 Different Types of Matrix Converters

#### 2.2.1 AC-DC-AC Converters

These types of converters are known as dc-link converters. There are two types of dc-link converters, which are voltage source inverters and current source inverters. In voltage source inverters, the rectifier stage is realized using diodes bridge while the dc link circuit consists of a shunt capacitor. In current source



inverter the rectifier stage is realized using phase controlled switching bridge and the dc link circuit consists of a series inductor. An AC-DC-AC converter with bidirectional power flow can be realized using a PWM rectifier and then a PWM inverter to the dc link. Energy storing element that is common to both sides forms the dc-link between them.

### 2.2.2 Cyclo-Converters

There is no dc link in cyclo-converters. The cyclo-converter generates the output of variable frequency. The output generated is almost sinusoidal because the segments of the input waveform are transferred to the output side by switching. SCRs are usually used in cyclo-converters. The output frequency of the cyclo-converter can never be greater than the input frequency.

### 2.2.3 Matrix Converter

Matrix Converter converts directly AC to AC without using any dc link. This increases reliability and stability of the system. Bidirectional switches using IGBTs are used commonly in matrix converters. Depending on the number and types of components used, the matrix converters are further classified into many types.

#### a. Sparse Matrix Converter

In this type of matrix converter, the numbers of required switches are less, so the complexity of the gate drive circuit is reduced. The function is identical to direct matrix converter. 18 diodes and 15 switches are required for the sparse type matrix converter.

#### b. Very Sparse Matrix Converter

In this type, the number of diodes is increased and correspondingly the number of switches is reduced as compared to the sparse matrix converter. Though gate drive complexity is reduced but due to increase in the number of diodes, the conduction losses are increased.

#### c. Ultra Sparse Matrix Converter

Only unidirectional switches are used in the input stage of ultra sparse matrix converter. So, these types of matrix converters are used for the variable speed drives which are of low dynamics. The topology of ultra sparse matrix converter introduces phase displacement between input voltages and input currents. Only 12 diodes and 9 switching devices are required for this type of matrix converter.

#### d. Hybrid Matrix Converters

The hybrid matrix converter converts AC/DC/AC but does not use any dc link or reactive elements like capacitor or inductor. The hybrid matrix converters are further classified into two types depending on their operation. If hybrid matrix converter converts both voltage and current commutation in same stage then this is called hybrid direct matrix converters. If current and voltages are converted in different steps then

these are called hybrid indirect matrix converter.

## 2.3 Basics of Matrix Converter:

The matrix converter is a direct AC-AC converter for converting one frequency AC supply to another frequency AC supply without involving an intermediate DC link capacitor.

It has a three phase input supply. The three phase output voltages obtained are  $V_a$ ,  $V_b$  and  $V_c$ . There are nine bidirectional switches from  $S_{11}$  to  $S_{33}$  which represent a nine matrix components mathematically.

The three phase matrix converter converts the three phase input of given amplitude ( $V_i$ ) and frequency ( $f_i$ ) to three phase output of a fixed amplitude ( $V_o$ ) and frequency ( $f_o$ ). Any desirable output frequency can be achieved by this converter. The three phase input voltages of the converter and required output voltages are given by (1) and (2).

$$\begin{bmatrix} V_A \\ V_B \\ V_C \end{bmatrix} = V_i \begin{bmatrix} \cos(\omega_i t) \\ \cos(\omega_i t + \frac{2\pi}{3}) \\ \cos(\omega_i t + \frac{4\pi}{3}) \end{bmatrix} \quad (1)$$

$$\begin{bmatrix} V_a \\ V_b \\ V_c \end{bmatrix} = V_o \begin{bmatrix} \cos(\omega_o t) \\ \cos(\omega_o t + \frac{2\pi}{3}) \\ \cos(\omega_o t + \frac{4\pi}{3}) \end{bmatrix} \quad (2)$$

The input and output voltage are related to each other according to the following matrix equations as shown in (3). Here  $M_{ij}$  is the duty cycle of switch  $S_{11}$  and so on.

$$\begin{bmatrix} V_a(t) \\ V_b(t) \\ V_c(t) \end{bmatrix} = \begin{bmatrix} M_{11} & M_{12} & M_{13} \\ M_{21} & M_{22} & M_{23} \\ M_{31} & M_{32} & M_{33} \end{bmatrix} \begin{bmatrix} V_A(t) \\ V_B(t) \\ V_C(t) \end{bmatrix} \quad (3)$$

Normally, the Matrix Converter is fed by a voltage source and switching should be performed in such a way that none of the input terminals are short circuited. The matrix converter applications are mostly used to drive inductive loads, so the switching should also be performed such that the output phase is never open circuit because it will cause discontinuous supply to load and also the inductive kicks will be caused. The load and source voltages and input and output currents can be expressed as vectors defined by (4) and (5).

$$v_o = \begin{bmatrix} V_a(t) \\ V_b(t) \\ V_c(t) \end{bmatrix}; V_i = \begin{bmatrix} V_A(t) \\ V_B(t) \\ V_C(t) \end{bmatrix} \quad (4)$$

$$i_o = \begin{bmatrix} i_a(t) \\ i_b(t) \\ i_c(t) \end{bmatrix}; i_i = \begin{bmatrix} i_A(t) \\ i_B(t) \\ i_C(t) \end{bmatrix} \quad (5)$$

## 2.4 Pulse Width Modulation

Pulse width modulation is a technique in which a message or a signal is encoded in such a way that it takes



the form of a pulsating signal. This technique is used to encode any information that can be used for transmission. One of the main use of PWM is the control of power that can be supplied to the load. By constantly turning on and off the switching device between load and the source, the value of voltage required is achieved. This phenomenon is carried out at high switching frequency. By varying the duty cycle of the PWM signal, the amount of power supplied to the load is varied. Due to constantly on and off the switching device the desired output waveform will not be smooth. So, in order to keep the output waveform smooth, the switching frequency should be as high as possible.

The switching frequency of a PWM signal is very high which enables the power electronic switching devices to be saturated hardly. So, between on and off state of the switching the transition interval is very short and hence, switching losses are also less. During off state of a controlled switch, there is no flow of current and during on state, the forward voltage drop is almost zero. So, using PWM signal for switching the switching losses are almost zero.

Depending on the requirement, width of the pulse is modulated. The term duty cycle is defined as the ratio of on time of signal to the total time period of the signal as given by (6):

$$\text{Duty Cycle (D)} = t_{on}/t_{on} + t_{off} \quad (6)$$

Duty cycle is represented in percentage like 50%, means on for half of the time and off for half of the time, 100% duty cycle defines fully on.

The steady state operation of a dc to dc type converter is made possible when the reference signal used for PWM generation is constant and does not vary. In dc to dc converters, the reference is assumed to be a dc value. In AC to DC or DC to AC type converters, the reference is assumed to contain the fundamental frequency component of desired output frequency. Similarly in case of multiple or 3 phase converters, the sinusoidal reference signals are shifted by desired amount of phase shift as required in the output voltages. In three phase inverters, the reference signals are shifted by zero degree, 120 degrees and 240 degrees to generate the desired switching. In the generation of switching sequences, reference signals may also contain harmonics mostly 3rd harmonics which are self introduced so that utilization of dc voltages can be increased.

#### 2.4.1 Modulation algorithm for PWM based Matrix Converter

Assuming that the switches are ideal, i.e., no losses occurs in switches. The three phase input supply is

given by (7).

$$\begin{pmatrix} V_A(t) \\ V_B(t) \\ V_C(t) \end{pmatrix} = \begin{pmatrix} \cos(\omega_i t) \\ \cos(\omega_i t + \frac{2\pi}{3}) \\ \cos(\omega_i t + \frac{4\pi}{3}) \end{pmatrix} \times V_{im} \quad (7)$$

The switching is performed after a sequence of time. This time  $T_s$  which is reciprocal to the switching frequency  $f_s$ . The switching time in term of switches shown is defined in (8)

$$\begin{aligned} T_s &= t_{Aa} + t_{Ba} + t_{Ca} \\ &= t_{Ab} + t_{Bb} + t_{Cb} \\ &= t_{Ac} + t_{Bc} + t_{Cc} \\ &= \frac{1}{f_s} \end{aligned} \quad (8)$$

The switching frequency  $f_s$  is constant which means that the length of each sequence is same. The values that are to be received at the output side is say  $V_a(t)$ ,  $V_b(t)$  and  $V_c(t)$  which should be displaced from each other by 120 degrees. The three phase output voltages in terms of switching time are given by (9) (10) and (11)

$$\begin{aligned} V_a(t) &= V_{im} \cos(\omega t) \frac{t_{Aa}}{T_s} + V_{im} \cos(\omega t + \frac{2\pi}{3}) \frac{t_{Ba}}{T_s} \\ &+ \cos(\omega t + \frac{4\pi}{3}) \frac{t_{Ca}}{T_s} \end{aligned} \quad (9)$$

$$\begin{aligned} V_b(t) &= V_{im} \cos(\omega t) \frac{t_{Ab}}{T_s} + V_{im} \cos(\omega t + \frac{2\pi}{3}) \frac{t_{Bb}}{T_s} \\ &+ \cos(\omega t + \frac{4\pi}{3}) \frac{t_{Cb}}{T_s} \end{aligned} \quad (10)$$

$$\begin{aligned} V_c(t) &= V_{im} \cos(\omega t) \frac{t_{Ac}}{T_s} + V_{im} \cos(\omega t + \frac{2\pi}{3}) \frac{t_{Bc}}{T_s} \\ &+ \cos(\omega t + \frac{4\pi}{3}) \frac{t_{Cc}}{T_s} \end{aligned} \quad (11)$$

Now, if the input frequency is increased from  $\omega_i$  to  $\omega_o$  then a modulating frequency  $\omega_m$  has to be added in the input frequency given by (12).

$$\omega_o = \omega_i + \omega_m \quad (12)$$

The output voltage  $V_a(t)$  has zero degree shift in its phase and switches  $t_{Aa}$ ,  $t_{Ba}$  and  $t_{Ca}$  determine the  $V_a(t)$  by connecting to first, second and third phase respectively. Thus to maintain zero degree shift in phase  $V_a(t)$ , the switching sequence  $t_{Ba}$  and  $t_{Ca}$  should be retarded by 120 degrees and 240 degrees respectively. And same is for other two phases. The switching sequences thus formed are given by (13) (14) (15) (16) (17) (18) (19) (20) and (21).





$V_o$  at  $0^\circ$

$$t_{Aa} = \frac{T_s}{3} (1 + 2q\cos(\omega_m t + \theta)) \quad (13)$$

$$t_{Ba} = \frac{T_s}{3} (1 + 2q\cos(\omega_m t + \theta - \frac{2\pi}{3})) \quad (14)$$

$$t_{Ca} = \frac{T_s}{3} (1 + 2q\cos(\omega_m t + \theta - \frac{4\pi}{3})) \quad (15)$$

$V_o$  at  $120^\circ$

$$t_{Ab} = \frac{T_s}{3} (1 + 2q\cos(\omega_m t + \theta - \frac{4\pi}{3})) \quad (16)$$

$$t_{Bb} = \frac{T_s}{3} (1 + 2q\cos(\omega_m t + \theta)) \quad (17)$$

$$t_{Cb} = \frac{T_s}{3} (1 + 2q\cos(\omega_m t + \theta - \frac{2\pi}{3})) \quad (18)$$

$V_o$  at  $240^\circ$

$$t_{Ac} = \frac{T_s}{3} (1 + 2q\cos(\omega_m t + \theta - \frac{2\pi}{3})) \quad (19)$$

$$t_{Bc} = \frac{T_s}{3} (1 + 2q\cos(\omega_m t + \theta - \frac{4\pi}{3})) \quad (20)$$

$$t_{Cc} = \frac{T_s}{3} (1 + 2q\cos(\omega_m t + \theta)) \quad (21)$$

If these values of the time sequence of each switch is substituted in the equation of the desired output voltages as defined before, then the modulation matrix is given by (22).

$$M(t) = \frac{1}{3} \begin{bmatrix} 1 & 1 & 1 \\ 1 & 1 & 1 \\ 1 & 1 & 1 \end{bmatrix} + \frac{2q}{3} \begin{bmatrix} \cos(\omega_m t) & \cos(\omega_m t - \frac{2\pi}{3}) & \cos(\omega_m t - \frac{4\pi}{3}) \\ \cos(\omega_m t - \frac{4\pi}{3}) & \cos(\omega_m t) & \cos(\omega_m t - \frac{2\pi}{3}) \\ \cos(\omega_m t - \frac{2\pi}{3}) & \cos(\omega_m t - \frac{4\pi}{3}) & \cos(\omega_m t) \end{bmatrix} \quad (22)$$

with  $\omega_m = (\omega_0 - \omega_i)$ . The output and input voltages are related to each other with the help of modulation matrix as given in (23).

$$V_o(t) = M(t).V_i(t) \quad (23)$$

So the output voltages are given by (24).

$$V(t) = \frac{1}{3} \begin{bmatrix} 1 & 1 & 1 \\ 1 & 1 & 1 \\ 1 & 1 & 1 \end{bmatrix} + \frac{2q}{3} \begin{bmatrix} \cos(\omega_m t) & \cos(\omega_m t - \frac{2\pi}{3}) & \cos(\omega_m t - \frac{4\pi}{3}) \\ \cos(\omega_m t - \frac{4\pi}{3}) & \cos(\omega_m t) & \cos(\omega_m t - \frac{2\pi}{3}) \\ \cos(\omega_m t - \frac{2\pi}{3}) & \cos(\omega_m t - \frac{4\pi}{3}) & \cos(\omega_m t) \end{bmatrix} \times \begin{bmatrix} V_m(\omega_m t) \\ V_m(\omega_m t - \frac{2\pi}{3}) \\ V_m(\omega_m t - \frac{4\pi}{3}) \end{bmatrix} \quad (24)$$

## 2.5 Space Vector Modulation

The generated three phase voltages vary from each other by 120 degrees with the frequency same as of reference signal. The reference signal can be varied by varying the time period  $T_s$  as  $T_s = 1/f_s$ , where  $f_s$  is switching frequency. The reference signal can be generated from a three phase using  $d-q$  or  $\alpha-\beta-\gamma$  transformation. Various combinations exist for selecting the switching sequence of switches but each strategy has its own switching losses as shown in figure 1.

Vector	A+	B+	C+	A-	B-	C-
$V_0 = (000)$	OFF	OFF	OFF	ON	ON	ON
$V_1 = (100)$	ON	OFF	OFF	OFF	ON	ON
$V_2 = (110)$	ON	ON	OFF	OFF	OFF	ON
$V_3 = (010)$	OFF	ON	OFF	ON	OFF	ON
$V_4 = (011)$	OFF	ON	ON	ON	OFF	OFF
$V_5 = (001)$	OFF	OFF	ON	ON	ON	OFF
$V_6 = (101)$	ON	OFF	ON	OFF	ON	OFF
$V_7 = (111)$	ON	ON	ON	OFF	OFF	OFF

$V_{AB}$	$V_{BC}$	$V_{CA}$	state
0	0	0	Zero
$+V_{dc}$	0	$-V_{dc}$	Active
0	$+V_{dc}$	$-V_{dc}$	Active
$-V_{dc}$	$+V_{dc}$	0	Active
$-V_{dc}$	0	$+V_{dc}$	Active
0	$-V_{dc}$	$+V_{dc}$	Active
$+V_{dc}$	$-V_{dc}$	0	Active
0	0	0	Zero

Figure 1: This table shows combination of switching sequence.

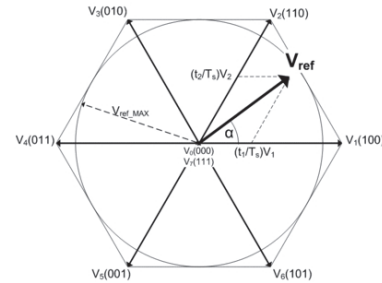


Figure 2: Vector representation of SVM signal

Two zero vectors and six active vectors can be represented in the form of a hexagon in such a way that the length of each vector represents the magnitude of voltages as shown in figure 2. The rotation of vectors represents the angular speed of the system. As previously discussed for balanced loads, space vectors are represented in 2-Dimensional figure. To minimize the time taken during toggling of states and to maintain the effective frequency of the switches used at minimum, the SVM topology prefers switching between two nearest active states. Using this approach, in every step only one leg is affected. Using proper switching, the effective output voltage to input voltage ratio can be increased to more than 90.6%.

The six active vectors can be represented by (25).

$$V_k = \frac{2}{3} V_d e^{j(k-1)\frac{\pi}{3}} \text{ with } k = (1, 2, \dots, 6) \quad (25)$$



SVM vectors are represented graphically by equally dividing six sectors of a hexagon. The switching of only one inverter leg provides minimum switching frequency and optimum harmonic performance. Using, SVM we can define any reference vector as a combination of two active vectors at any instant of time. Suppose that in figure 2,  $V_{ref}$  shown is in  $k$  sector and the active vectors adjacent to  $V_{ref}$  are  $V_k$  and  $V_{k+1}$ . So, the reduced equation is given by (26).

$$V_{ref} \cdot \frac{T_s}{2} = V_k \cdot T_k + V_{k+1} \cdot T_{k+1} \quad (26)$$

Where  $T_s$  is switching period. If this equation is split in real and imaginary parts, then it is given by (27) and (28).

$$\begin{bmatrix} V_{alpha} \\ V_{beta} \end{bmatrix} * \frac{T_s}{2} = \frac{2}{3} V_d T_k \begin{bmatrix} \cos \frac{(k-1) * \pi}{3} \\ \sin \frac{(k-1) * \pi}{3} \end{bmatrix} + \frac{2}{3} V_d T_{k+1} \begin{bmatrix} \cos \frac{(k) * \pi}{3} \\ \sin \frac{(k) * \pi}{3} \end{bmatrix} \quad (27)$$

$$\begin{bmatrix} V_{alpha} \\ V_{beta} \end{bmatrix} * \frac{T_s}{2} = \frac{2}{3} V_d \begin{bmatrix} \cos \frac{(k-1) * \pi}{3} & \cos \frac{(k) * \pi}{3} \\ \sin \frac{(k-1) * \pi}{3} & \sin \frac{(k) * \pi}{3} \end{bmatrix} \begin{bmatrix} T_k \\ T_{k+1} \end{bmatrix} \quad (28)$$

$k$  is determined by taking the argument of the reference vector given by (29).

$$\frac{(k-1) * \pi}{3} \leq \arg \begin{bmatrix} V_a \\ V_b \end{bmatrix} \leq \frac{k * \pi}{3} \quad (29)$$

$V_{ref}$  makes a circular path of radius  $V_{ref}$  at an angular velocity in the complex plane. So, larger the radius of the trajectory circle, largest is the magnitude of voltage that can be achieved. This circle is tangential to the mid points of the lines connecting the ends of the active state vectors. The maximum achievable phase voltages are given by (30).

$$|V_{ref}|_{max} = \frac{2}{3} V_d \frac{\sqrt{3}}{2} = \frac{1}{\sqrt{3}} V_d \quad (30)$$

Following the definition of modulation index introduced in above, the corresponding maximum modulation index is given by (31).

$$m_{max\ cont} = \frac{|V_{ref}|_{max}}{V_{max, sixstep}} = \frac{\frac{1}{\sqrt{3}} \cdot V_d}{\frac{2}{\pi} \cdot V_d} = \frac{\pi}{2\sqrt{3}} = 0.906 \quad (31)$$

With the definition of modulation index the computation of the inverter switching times does not require the knowledge of the adopted DC-link voltage but depends only on the desired modulation index.

Only space vector topology provides the best suitable switching sequence according to the type of loads like pulsating load, non-linear load and static load etc. The advantages of SVM are:

- THD of the output voltage is low
- DC bus utilization in case of SVM is at least 15% more than the PWM technique used
- SVM offers low peak currents in controlled switches as compared to PWM.
- Higher performance, efficiency and reliability is achieved using SVM as compared to PWM based inverters of similar type.

Switching Configuration List	Switches	Switches	ON	$V_o$	$a_o$	$i_i$	$b_o$
1	$S_{11}$	$S_{22}$	$S_{33}$	$\frac{2}{3}V_{123}$	0	$\frac{2}{3}V_{101}$	$\frac{2}{3}$
4	$S_{12}$	$S_{21}$	$S_{33}$	$\frac{2}{3}V_{123}$	0	$\frac{2}{3}V_{101}$	$\frac{2}{3}$
2	$S_{12}$	$S_{23}$	$S_{33}$	$\frac{2}{3}V_{231}$	0	$\frac{2}{3}V_{101}$	$\frac{2}{3}$
2	$S_{13}$	$S_{22}$	$S_{32}$	$\frac{2}{3}V_{231}$	0	$\frac{2}{3}V_{101}$	$\frac{2}{3}$
3	$S_{13}$	$S_{21}$	$S_{31}$	$\frac{2}{3}V_{311}$	0	$\frac{2}{3}V_{101}$	$\frac{2}{3}$
3	$S_{11}$	$S_{23}$	$S_{33}$	$\frac{2}{3}V_{123}$	0	$\frac{2}{3}V_{101}$	$\frac{2}{3}$
3	$S_{11}$	$S_{23}$	$S_{33}$	$\frac{2}{3}V_{123}$	0	$\frac{2}{3}V_{101}$	$\frac{2}{3}$
4	$S_{12}$	$S_{21}$	$S_{32}$	$\frac{2}{3}V_{123}$	$\frac{2}{3}$	$\frac{2}{3}V_{102}$	$\frac{2}{3}$
4	$S_{11}$	$S_{22}$	$S_{31}$	$\frac{2}{3}V_{123}$	$\frac{2}{3}$	$\frac{2}{3}V_{102}$	$\frac{2}{3}$
5	$S_{13}$	$S_{22}$	$S_{33}$	$\frac{2}{3}V_{231}$	$\frac{2}{3}$	$\frac{2}{3}V_{102}$	$\frac{2}{3}$
5	$S_{12}$	$S_{23}$	$S_{32}$	$\frac{2}{3}V_{231}$	$\frac{2}{3}$	$\frac{2}{3}V_{102}$	$\frac{2}{3}$
6	$S_{14}$	$S_{23}$	$S_{31}$	$\frac{2}{3}V_{311}$	$\frac{2}{3}$	$\frac{2}{3}V_{102}$	$\frac{2}{3}$
6	$S_{13}$	$S_{21}$	$S_{33}$	$\frac{2}{3}V_{311}$	$\frac{2}{3}$	$\frac{2}{3}V_{102}$	$\frac{2}{3}$
7	$S_{12}$	$S_{22}$	$S_{31}$	$\frac{2}{3}V_{123}$	$\frac{2}{3}$	$\frac{2}{3}V_{103}$	$\frac{2}{3}$
7	$S_{11}$	$S_{21}$	$S_{32}$	$\frac{2}{3}V_{123}$	$\frac{2}{3}$	$\frac{2}{3}V_{103}$	$\frac{2}{3}$
8	$S_{13}$	$S_{23}$	$S_{32}$	$\frac{2}{3}V_{231}$	$\frac{2}{3}$	$\frac{2}{3}V_{103}$	$\frac{2}{3}$
8	$S_{12}$	$S_{22}$	$S_{33}$	$\frac{2}{3}V_{231}$	$\frac{2}{3}$	$\frac{2}{3}V_{103}$	$\frac{2}{3}$
9	$S_{11}$	$S_{21}$	$S_{33}$	$\frac{2}{3}V_{311}$	$\frac{2}{3}$	$\frac{2}{3}V_{103}$	$\frac{2}{3}$
9	$S_{13}$	$S_{23}$	$S_{31}$	$\frac{2}{3}V_{311}$	$\frac{2}{3}$	$\frac{2}{3}V_{103}$	$\frac{2}{3}$
0 <sub>1</sub>	$S_{11}$	$S_{21}$	$S_{31}$	0	—	0	—
0 <sub>2</sub>	$S_{12}$	$S_{22}$	$S_{32}$	0	—	0	—
0 <sub>3</sub>	$S_{13}$	$S_{23}$	$S_{33}$	0	—	0	—

Figure 3: This table shows that 27 different combinations of switches are obtained using 9 bidirectional switches. Keeping in view the modulation constraints only 21 switching combinations are useful. The last three switching combinations provide zero vectors. The other six combinations are not useful because these combinations can not provide the reference vectors.

### 3 Modulation Techniques

The relations between input and output voltages are related to the states of the nine bidirectional switches with the condition that  $0 < M_{ij} < 1$  where  $i, j = 1, 2, 3$ . The variable  $M_{ij}$  represents the duty cycle of 9 bidirectional switches [31, 32]. The duty cycle must satisfy the following equations (32) (33) and (34).

$$M_{11} + M_{12} + M_{13} = 1 \quad (32)$$

$$M_{21} + M_{22} + M_{23} = 1 \quad (33)$$

$$M_{31} + M_{32} + M_{33} = 1 \quad (34)$$





Venturini proposed the method whose modulation function gives maximum value of voltage transfer ratio of 0.5 which is very low and is given by (35).

$$M_{ij} = \frac{1}{3} \cos[b_o - (j-1)\frac{2\pi}{3}] + \frac{2q}{3} [\cos a_o - (i-1)\frac{2\pi}{3}] * \cos[b_o - (j-1)\frac{2\pi}{3}] \quad (35)$$

This method was modified by optimum method to increase the voltage transfer ratio to 0.866 and its modulation function is given by (36).

$$M_{ij} = \frac{1}{3} \{1 + 2q[\cos b_h - (j-1)\frac{2\pi}{3}] * [\cos(a_o - (i-1)\frac{2\pi}{3}) - \frac{1}{6} \cos(3a_o) + (\frac{1}{2}\sqrt{3}) \cos(3b_h)] - (\frac{2}{3}\sqrt{3})q \cos[(4b_h - (j-1)\frac{2\pi}{3}) - \cos(2b_h + (j-1)\frac{2\pi}{3})]\} \quad (36)$$

## 4 Simulation and Results

Matlab/ Simulink is used for simulation and results. A complete step by step process is shown in a figure 4. A three phase source is required whose amplitude and frequency can be varied. Modulation block also modulates the switching intervals for the switches which in our simulation are insulated gate bipolar junction transistors (IGBTs).

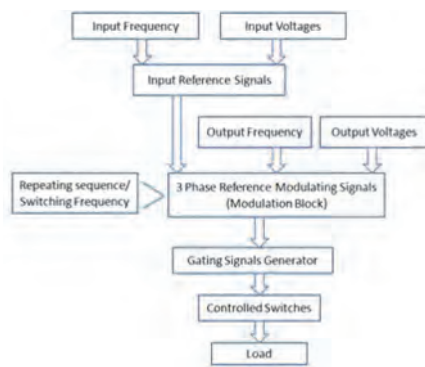


Figure 4: Flow Chart for the Implementation of PWM and SVM based Matrix Converters

The switching intervals are defined by using the solution as provided by the Venturini Method [31, 32]. Using Venturini method, two solutions are obtained.

The first solution is given by (37).

$$M_1(t) = \frac{1}{3} \begin{bmatrix} 1 & 1 & 1 \\ 1 & 1 & 1 \\ 1 & 1 & 1 \end{bmatrix} + 2q \begin{bmatrix} \cos(\omega_m t) & \cos(\omega_m t - \frac{2\pi}{3}) & \cos(\omega_m t - \frac{4\pi}{3}) \\ \cos(\omega_m t - \frac{4\pi}{3}) & \cos(\omega_m t) & \cos(\omega_m t - \frac{2\pi}{3}) \\ \cos(\omega_m t - \frac{2\pi}{3}) & \cos(\omega_m t - \frac{4\pi}{3}) & \cos(\omega_m t) \end{bmatrix} \quad (37)$$

with  $\omega_m = (\omega_0 - \omega_i)$ . This yields  $\phi_i = \phi_o$ , i.e. the input phase displacement is the same as the load phase displacement. The alternative solution is given by (38).

$$M_2(t) = \frac{1}{3} \begin{bmatrix} 1 & 1 & 1 \\ 1 & 1 & 1 \\ 1 & 1 & 1 \end{bmatrix} + 2q \begin{bmatrix} \cos(\omega_m t) & \cos(\omega_m t - \frac{2\pi}{3}) & \cos(\omega_m t - \frac{4\pi}{3}) \\ \cos(\omega_m t - \frac{2\pi}{3}) & \cos(\omega_m t - \frac{4\pi}{3}) & \cos(\omega_m t) \\ \cos(\omega_m t - \frac{4\pi}{3}) & \cos(\omega_m t) & \cos(\omega_m t - \frac{2\pi}{3}) \end{bmatrix} \quad (38)$$

with  $\omega_m = -(\omega_0 + \omega_i)$ . This yields  $\phi_i = -\phi_o$ , i.e. the input phase displacement is the reverse of the load phase displacement. Combining the two solutions provides the means for input displacement factor control given by (39).

$$[M(t)] = \alpha_1[M_1(t)] + \alpha_2[M_2(t)] \quad (39)$$

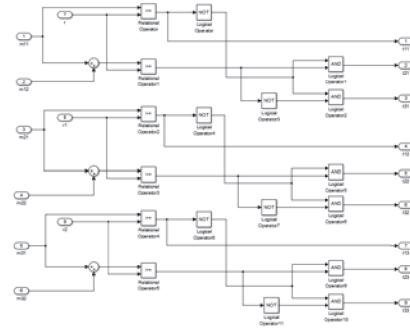


Figure 5: Gating Signal Generator

Combined solution allows input displacement factor control. This can be explained by taking the example of an inductive load. If:

- $a_1 = a_2$  : input is resistive (unity displacement factor)
- $a_1 > a_2$  : input is inductive (lagging displacement factor)
- $a_1 < a_2$  : input is capacitive (leading displacement factor)

The output voltages are thus produced by using these switching intervals and the input voltages.



Since, the transfer ratio is 0.5, so the output voltages cannot be increased by the half value of input voltages. Gating signal generator is shown in figure 5. The six signals of the switching intervals are compared with the repeating sequence taken as reference to produce the gate signals for the IGBTs. This is pulse width modulation. Matrix converter and space vector modulation based matrix converters are shown in figures 6 and 7 respectively.

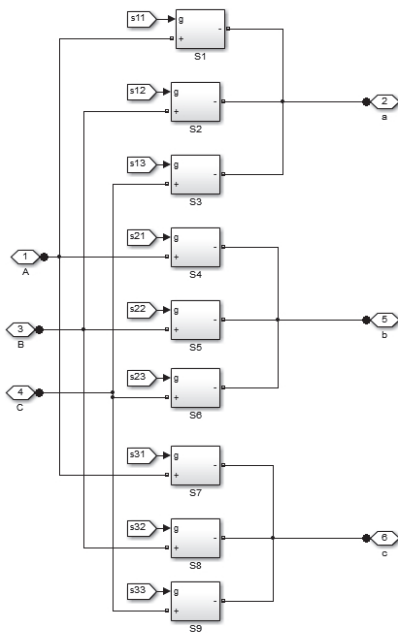


Figure 6: Matrix Converter

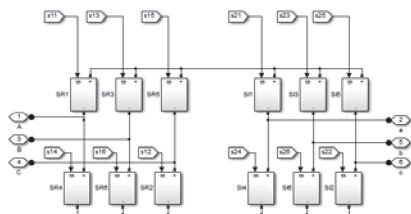


Figure 7: SVM based Matrix Converter

## 4.1 Case Studies

### 4.1.1 Test Case IA: Fixed Input Frequency and Variable Output Frequency

In the test case IA, input frequency is fixed and output frequency is varied. It is observed that change in output frequency does not affect the input frequency when PWM and SVM based AC to AC matrix converters are employed as shown in figures 10, 11 and 12.

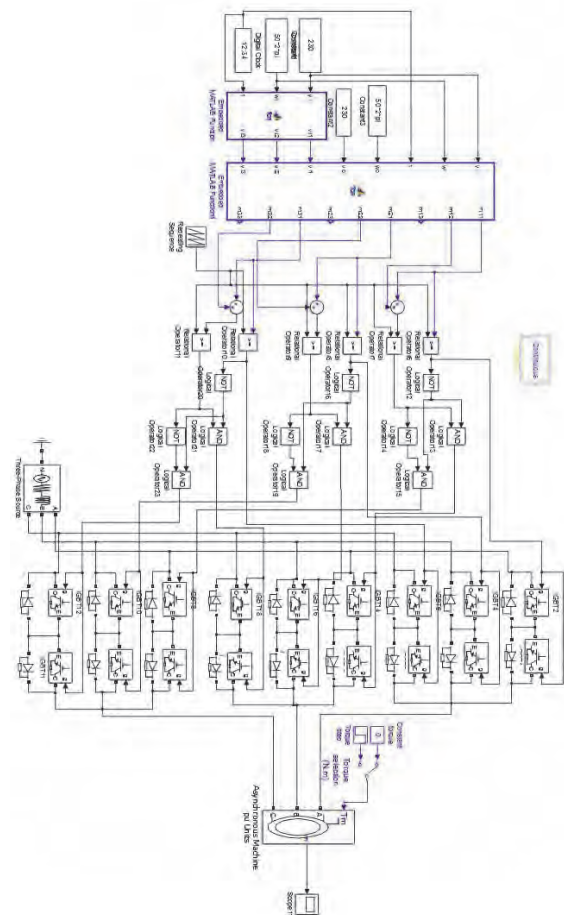


Figure 8: Circuit Diagram of PWM based Matrix Converter

### 4.1.2 Test Case IB: Variable Input Frequency and Fixed Output Frequency

In the test case IB, output frequency is fixed and input frequency is varied. It is observed that change in input frequency does not affect the output frequency when PWM and SVM based AC to AC matrix converters are employed as shown in figures 13, 14 and 15.

### 4.1.3 Test Case IIA: Fixed Input Voltage and Variable Output Voltage

In the test case IIA, input voltage is fixed and output voltage is varied. It is observed that change in output voltage does not affect the input voltage when PWM and SVM based AC to AC matrix converters are employed as shown in figures 16, 17 and 18.

### 4.1.4 Test Case IIIB: Fixed Output Voltage and Variable Input Voltage

In the test case III, output voltage is fixed and input voltage is varied. It is observed that change in input voltage does not affect the output voltage when PWM and SVM based AC to AC matrix converters are employed as shown in figures 19, 20 and 21.



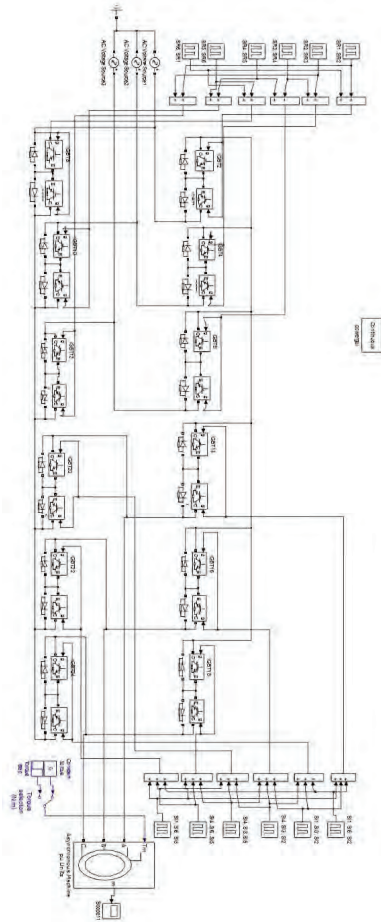


Figure 9: Circuit Diagram of SVM based Matrix Converter

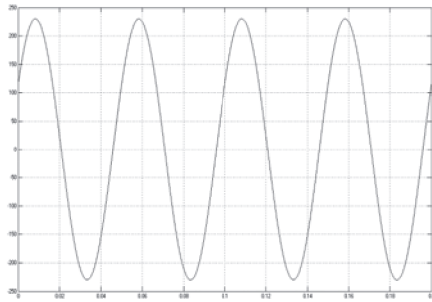


Figure 10: 20Hz Output Signal with 50Hz Input Signal Frequency.

#### 4.1.5 Test Case III A: FFT Analysis for Pulse Width Modulation Based Matrix Converter with Fixed Input Frequency

Fast Fourier Transform Analysis for PWM based matrix converter is carried out as shown in figures 22, 23 and 24. It is found that this matrix converter maximizes the fundamental content of the characteristics by reducing the harmonic content. Any desired output frequency with maximum fundamental content can be obtained with this model by fixing the supply frequency.

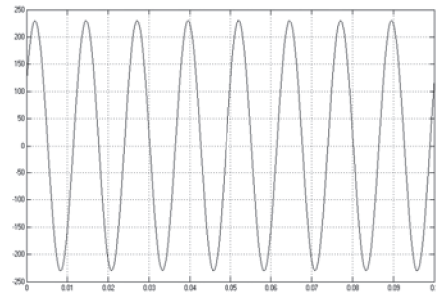


Figure 11: 80Hz Output Signal with 50Hz Input Signal Frequency.

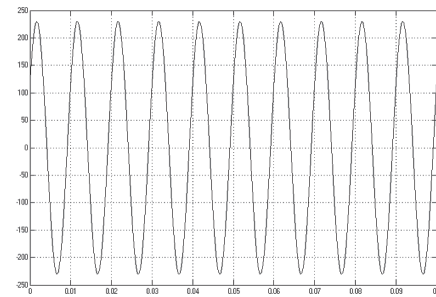


Figure 12: 100Hz Output Signal with 50Hz Input Signal Frequency.

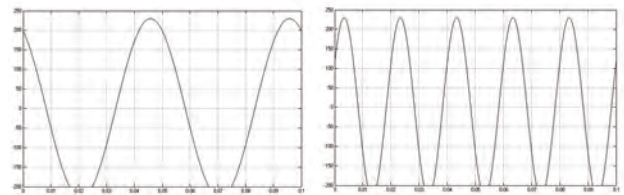


Figure 13: 20Hz Input Signal with 50Hz Output Signal Frequency.

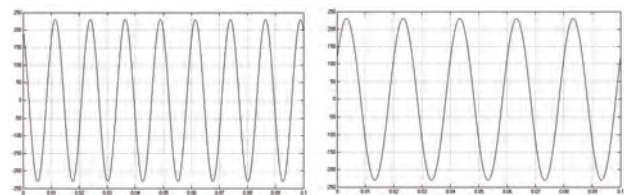


Figure 14: 80Hz Input Signal with 50Hz Output Signal Frequency.

#### 4.1.6 Test Case III B: FFT Analysis for Pulse Width Modulation Based Matrix Converter with Fixed Output Frequency

Fast Fourier Transform Analysis for PWM based matrix converter is carried out as shown in figures 25, 26 and 27. It is found that this matrix converter maximizes the fundamental content of the characteristics by reducing the harmonic content. Any desired input frequency with maximum fundamental content can be supplied with this model by fixing the output



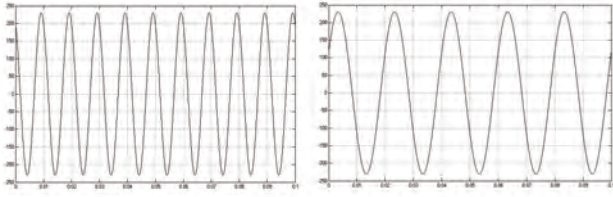


Figure 15: 100Hz Input Signal with 50Hz Output Signal Frequency.

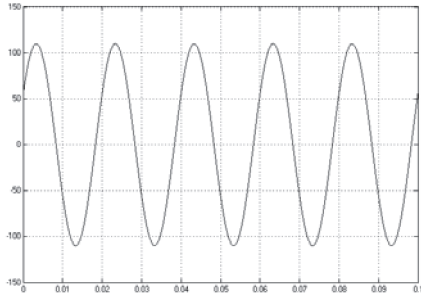


Figure 16: 110V Output Signal with 220V Input Signal Frequency.

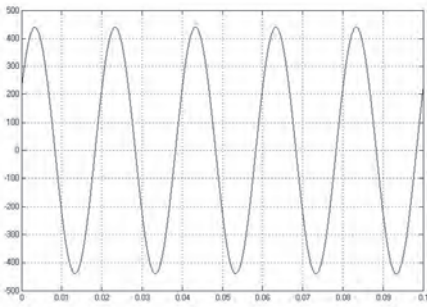


Figure 17: 440V Output Signal with 220V Input Signal Frequency.

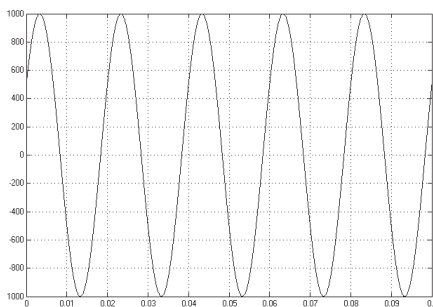


Figure 18: 1000V Output Signal with 220V Input Signal Frequency.

frequency or in other words, fixed frequency applications can work smoothly irrespective of the variation in the supply frequency by deploying this model.

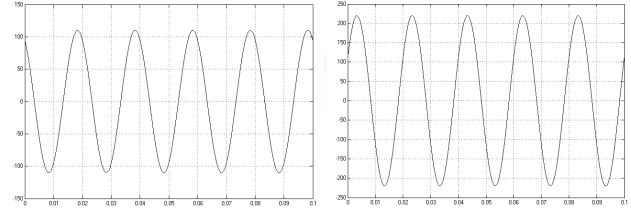


Figure 19: 110V Input Signal with 220V Output Signal Frequency.

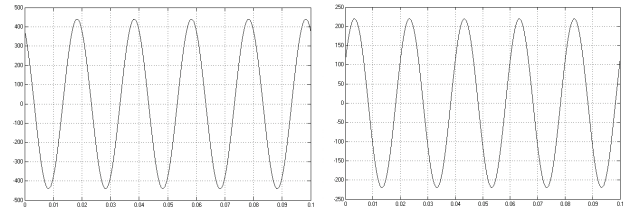


Figure 20: 440V Input Signal with 220V Input Signal Frequency.

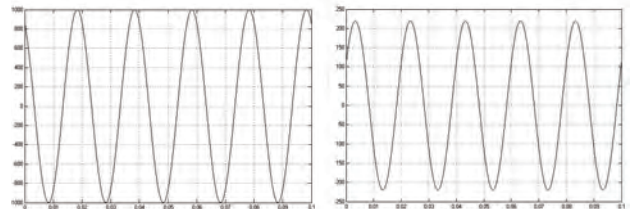


Figure 21: 1000V Output Signal with 220V Input Signal Frequency.

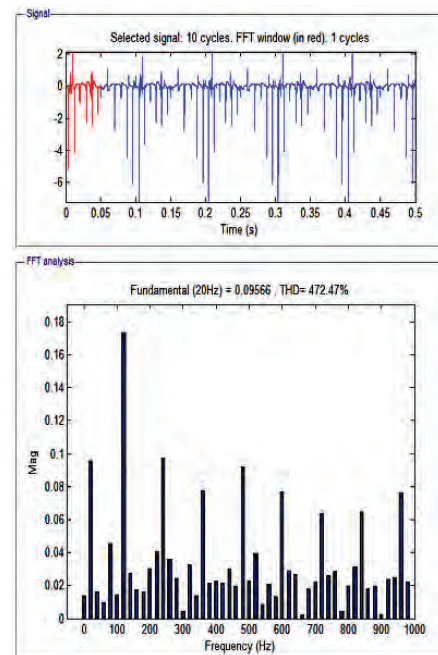


Figure 22: FFT analysis of 20Hz Output Signal with 50Hz Input Signal.





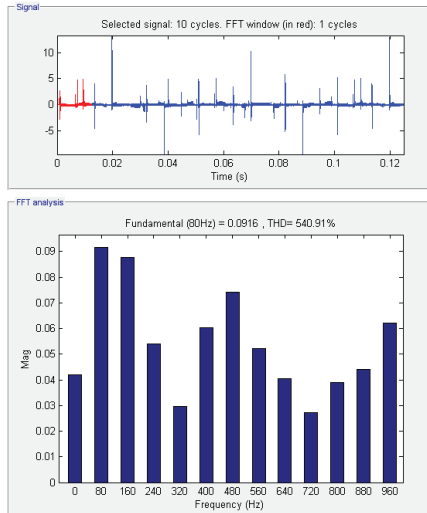


Figure 23: FFT analysis of 80Hz Output Signal with 50Hz Input Signal.

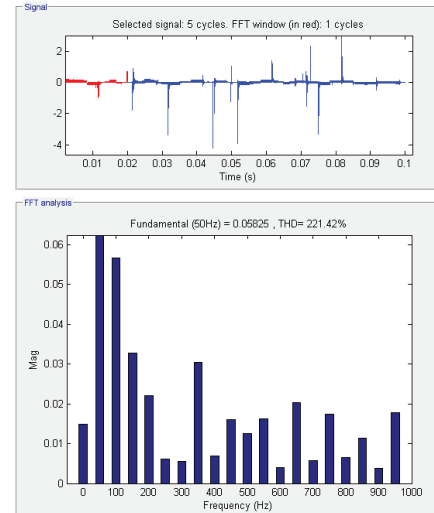


Figure 25: FFT analysis of Fixed Output 50Hz with 20Hz Input Signal.

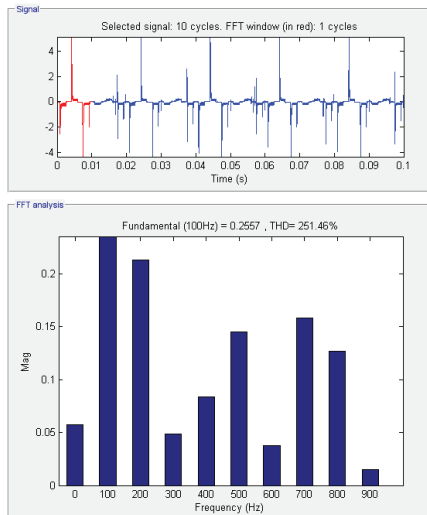


Figure 24: FFT analysis of 100Hz Output Signal with 50Hz Input Signal.

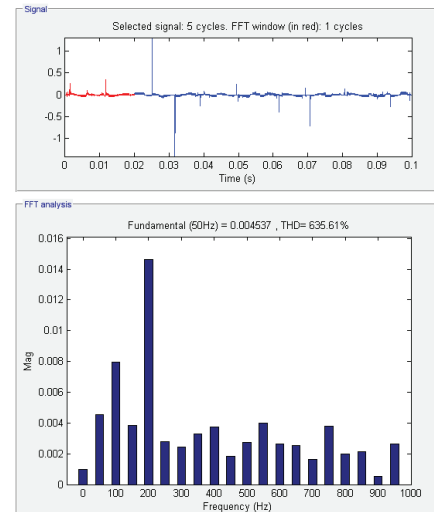


Figure 26: FFT analysis of Fixed Output 50Hz with 80Hz input Signal.

#### 4.1.7 Test Case IV A: FFT Analysis for Space Vector Modulation Based Matrix Converter with Fixed Input Frequency

Fast Fourier Transform Analysis for SVM based matrix converter is carried out as shown in figures 28, 29 and 30. It is found that this matrix converter maximizes the fundamental content of the characteristics by reducing the harmonic content. Any desired output frequency with maximum fundamental content can be supplied with this model by fixing the input frequency. Total harmonic distortion is lower as compared to PWM based matrix converter.

#### 4.1.8 Test Case IV B: FFT Analysis for Space Vector Modulation with Fixed Output Frequency

Fast Fourier Transform Analysis for PWM based matrix converter is carried out as shown in figures 31, 32 and 33. It is found that this matrix converter maximizes the fundamental content of the characteristics by reducing the harmonic content. Any desired input frequency with maximum fundamental content can be supplied with this model by fixing the output frequency or in other words, fixed frequency applications can work smoothly irrespective of the variation in the supply frequency by deploying this model. Total harmonic distortion is lower as compared to PWM based matrix converter.



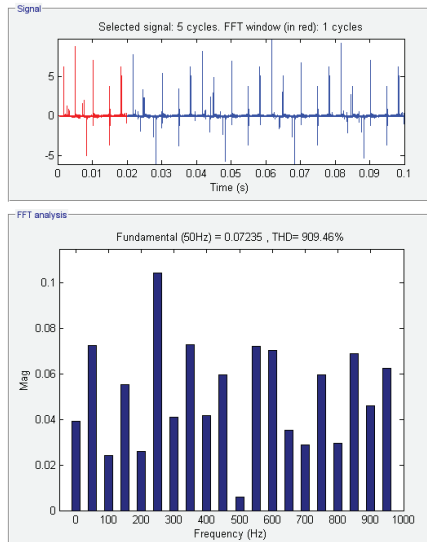


Figure 27: FFT analysis of Fixed Output 50Hz with 100Hz input Signal.

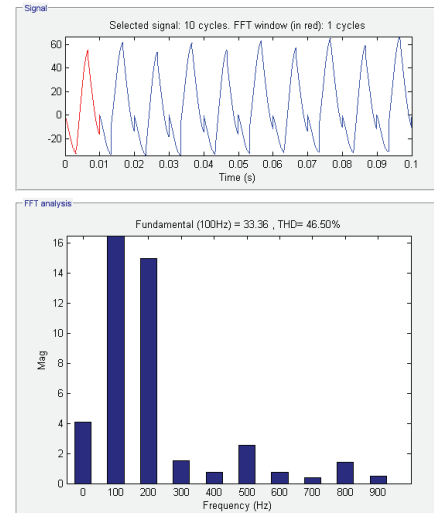


Figure 30: FFT analysis of 100Hz Output with 50Hz Input Signal.

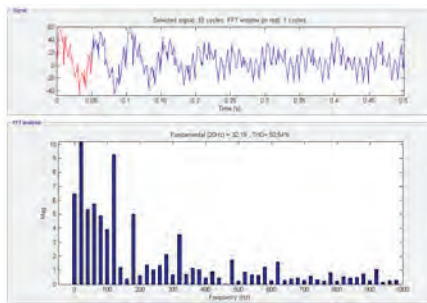


Figure 28: FFT analysis of 20Hz Output with 50Hz Input Signal.

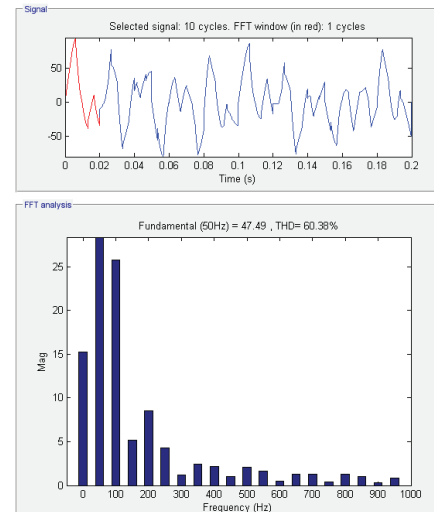


Figure 31: FFT analysis of output with 50Hz Output and 20Hz Input Signal.

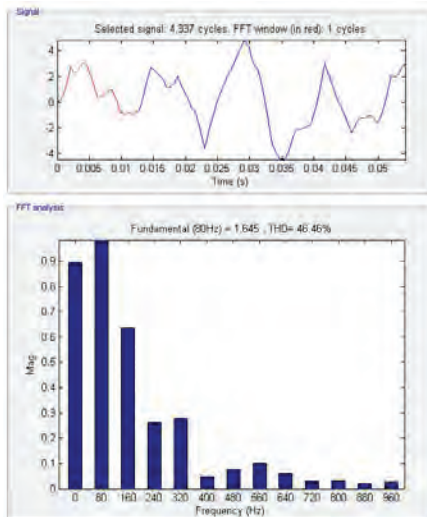


Figure 29: FFT analysis of 80Hz Output with 50Hz Input Signal.

## 5 Conclusion

In this research, PWM and SVM based three phase AC to AC matrix converters are developed. Simula-

tions are performed on Matlab. It is found out that PWM and SVM based matrix converter can be deployed to achieve any desired output and input characteristics. These converters are highly applicable for adjustable speed drives or variable frequency drives because in these proposed models it is shown that irrespective of any supply frequency, variable desired frequency can be attained. Secondly, this proposed model has revolutionized the applications requiring variable voltages. Any desired output voltage can be achieved without taking into consideration of input voltage and vice versa. Interconnected systems can be free of synchronization issues by employing these converters. Further, harmonic contents are greatly reduced and it has maximized the fundamental content of the desired characteristics. SVM based matrix converter offers low total harmonic distortion than PWM





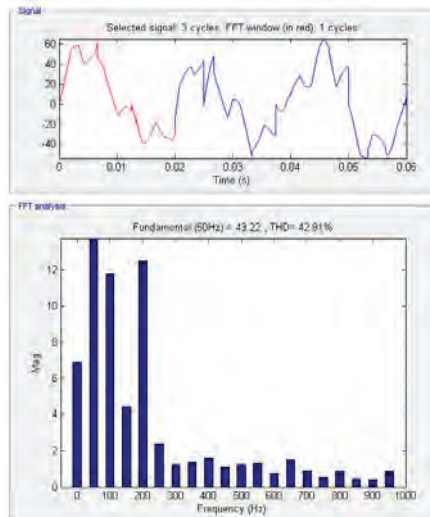


Figure 32: FFT analysis of output with 50Hz Output and 80Hz Input Signal.

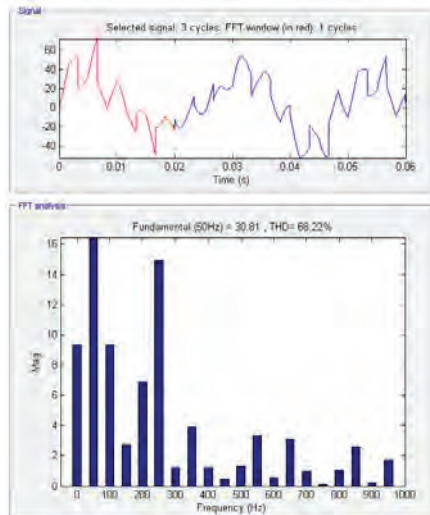


Figure 33: FFT analysis of output with 50Hz Output with 100Hz Input Signal.

based matrix converter.

## References

- [1] Recommended practices and requirements for harmonics control in electrical power systems. IEEE 519, 1993.
- [2] Limits for harmonic current emission (equipment input current 16 a per phase). IEC 1000 – 3 – 2 International Standard, 1995.
- [3] Limits for harmonic current emission (equipment input current up to and including 16 a per phase). IEC 61000-3-2 International Standard, 2000.
- [4] H. Akagi and H. Fujita. New power line conditioner for harmonic compensation in power systems. *IEEE Trans. Power Del.*, 10(3):1570–1575, July 1995.
- [5] H. Akagi, Y. Tsukamoto, and A. Nabae. Analysis and design of an active power filter quad-series voltage source pwm converters. *IEEE Trans. Ind. Electron.*, 26(1):93–98, 1990.
- [6] M. Braun and K. Hasse. A direct frequency changer with control of input reactive power. *IFAC Control in Power Electronics and Electrical Drives*, pages 187–194, 1983.
- [7] J. Chang, T. Sun, A. Wang, and D. Braun. Medium power ac-ac converter based on integrated bidirectional power modules, adaptive commutation and dsp control. In *Conf. Rec. IEEE Ind. Application Source Annual Meeting*, 1999.
- [8] E. Peralta-Sánchez E. L. Áñez-Robles, J.J. Rodríguez-Rivas and O. Carranza-Castillo. Voltage regulation of a matrix converter with balanced and unbalanced three-phase loads. *Journal of Applied Research and Technology*, 13(5):510 – 522, 2015.
- [9] F. Schafmeister. *Sparse and Indirect Matrix Converter*. PhD thesis, ETH Zurich, Switzerland, 2007.
- [10] L. Huber, D. Borojevic, and N. Burany. Voltage space vector based pwm control of forced commutated cyclo converters. *IEEE IECON*, pages 106–111, 1989.
- [11] J. Arrillaga and N. Watson. *Power System Harmonics*. Wiley, New York, 2003.
- [12] V. Jones and B. Bose. A frequency step-up cyclo converter using power transistors in inverse-series mode. *Int. Journal Electronics*, 41(6):573–587, 1976.
- [13] Nisha G. K., Ushakumari S., and Lakshampillai Z. V. In *Proceedings of the international conference of engineers and computer scientists (IMECS) 2012*, Hong Kong, March 2012.
- [14] G. Kastner and J. Rodriguez. A forced commutated cyclo converter with control of the source and load currents. *Proc. EPE85*, x(x):1141–1146, 1985.
- [15] M.P. Kazmierkowski, R. Krishnan, and F. Blaabjerg. *Control in Power Electronics: Selected Problems*. PhD thesis, San Diego, 2002.
- [16] C. Klumpner, I. Boldea, and F. Blaabjerg. Short term ride through capabilities for direct frequency converters. In *Conf. Rec. IEEE PESC00*, 2000.



- [17] C. Klumpner, P. Nielsen, I. Boldea, and F. Blaabjerg. New steps towards a low cost power electronic building block for matrix converters. In *Conf. Rec. IEEE Ind. Application Socuce, Annual Meeting*, 2000.
- [18] J.W. Kolar. Vorrichtung zur quasi direkten pulsbreitengesteuerter energieumformung zwischen dreiphasennetzen, July 2001.
- [19] J.W Kolar, F.Schafmeister, S.D Round, and H. Ertl. Three phase ac to ac sparse matrix converter. volume 2, pages 777–791, Dalas, USA, March 2002.
- [20] J.W Kolar, F.Schafmeister, S.D Round, and H. Ertl. Three phase ac to ac sparse matrix converter. *Transactions Power Electronics*, 22(5):1649–1661, 2007.
- [21] O. Lopez, J. Alvarez, J. Doval-Gandoy, and F. D. Freijedo. Multilevel multiphase space vector pwm algorithm. *IEEE transactions on Industrial Electronics*, 55(5):244–251, 2008.
- [22] L.Wei, T.A.Lipo, and H.Chan. Matrix converter topologies with reduced number of switches. pages 125–130, Blacksburg, USA, April 2002.
- [23] L. Nezli M.M. Rezaoui, A. Kouzou and M.O. Mahmoudi. Comparative analysis of pwm strategies of venturini and roy for the control of a [3ÄÜ3] matrix converter for renewable energies sources. In *Int. Multi-Conf. on Signals Devices and Power Electrical Systems*, 2013.
- [24] J. F. Moynihan, M. G. Egan, and J. M. D. Murphy. Theoretical spectra of space vector modulated waveforms. *IEEE proceedings of Electrical Power Applications*, 145(1), January 1998.
- [25] C. L. Neft and C. D. Schauder. Theory and design of a 30-hp matrix converter. *IEEE Trans. Ind. Applicat.*, 28(3):546–551, May/June 1992.
- [26] J. Oyama, T. Higuchi, E. Yamada, T. Koga, and T. Lipo. New control strategy for matrix converter. In *Conf. Rec. IEEE PESC89*, pages 360–367, 1989.
- [27] D. Paice. *Power Electronic Converter Harmonics*, chapter Multiple Methods for Clean Power. IEEE Press, 2<sup>nd</sup> edition, 1996.
- [28] F. Z. Peng, H. Akagi, and A. Nabae. A new approach to harmonic compensation in power system: A combines system of shunt passive and series active filters. *IEEE Trans. Ind. Electron*, 26(6):983–990, December 1990.
- [29] J. Rodriguez. A new control technique for ac-ac converters. *IFAC Control in Power Electronics and Electrical Drives*, pages 203–208, 1983.
- [30] Prakash. T. Patil Sagar. S. Pawar. Design of three phase matrix converter ac-ac utility power supply using spwm technique. *Int. Journal of Engineering Research and Applications*, 5(4):125–128, 2015.
- [31] M. Venturini. A new sine wave in sine wave out, conversion technique which eliminates reactive elements. In *Proc. POWERCON 7*, pages E301–E315, 1980.
- [32] M. Venturini and A. Alesina. The generalized transformer: A new bidirectional sinusoidal waveform frequency converter with continuously adjustable input power factor. In *Conf. Rec. IEEE PESC80*, pages 242–252, 1980.
- [33] P. Wheeler, H. Zhang, and D. Grant. A theoretical and practical consideration of optimized input filter design for a low loss matrix converter. In *IEE PEVD*, pages 363–367, September 1994.



## Biographies



**Raheel Muzzammel** received his B.Sc. Electrical Engineering Degree from Department of Electrical Engineering at University of Engineering and Technology, Lahore, Pakistan and M.S Electrical Engineering Degree from Department of Electrical Engineering at University of Lahore, Lahore, Pakistan. Currently he is working as a lecturer in the Department of Electrical Engineering in the University of Lahore, Lahore, Pakistan. His research interests include power systems, power system protection and power electronics



**Umair Tahir** is student of Department of Electrical Engineering in the University of Lahore, Lahore, Pakistan. He has done his final year research work project in three phase AC to AC matrix converters under the supervision of Raheel Muzzammel. His main research interests are power electronics, power systems and power system protection. He wants to pursue his further studies in power engineering.







## Improving the Characteristics of Switched Reluctance Motor

Phi Hoang Nha<sup>(1),(2)</sup>, Dao Quang Thuy<sup>(3)</sup>

Ha Noi university of science and technology

Ha Noi university of industry

Ministry of Science Technology

Ha Noi capital, Viet Nam

hvg.98@gmail.com, nhaphihoang@gmail.com

### Abstract

Switched reluctance motor (SRM) has outstanding advantages such as simple structure, absence of commutator, high torque. However, torque ripple and loud noise are the biggest disadvantages of this SRM. Thus, applications in some special areas in industry are restricted. To reduce torque ripple and improve output power, this article provides solutions for control and change the structure of SRM. At the same time, it also proposes a new solution: using of new materials – amorphous materials in manufacturing rotor and stator instead of normal Silicon steel materials. With special physical properties, the amorphous materials used in motor manufacture give a greater speed and lower loss.

**Keywords:** switched reluctance motor, torque ripple, amorphous materials.

### Nomenclature

AMN	Associative Memory Networks
APC	Angular Position Control
CCC	Current Chopping Control
CVC	Voltage Chopping Control
FEM	Finite Element Method
PI	Proportional Integral
PID	Proportional Integral Derivative
PWM	Pulse Width Modulation
RBF	Resting Bitch Face
SMC	Sliding Mode Control
SRM	Switched Reluctance Motor
TSF	Torque Share Function

### 1. Introduction

Switched reluctance motor (SRM), a type of simple structure motor, was proposed since 1842. However, SRM operates under the principle of switching electric current for each phase, so it was very difficult to control SRM at that time. By the 80s, with the rapid development of power electronics, microprocessors and control technology, SRM started becoming the choice for high speed control systems.

Switched reluctance motor has the advantages such as: simple structure, high reliability, the motor can work at an extremely fast speed. Thanks to permanent magnet and winding are absent in the rotor, the rotor temperature can be higher than other types of motor. Torque direction doesn't depend on current direction, so can simplify the inverter, reduce the cost of the system. As there isn't overcurrent that can damage the capacity valve in SRM, the inverter has a high reliability. Big starting torque, high speed controlling performance, there is no impact of the current in the induction motor at the time of starting. Magnetic circuit of motor can work in the linear region and the saturation of the B-H magnetic characteristic curve, using the maximum capabilities ferromagnetic materials, power ratio with weight is large. With the above advantages, SRM is widely used in industry and some specific sectors such as manufactured generators for aircraft launch, the centrifuges require high speed, dynamic the submarine base with large startup torque, etc.

However, due to salient pole structure of rotor such motor flux has strong non-linearity, torque ripple is large and highly noise. Therefore, in some cases, the applications of SRM are limited. In order to overcome these restrictions of torque ripple and improve the quality of motor, based on analysis, comparison and summarization of domestic and international relating documents, the authors of this article have figured out some solutions to reduce torque ripple including solutions of controlling and solutions of changing motor structure. At the same time, the authors also proposed a new solution - using new materials in the motor manufacturing to improve the characteristics of this switched reluctance motor.

### 2. Mathematical model of switched reluctance motor

#### 2.1. Voltage equation

Survey of SRM operating status requires a mathematical model. Since SRM is a non-linear system, it demands a suitable model which represents



the dynamic process in various operating conditions. Assuming the phase of the motor including: resistance of winding  $R$ , inductance  $L(i, \theta)$ , the voltage  $u$  supply to the phases by total voltage drop and the rate of flux  $\psi(i, \theta)$ , effects of mutual inductances can be neglected, Faraday's law gives:

$$\frac{d\psi(i, \theta)}{dt} = -iR + u$$

$$\leftrightarrow u = Ri + \frac{d\psi(i, \theta)}{dt} \quad (1)$$

$$\text{where } \psi(i, \theta) = (i, \theta)i \quad (2)$$

Switched reluctance motor structure is symmetrical so flux circulation cycle  $2\pi/n_R$  ( $n_R$  is the number of rotor poles). Hence, there are two concepts to be distinguished: mechanical angle  $\theta$  and electrical angle ( $n_R\theta$ ). Mechanical angle indicates the rotation angle of the rotor position, electrical angle shows angle calculating phase current and voltage. Voltage equation can be rewritten in the form of electrical angle as follows:

$$u = Ri + \frac{d\psi(n_R\theta, i)}{dt} \quad (3)$$

Consider the three phase motor, each phase mismatches of a electrical angle:  $\theta_s = \frac{2\pi}{3n_R}$ . Continue to ignore mutual inductance, equations for the phase voltages are as follows:

$$\begin{cases} u_a = Ri_a + \frac{d}{dt}\psi(n_R\theta, i_a) \\ u_b = Ri_b + \frac{d}{dt}\psi(n_R(\theta - \theta_s), i_b) \\ u_c = Ri_c + \frac{d}{dt}\psi(n_R(\theta - 2\theta_s), i_c) \end{cases} \quad (4)$$

## 2.2. Torque equation

In any rotor position of a phase, according to the principle of total of magnetic energy, the torque formula of the SRM is calculated as follows:

$$T(i, \theta) = \frac{\partial W'(i, \theta)}{\partial \theta} \quad (5)$$

$\theta$  is rotor azimuth

$i$  is phase current

$W'(i, \theta)$  is the total of magnetic energy

Total of magnetic energy is defined as the area under the curve of magnetization shown in Figure 1, it can be expressed as follows:

$$W'(\theta, i) = \int_0^i \psi(\theta, i) di \quad (6)$$

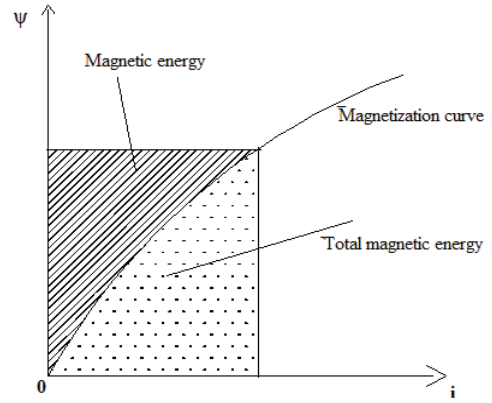


Figure 1. The chart outlines the total magnetic

In certain cases, SRM is not affected by magnetic saturation and inductance is independent of electric current, depends only on rotor position (2), the torque generated as follows:

$$T(\theta, i) = \frac{1}{2} \frac{\partial}{\partial \theta} \int_0^i (\theta, i) di^2 \quad (7)$$

If  $L$  changes linearly with rotor position, torque equation is as follows:

$$T = \frac{1}{2} i^2 \frac{d(\theta, i)}{dt} \quad (8)$$

Torque of three phase motor equal to total of phases torque:  $T_e = T_a + T_b + T_c$ .

## 2.3. Mechanical equation

According to the torque balance theorem of motor:

$$T_e - T_l = J \frac{d\omega_m}{dt} + \omega_m \quad (9)$$

$T_e$  is total torque

$T_l$  is load torque

$\Omega_m$  is speed

$J$  is inertia torque

$B$  is constant friction

Based on three equations above, we can build model of switched reluctance motor. This model based on the change of voltage equations:

$$\begin{cases} \frac{di_a}{dt} = \frac{-Ri_a - \frac{\partial}{\partial \theta} \psi(n_R\theta, i_a)n_R\omega + u_a}{\frac{\partial}{\partial i_a} \psi(n_R\theta, i_a)} \\ \frac{di_b}{dt} = \frac{-Ri_b - \frac{\partial}{\partial \theta} \psi(n_R(\theta - \theta_s), i_b)n_R\omega + u_b}{\frac{\partial}{\partial i_b} \psi(n_R(\theta - \theta_s), i_b)} \\ \frac{di_c}{dt} = \frac{-Ri_c - \frac{\partial}{\partial \theta} \psi(n_R(\theta - 2\theta_s), i_c)n_R\omega + u_c}{\frac{\partial}{\partial i_c} \psi(n_R(\theta - 2\theta_s), i_c)} \end{cases} \quad (10)$$





### 3. Solutions to improve the characteristics of switched reluctance motor

Switched reluctance motor torque ripple is really complicated and affected by many factors. Therefore, to reduce torque ripple, strategic solutions to be given are using SRM control method with definite motor structure and parameters [1] or changing motor structure. In this paper, the authors have presented, analyzed and compared with domestic and international researches relating to reduction of torque ripple and improvement of SRM characteristics.

#### 3.1. Solution using control method of switched reluctance motor

According to equation (1) and (8), motor control method can be performed by current control  $i$ , or adjust angle  $\theta$ . These are two important parameters to calculate the voltage and torque of SRM.

##### 3.1.1. Traditional control strategy

There are three ways in typical traditional control including angular position control (APC), current chopping control (CCC) and voltage chopping control (CVC).

The angular position of the control means at a certain voltage across the winding provided by changing  $\theta_{on}$  and  $\theta_{off}$  of main switch to change power-on and power-off. Thus, to control closed loop speed, it needs to adjust the phase current waveform signal. Opening angle  $\theta_{on}$  and off angle  $\theta_{off}$  can be revised, however in fact, we often have to fix  $\theta_{off}$  and change  $\theta_{on}$  according to control mode.  $\theta_{on}$  and  $\theta_{off}$  must be adjusted separately, then SRM is able to achieve optimum operating angle position control (APC) mode. There are some advantages of this control method such as greater torque adjustment range, multi phase windings simultaneously powered, high motor efficiency, suitable for higher speeds but unsuitable for low speed operation.

Current chopping control is mainly used for motor running at low speed. Because of increasing rapidly of the current, in order to avoid damage caused by current pulse, it requires to limit the peak current. This control method rarely involves  $\theta_{on}$  and  $\theta_{off}$  control, so select the position of each phase winding's conduction to control the current by chopper. The main advantages of this control method are simplicity and accuracy, reduction of torque ripple, suitable for the low speed operation of fixed load motor.

Voltage chopping control means keeping  $\theta_{on}$  unchanged and changing  $\theta_{off}$ , the power switching devices operate in pulse width modulation (PWM) mode. Keep the pulse period  $T$  fixed, simply adjust the duty cycle of the PWM waveform, thereby adjust the size of the voltage across the winding, which cause changes in winding phase current to achieve the regulation of motor speed. Advantages of the method are followings suitable for both high speed and low speed operation, enable quick adaptation to change of the load.

##### 3.1.2. Torque distribution strategy

Torque distribution strategy shows that by defining the torque share function (TSF), electromagnetic torque corresponding to the current phase can be distributed

reasonably to ensure each phase torque being at a constant value. Accordingly, phase current values can be calculated and combined with appropriate control strategies to reduce torque ripple.

Reference [2] proposes an optimized solution based on conventional torque distribution strategy to maximize the torque/ampere ratio within the allowable error range of torque ripple in adjusting the opening angle  $\theta_{on}$  and off angle  $\theta_{off}$  of SRM. Under the premise of guaranteed output torque, to achieve the optimal purpose, it is important to ensure lower the winding phase current. After testing, the results show that the optimized ratio of torque and current will improve the system performance.

For the SRM torque ripple, Reference [3] adopts the torque distribution based on controller to obtain the desired torque of each phase, and then synthesize the constant torque through each phase, effectively eliminate torque ripple.

Reference [4] combines the current torque distribution and current to achieve efficient suppression of the torque ripple. Up to a point, the method has achieved certain results, but choosing to divide torque has omitted necessary physical factors.

In order to extremely minimize the torque faults, reference [5] dissects the optimization by using flux linkage as optimized variables. With discrete method, the torque reducing problem is transferred into a mathematical programming issue. Its feasibility has been proved by simulation. But this method ignores the correlation between electromagnetic and winding.

##### 3.1.3. Intelligent control

Intelligent Control is a type of control of which object is mathematical non-linear, its properties are strong self-learning ability and adaptive capacity. Applying the intelligent control theory in designing SRM controller is one of the effective ways to solve thorny issue of SRM meaning torque ripple reduction. Performance control of SRM is significantly improved

##### a. Fuzzy control

Typical application of fuzzy control is an adaptive fuzzy control strategy of minimum SRM torque ripple proposed by Sayeed [6].

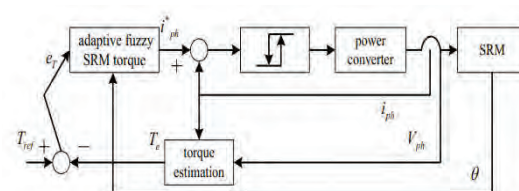


Figure 2. The block diagram of adaptive fuzzy torque control

Figure 2 shows the adaptive fuzzy SRM torque control system regarding position as an input, phase current as an output. Changing the membership function gave broken phases in the most appropriate area. The initial value of the fuzzy parameter is randomly selected. During the operation, the parameters are adjusted by the real time controller, able to adapt to the motor characteristics of any changes.



Reference [7] applies fuzzy neural algorithm constantly adjusting the size of the current compensation signal to optimize the phase current waveform and then to suppress torque ripple. Because of the difficulty in measuring the real time of the dynamic torque and expensive torque sensor, it is hard to apply this method. Reference [8] through the fuzzy neural network speed controller determines the desired torque output, calculates the current value of each phase.

Reference [9] proposes a new method of mathematical modeling of a motor switched reluctance, based on the static inductance curve and torque - angle characteristic curve, apply the adaptive network based on fuzzy inference system to the whole modeling of SRM.

#### b. Neural network

Reducing torque ripple based on neural network was first proposed by JGO Donovan [10]. SRM non-linear characteristics, SRM torque - current - angle relationship are analyzed based on the knowledges, experiences of professional experts.

Reference [11] applies AMN (associative memory networks) neural network online to get the motor phase current waveform optimization. Disadvantages of this approach are expensive torque sensor, inaccurate measurements at high speeds and no torque feedback during normal operation.

Reference [12] proposes combination of traditional PID with neural network to make adaptive PID control applied for serious non-linear SRM. The non-linear transformation properties and parallel processing ability at a high degree of neural network made it suitable for the establishment of non-linear predictive model parameters to predict. Through predicting the parameters of the control system, the dynamic response performance of the system can be improved as shown in Figure 3. The results show that the system is stable, quick, accurate, strong anti-disturbance and easy control.

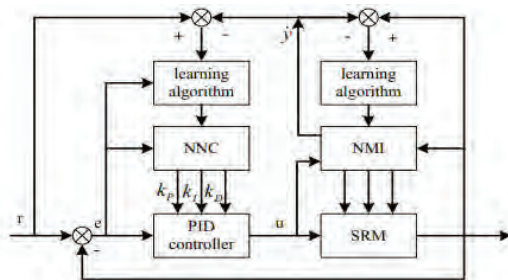


Figure 3. Block diagram of the non-linear model based on RBF neural network

Reference [13] proposes a SRM instantaneous torque control method which is based on radial basis function neural network. Using data generated from the SRM dynamic simulation for RBF neural network's offline training, learning to optimize current waveforms under different speed and torque, and then RBF network is used for controlling motor torque. Experimental results show that the control strategy can effectively reduce SRM torque ripple with high control accuracy, able to adapt to speed changes.

#### 3.1.4. Sliding mode control

Reference [14] proposes a new method to minimize torque ripple of a switched reluctance motor, which is based on the control of the sum of the square of the phase currents by using only two current sensor and analog multipliers. In addition, the sliding mode control (SMC) technique has been applied to SRM speed control loop that compensates the low frequency oscillations on the torque output. The results show that the continuous sliding mode controller is effective compared to PI or Fuzzy controllers in reducing the torque ripple of the motor, compensating for non-linear torque characteristics and making drive insensitive to parameter variations as well, low frequency vibration in torque variation has been eliminated.

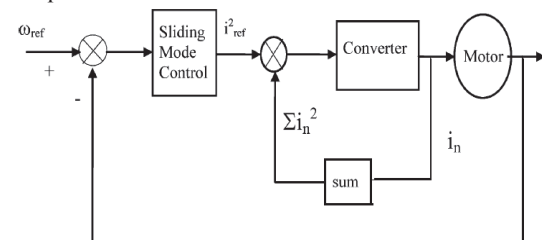


Figure 4. Block diagram for the speed control with SMC

In addition to the methods described above, the issue of SRM control to improve the work quality, reduce torque ripple which researchers overcome by the other control methods such as linearization control, Iterative Learning Control, Internal Model Control, etc.

### 3.2. Solution for change of switched reluctance motor structure

Equation (5) and (9) show the torque of motor directly affected by the magnetic flux density  $\psi(i, \theta)$  which is closely related to the motor structure. Therefore, motor structural change solution is presented to improve torque characteristics and SRM performance.

#### 3.2.1. Change the shape and size of stator and rotor pole

General purposes of designing switched reluctance motor is to maximize torque, reduce torque ripple by optimizing control manner and strategy. In terms of trade, however, the design target is not only to meet the requirements of torque at both low and high speed but also to reduce the cost of motor production. Reference [15] uses the finite element analysis method (FEM) to simulate the shape of SRM with many different configurations by changing the shape of stator and rotor poles.

Rotor is usually made of ferromagnetic materials (silicon). Ferromagnetic materials have a direct influence on making flux. The author changed iron ratio in the rotor (62%, 76%, 91%). In there, this rate of SRM rotor is 62% for max flux (0.031Wb). Thus, because of strong nonlinearities, inductance dependent of angle  $\theta$  and current  $i$ , changing ferromagnetic materials rate in SRM rotor contributes only to optimize calculations in design while has not shown a



clear positive correlation between ferromagnetic materials rate and flux in the motor.

The resizing rotor and stator poles size related directly to the change in order to achieve the ratio  $\gamma$  ( $\gamma$  is the ratio between rotor pole angle and pole pitch) and  $\beta$  ( $\beta$  is the ratio between stator pole angle and pole pitch). The stator and rotor pole angles are important variables in SRM design, it affects to the motor torque and it also has been studied to find precisely range of the stator and rotor pole angle in practice. A parameter obtained from generation of results in changing the poles is the ratio between the polar angle and pole pitch (pole pitch is the angle between two consecutive stator poles or rotors). Survey results in 3 phase SRM, reference [15], give the optimal value  $\gamma$  and  $\beta$  ( $\gamma = 0.38$ ,  $\beta = 0.5$ ) for the highest performance.

The advantage of this method is figured out the optimal parameter  $\gamma$ ,  $\beta$  and torque increased. However, the torque also depends on many other motor configuration parameters; motor is only surveyed to stop at 3 phase SRM 6/4 poles and 8/6 poles, low speed range.

### 3.2.2. Change rotor and stator pole surface

The non-linear torque in the overlap region is the main cause of torque ripple. Also, the radial force is generated in the whole overlap area of stator and rotor poles and the tangential force is generated at the edges of stator and rotor poles, respectively. To reduce the fringing flux at the overlap angles, a rotor shape made by method of laminated layer of the asymmetry rotor is proposed [16], as Figure 4a. To have the asymmetry angles, the width of each steel sheet at rotor pole arc needs to be different. Research results conducted with SRM 12/8 poles show that the torque ripple was reduced by 15% against the initial SRM and increased by 12.5% compared with normal structures. However, switched reluctance motor was tested with quite small capacity, just 1.5kW.

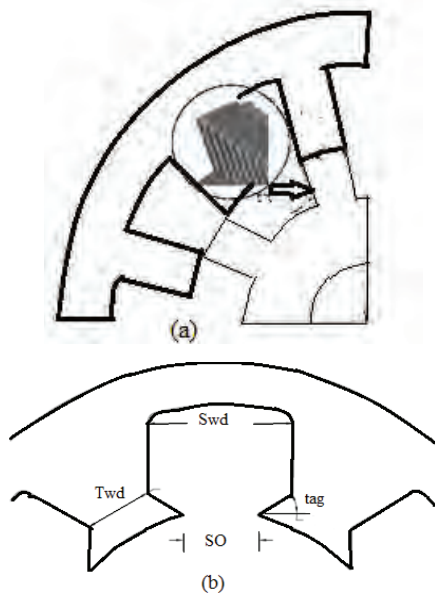


Figure 4. Surface structure of rotor pole (a) and stator pole (b)

Stator pole shape has been changed in the reference [17]. Stator pole surface is constructed in tip shape as shown in Figure 4b, flared wide at the tip to increase the amount of magnetic flux passing, the magnetic flux density exists in the stator poles increased, resulting in increased torque. The author used multi domain simulation environment (ANSYS workbench) to simulate the magnetic field, torque of switched reluctance motor.

### 3.2.3. Change the number of rotor pole

The number of stator pole in initial SRM is more than number of rotor pole (6/4, 8/6, 12/8, etc). However, 6/10 SRM introduced in reference [18] is a new motor concept, in which the rotor poles are more than the stator poles, focusing on creation of greater torque, improving torque density, reducing torque ripple while maintaining continuous thermal energy density. These advantages are thanks to structure of 6/10 SRM with pole pitch and rotor angle smaller than traditional structure. The more aligned positions between rotor and stator are created the more flux with maximum value increased.

The author has made a comparison of 6/10 SRM and 6/4 SRM about the flux in stator winding, thermal efficiency, torque density and torque ripple. With 6/10 SRM, torque performance increases (up to 119.82% compared with the 6/4 SRM). However, the winding temperature is more than 40% and torque ripple is not reduced.

Reference [19] shows the new structure of SRM with equal number of rotor poles and stator poles (6/6 pole). However, with such a structure of pole, the motor can not be started by itself. But this is also a special point because this motor uses only single phase. Thus, the system has a simple converter having two important roles: to improve the input power factor and to stimulate the motor phase. A test was conducted for 6/6 pole motor with rated power of 400 W and speed of 1800 rpm. However, this study is just applied for the survey of current and voltage during engine operation with the expectation of high performance at low cost of system.

### 3.2.4. Change the number of stator teeth

In principle, it is expected that increasing the number of teeth per stator pole may be increase more advantages, limit disadvantages and enlarge widely certain applications of switched reluctance motor. It seems generated torque has increased owing to increasing number of teeth, the losses in the motor are limited, particularly at high speeds. These losses are lower than that in SRM with only one tooth per stator pole. The first SRM with many teeth per stator pole which is 6 pole 3 phase 12/10 slotted motor with 2 teeth per pole stator. Other version of 4 teeth per stator pole is 3 phase motor with 22 tooth rotor and 24 stator teeth [20], as shown in Figure 5. Both these motors are designed with same frame size and air gap for easy comparison. The simulation result in two bands speed is 300 rpm and 750 rpm showing greater motor performance and high torque. However, at a speed of 300 rpm, 24/22 SRM has higher performance than 12/10 SRM; at speed of 750 rpm, the result is opposite.





Besides the methods described above, some researches continue to be made to improve the characteristics of SRM as adjusted inclined slotted, perforated on the rotor teeth, tilted stator pole, rotor, etc. Those methods have contributed to improve the work quality of the switched reluctance motor in certain cases, but the contribution in reducing torque ripple is not thoroughly made.

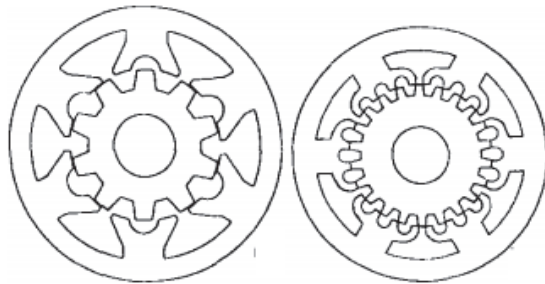


Figure 5. Stator pole structure many teeth

### 3.3. Propose a solution using new materials

Equation (2) shows the relationship between magnetic flux  $\psi$  with current  $i$  and angle  $\theta$ . This flux curve is non-linear, depends on the materials of rotor, stator. In equation (5), (6), the effect of magnetization of materials to torque, torque ripple is quite clear. Therefore, changing the motor manufacturing materials is an effective solution in order to improve motor characteristics.

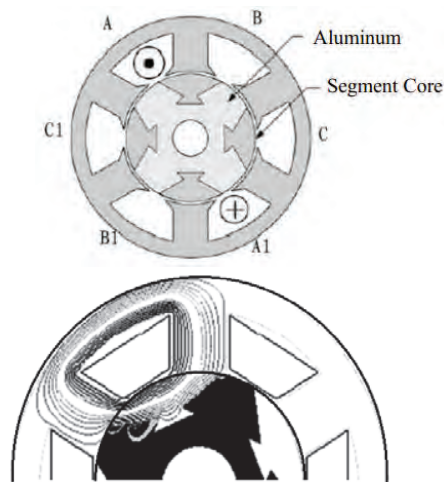


Figure 6. Rotor structure used aluminum materials and magnetic field lines

Currently, both switched reluctance motor in particular and other motor types in general use electrical steel in manufacturing rotor and stator. Electrical steel is a soft ferromagnetic, large magnetic permeability, small degaussing magnetic, low hysteresis loss (due to narrow magnetic hysteresis curve). However, ferromagnetic materials exist limitations such as low operating frequencies (silicon steel cores can be used only for low frequency, at high frequency, losses will be greater due to low resistivity of silicon steel), small coercivity force, etc. Moreover, due to the requirements

of environmental protection and saving energy, reducing core losses and magnetic losses, the solutions using other materials instead of ferromagnetic materials started to be proposed.

Reference [21] gives a new type of SRM model used unibody aluminum for rotor core, the purpose is to reduce motor weight, as shown in Figure 6. At the same time, to create magnetism in the rotor, the magnetic core is embedded in the rotor blocks. This design has been used to make the low speed motor. The simulation results show that torque did not significantly increase. due to the fact that the magnetic field lines didn't go through the central rotor (rotor core made of aluminum) causing the low density of magnetic flux. However, thanks to removing the radial magnetic force, noise is significantly reduced.

Based on the results of research using new materials being low-iron-loss such as Super E-Core brand, reference [22] also made comment that strip steel has improved performance of the SRM and prevent steel loss.

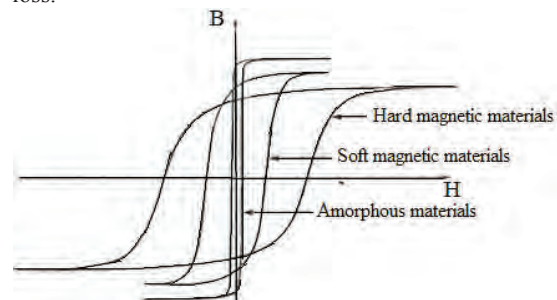


Figure 7. Magnetic hysteresis curves of magnetic materials

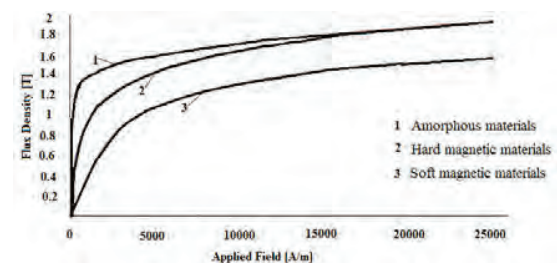


Figure 8. Saturation of flux density with the different materials

Through the synthesis of researches on some new materials with good magnetic and high conductivity, authors have proposed solutions using new materials in order to replace conventional ferromagnetic material. This new material is amorphous alloys. Amorphous alloy is a kind of alloy made of iron or cobalt (Co), in the amorphous state, so its resistivity is much higher than crystalline alloy. At the same time, this material is resistant to corrosion, high mechanical strength, can be used at higher operating frequencies than crystal material of metal base. Without crystal structure of amorphous material permits elimination of, anisotropic so its properties are highly soft magnetic. Cobalt amorphous materials have magnetostrictive by 0 so it has



a very small coercive force, can be compared with nanocrystalline materials. Magnetic hysteresis curve of this material is much narrower than silicon steel – soft magnetic materials (Figure 7). Natural thickness of the amorphous steel sheets is very small around  $\sim 0.03$  mm compared with  $\sim 0.3 - 0.5$  mm of silicon steel, resistivity greater  $\sim 130 - 170 \mu\Omega\text{cm}$  compared with  $\sim 50 - 60 \mu\Omega\text{cm}$  of silicon steel. Therefore, steel core loss reduced significantly compared with silicon steel. To demonstrate the effectiveness of the research results, the research team has developed the characteristic curves for evaluation that is described in figure 8. Thus, it is shown that amorphous steel is capable of spontaneous magnetization and long-lasting magnetizing energy which increased the magnetic flux density and improved motor torque (Figure 8). Moreover, amorphous material weight is very light useful for motor operation at much higher speed than normal motor. Analytical result shows that steel core losses in amorphous materials decreased by about 20% compared with silicon steel, magnetic flux density increased by over 12% and the motor speed can be up to 140% compared to the motor manufactured by conventional silicon steel. The analytical result is shown in Table 1.

Table 1. Result of the study compared with the traditional SRM [23] at speed  $n = 3000$  rpm and current  $I = 4$  A.

Motor specs	New SRM	Traditional SRM
Copper losses (W)	2.24	2.8
Core losses (W)	1.2	1.4
Motor efficiency (%)	83.7	75.4
Aligned inductance (mH)	4.2	3.75
Unaligned inductance (mH)	0.78	0.7
Average torque (Nm)	0.053	0.047

Therefore, the research and design of switched reluctance motor using amorphous materials is an important and necessary solution. However, it is necessary to evaluate the relationship of the magnetic field in the motor to give a specific design technology and manufacture using amorphous materials. Research result announced by the authors in this paper is initial, the standardized assessment results through the simulation of physical transformation process of the motor parameters will be announced in the appropriate time.

#### 4. Conclusion

This article presents different solutions in order to improve the characteristics of switched reluctance motor. With the development of various intelligent control theories, SRM controller has achieved good results in reducing torque ripple. At the same time, research of solution changing the internal structure of motor which will be continued because of its effective

solution to strictly overcome the disadvantages of the switched reluctance motor.

#### 5. References

- [1] X. Gao, X. Wang, Z. Li and Y. Zhou. A review of torque ripple control strategies of switched reluctance motor, *International journal of control and automatic*, vol. 8, no. 4, pp. 103 - 116, 2005.
- [2] B. L. Zhang, Y. W. Qi and G. S. Xu. Switched reluctance motor torque distribution Strategy optimization, *Journal of HeFei University of Technology*, no. 12, vol. 35, pp. 1615 - 1619, 2012.
- [3] Z. L. Shi, Y. S. Huang and X. Chen. Research on control system of Switched Reluctance Motor Based on torque distribution strategy, *Coal mine machinery*, vol. 31, no. 12, pp. 59 - 61, 2010.
- [4] B. Yang, J. Y. Cao and Y. P. Chen. A new method to reduce the torque ripple of switched reluctance motor, *Small and medium sized motor*, vol. 28, no. 4, pp. 11 - 15, 2001.
- [5] J. Y. Cao, Z. D. Zhou and Y. P. Chen. A new method of switch reluctance motor torque control, *Proceedings of the CSEE*, 2005.
- [6] S. Mir, M. E. Elbuluk and I. Husain. Torque ripple Minimization in Switched Reluctance Motors Using Adaptive Fuzzy Control, *IEEE Transactions on Industry Applications*, vol. 35, no. 2, pp. 461 - 468, 1999.
- [7] L. O. A. P. Henriques, L. G. B. Rolim and W. I. Suemitsu. Torque Ripple Minimization in a Switched Reluctance Drive by Neuro-fuzzy Compensation, *IEEE Transactions on magnetics*, vol. 36, no. 5, pp. 3592-3594, 2000.
- [8] Z. Q. Fan and P. Wang. Methods of inhibiting intelligent torque ripple of switched reluctance motor, *Micromotor*, vol. 28, no. 2, pp. 28 - 30, 2000.
- [9] D. L. Liang, W. Ding and Z. M. Yu. Modeling for Switched Reluctance Motor Based on adaptive network based fuzzy inference system, *Proceedings of the CSEE*, 2008.
- [10] J. G. O'Donovan, P. J. Roche and R. C. Kavanagh. Neural Network Based Torque Ripple Minimization in a Switched Reluctance Motor, *IECON*, pp. 1226 - 1231, 1994.
- [11] D. S. Reay, T. C. Green and B. W. Williams. Application of Associative Memory Neural Networks to the Control of a Switched Reluctance Motor, *IECON*, vol. 1, pp. 200 - 206, 1993.
- [12] C. L. Xia and J. Xiu. Switched reluctance motor adaptive PID prediction model of non-linear control based on RBF neural network, *Proceedings of the CSEE*, 2007.
- [13] C. L. Xia, Z. R. Chen and B. Li. Switched reluctance motor instantaneous torque control based on RBF neural network, *Proceedings of the CSEE*, 2006.
- [14] Nihat Inanc, Veysel Ozbulur. Torque ripple minimization of switched reluctance motor by using continuous sliding mode control technique, *Electric Power Systems Research*, vol. 66, pp. 241 - 251, 2003.



- [15] Wadah Abass Aljaism. Switched reluctance motor: Design, simulation and control, PhD thesis, University of Western Sydney, 2007.
- [16] Lingquan Zeng, Haiwei Yu. Research on a novel Rotor Structure Switched Reluctance Motor, International Conference on Applied Physics and Industrial Engineering, Physics Procedia, vol. 24, pp. 320 – 327, 2012.
- [17] Jawad Faiz , J.W. Finch , H.M.B. Metwally. A novel switched reluctance motor with multiple teeth per stator pole and comparison of such motors, Electric Power Systems Research, vol. 34, pp. 197 – 203, 1995.
- [18] Piyush C. Desai, Mahesh Krishnamurthy, Niegel Schofield, Ali Emadi. Design and performance evaluation of a novel 6/10 switched reluctance machine, IEEE Xplore, 2009.
- [19] Sang Hun Lee, Feel Soon Kang, Sung Jun Park, Su Eog Cho, Man Hyung Lee. Single stage power factor corrected converter for switched reluctance motor drive, Electric Power Systems Research, vol. 76, pp. 534 – 540, 2006.
- [20] M. Sundaram, P. Navaneethan, M. Vasantha Kumar. Magnetic analysis and comparison of switched reluctance motor with diferent stator pole shapes using a 3D finite element method, ICGST-ACSE Journal, ISSN 1687 - 4811, Volume 9, Issue II, December 2009.
- [21] Ju Hwan Oh, Byung Il Kwon. New rotor shape design of SRM to reduce the torque ripple and improve the output power, IEEE Xplore, 2010.
- [22] Takanori Suzuki, Shinya Ito, Naoki Tanaka, Akira Chiba, Tadashi Fukao, Hironori Ninomiya. Development of high efficiency switched reluctance motor, Electrical Engineering in Japan, Vol. 162, No. 2, 2008.
- [23] Torsten Wichert. Designed and construction modifications of switched reluctance motor, PhD thesis, Warsaw University of Technology, 2008.

## Biographies



M.Sc Phi Hoang Nha, 1988. He works at the electric facult, Ha Noi university of industry. He is also currently studying at Ha Noi university of science and technology. His areas of interest include the control, electrical equipment.



Ph.D Dao Quang Thuy, 1978. He works at the Ministry science and technology. His areas of interest include the measurement and control, electrical equipment, etc. He is also lecture at some universities.

